University of Nottingham
UK | CHINA | MALAYSIA

# Non-equilibrium Quantum Simulations using Thimble Methods

Thesis submitted to the University of Nottingham for the degree of **Doctor of Philosophy, December 2023.**


**Simon J. Woodward**

**4311477**

Supervised by

**Paul Saffin**
**Antonio Padilla**


Signature _____

Date _____ / _____ / _____

# Abstract

Our understanding of time dependent phenomena in particle physics is hampered by our inability to effectively investigate non-equilibrium phenomena, even using computers, due to the 'Sign Problem'. This problem means that for non-perturbative theories, it is functionally impossible to evaluate Feynman path integrals to calculate the expectation values of operators. Here I present a possible remedy to this problem in the form of Generalised Thimble Techniques which, at great computational cost, suppress the Sign Problem and allow us to make headway in these investigations.

The formalism for moving these path integrals onto a discrete lattice is discussed, and is followed by an explanation of the mechanics of these Thimble techniques. These techniques are then compared, both in terms of approach and in terms of performance, to the other prominent approach to dealing with the Sign Problem, Langevin Dynamics. The implementation of these techniques is then demonstrated by comparing my results with literature, and how to best compensate for the computational cost is considered.

The discussion then turns to how best to take advantage of the non- perturbative nature of these calculations. The lattice is modified, the characteristic imaginary time extension is removed and replaced with a bespoke density matrix, which is sampled independently of the thimble. This removal of the imaginary time extension opens the door to non-equilibrium density matrices, but initially the focus is on ensuring that these modifications are valid, and reproduction of equilibrium results takes priority.

Unfortunately, the requirement to sample the density matrix independently of the thimble poses new computational problems however. The focus therefore briefly returns to optimisations, this time focusing on physical parameters of the system rather than numerical tricks or approximations. With these optimisations higher dimensional simulations are considered, but are still found to be too intensive for the available hardware. Instead, a second field is introduced, allowing the system to start out of equilibrium in a different way. This second field has a higher mass and occupation number, and two different interactions with a range of coupling strengths are considered. This means 'particle' decay can be seen between the two fields.

The technique is shown to be promising, but hampered by its high computational cost. Possible routes to reducing this through both improvements to the algorithm and promising developments in hardware are discussed.

# Acknowledgements

It would be impossible to thank everyone who has helped me during my Ph.D. studies without going well beyond the word limit. However, above everyone else there are a few people who stand out. Firstly to my partner Rowann, who has not only put up with my incessant talk about physics and computing at the dinner table, but supported me wholeheartedly through the most difficult part of this project with only minimal jokes at my expense. My father, who in addition to the enormous assistance provided throughout my life somehow found the time to give me his thoughts on this work, and whose ability to spot split infinitives in the prose managed to continually amaze me. My supervisor, Paul and my collaborators Anders and Mou, without whom this project could have never taken shape. Everyone with whom I have shared the Centre for Astronomy and Particle Theory/Cosmology between 2017 and 2022, especially those in office A113, you've kept me sane and helped me in more ways than I can list here. Finally to my mother, who if I'd written just a little faster could have read this for herself.

# Contents

# List of Tables

# List of Figures

# Chapter 1

# Introduction

Along with the deep ocean, the early universe is not yet well understood. The reasons for this are remarkably similar, given the differences in subject matter. Neither can be inspected in person, nor can they be observed through the passage of light, as it is blocked by water or the plasma that preceded recombination. Both, however, are areas of immense scientific interest as, just as the oceans are critical to understanding the formation of life bearing conditions on Earth, the early universe is critical to understanding the formation of all structure from the single atoms that formed in the wake of recombination to the largest clusters of galaxies [4, 5, 6, 7, 8, 9, 10, 11].

Given how important the formation of matter is to understanding our universe and everything within it, why is our understanding still so lacking? As mentioned above, direct observations of recombination are impossible to obtain using photons, as the high energy plasma forms what is known as the primordial light barrier. This is because the conditions were unfavourable for the formation of neutral hydrogen, meaning the universe was highly charged. Consequently the mean free path of a photon was very short, and the history of this era, and its preceding eras must be inferred or observed through other means. [12, 13, 14, 15, 16, 17, 18]. However, similar observational problems plague research into dark matter, and yet remarkable progress has been made in eliminating dark matter candidates,

and understanding its dynamical behaviour in recent years [19, 20, 21, 22, 23]. This is in large part because gravity, the primary or perhaps only, way dark matter interacts with the rest of our universe is understood well enough and is (from a numerical perspective) simple enough to be well implemented to be implemented on a computer without issue. Consequently potential models and initial conditions can be tested against observation through computer simulations, such as those generated by the Three Hundred Project [21]. This has resulted in the development of a Cosmological Standard Model based around cold dark matter and a cosmological constant with tight constraints on the composition of the dark matter, such as the tight restriction placed on the amount of primordial black holes that could make up dark matter [24, 25, 26, 27, 28].

The sudden changes in the behaviour of matter as the universe cools presents a problem for computational scientists preventing similar techniques to those used to eliminate dark matter models from being used here. This is because, by definition this problem is both non-equilibrium and due to its high energy is non-perturbative, conditions which have typically been hard to resolve on a computer [29, 30, 31, 32]. In a large part, the computational difficulties encountered are tied to the so called 'sign problem' which represents the issues with numerically calculating the integrals of highly oscillatory functions [33, 34, 35, 36]. Unfortunately, such integrals occur all over science, but particularly in particle physics where the path integral approach is key to evaluating the expectation values of operators [1, 2, 37, 38]. There have been historically a number of attempts made to deal with the sign problem motivated by the frequency of its appearance [39, 35]. Unfortunately, none of these techniques have been completely successful, until recently. The development of 'generalised thimble' techniques, a numerical technique developed from Picard-Lefshetz thimbles, has opened the door to effective although computationally expensive solutions to this problem [40, 41, 42, 43, 44, 45, 46, 47, 1, 48].

This thesis uses generalised thimble methods on a lattice based on a modified Schwinger-Keldysh contour, which will be discussed later. Using this, it shows

that it is possible to simulate non-equilibrium, non-perturbative problems using lattice quantum field theory. The thimble techniques, their uses in general, and how they're used here to calculate expectation values is described in Section 1.2, and implemented in Chapters 2 - 4. The Schwinger-Keldysh contour is discussed below, and the modifications made to it to separate the initial conditions from the lattice itself are discussed and tested in Chapter 3, the chapter itself based on the work published in [49]. Chapter 4 meanwhile is based on work published in [41], and builds on the work in Chapter 3 by using these modifications to simulate 'particle' transfer between two fields that start in non-equilibrium conditions, for a range of coupling strengths that go beyond the perturbative regime.

## 1.1 Path Integral Formalism

### 1.1.1 The Schwinger Keldysh Contour

Perhaps the single most important task for any quantum formalism is to be able to predict the expectation values of operators, and the variation of that expectation value over time [29, 50, 51, 52]. This can be achieved for a pure state by taking an initial state $|\psi_0\rangle$ and applying the time evolution operator which takes a state from time $t_0$ to time $t$ [53, 54] and has the form

$$\hat{U}(t_0, t) = e^{-i\int_{t_0}^{t} \mathrm{d}t' \hat{H}(t')}. \tag{1.1}$$

As a result, the expectation value can be found using

$$\langle \hat{O}(t) \rangle = \langle \psi_0 | \, \hat{U}(t, t_0) \hat{O}(t) \hat{U}(t_0, t) \, | \psi_0 \rangle \,, \tag{1.2}$$

this naturally leads to the idea of a basic contour. Despite the use of $\hat{O}(t)$ notation, this is still implemented in the Heisenberg picture, and kept only for the discussion of time separated observables later. As shown in Figure 1.1 (1.2) represents a path along the real time axis from $t_0$ to $t$ and back [29]. Note that these branches are on the real axis and are separated in the diagram for illustrative

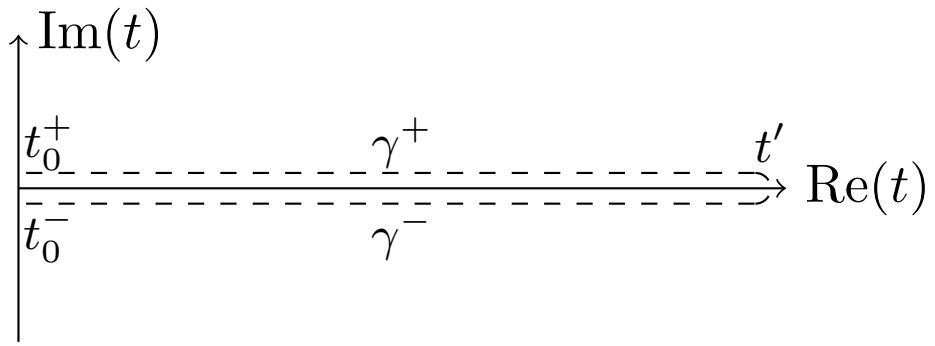


Figure 1.1: A simple contour, familiar from quantum mechanics.

purposes only.

This corresponds to the $\langle \text{in}|\text{in}\rangle$ formalism, where the two states used for the calculation are at the beginning of the time considered and is typically useful for capturing time dependent effects as will be the focus of later chapters. This can be contrasted with the $\langle \text{in}|\text{out}\rangle$ formalism, where the states considered represent the distant past and future of the system, and typically represents perturbative scattering, which while a useful technique, is not principally considered here.

Returning to Figure 1.1 $\gamma^{\pm}$ is defined to be the branches of the contour and $\gamma = \gamma^{-} \oplus \gamma^{+}$ to be the entire contour as in Figure 1.1. As a result, (1.2) can be rewritten as

$$\langle \hat{O}(t) \rangle = \langle \psi_0 | \exp\left( -i \int_{\gamma^+} \mathrm{d}t' \hat{H}(t') \right) \hat{O}(t) \exp\left( -i \int_{\gamma^-} \mathrm{d}t' \hat{H}(t') \right) |\psi_0\rangle \,, \tag{1.3}$$

and by using the time ordering operator $T$ it becomes,

$$\langle \hat{O}(t) \rangle = \langle \psi_0 | \, T \left[ \exp\left( -i \int_{\gamma} \mathrm{d}t' \hat{H}(t') \right) \hat{O}(t) \right] |\psi_0\rangle \,. \tag{1.4}$$

Note that $T$ time orders along the contour; this means that a point on the backwards ($\gamma^+$) branch occurs after any point on the forwards contour, even if the point on the forwards contour is closer to $t_0$ [29].

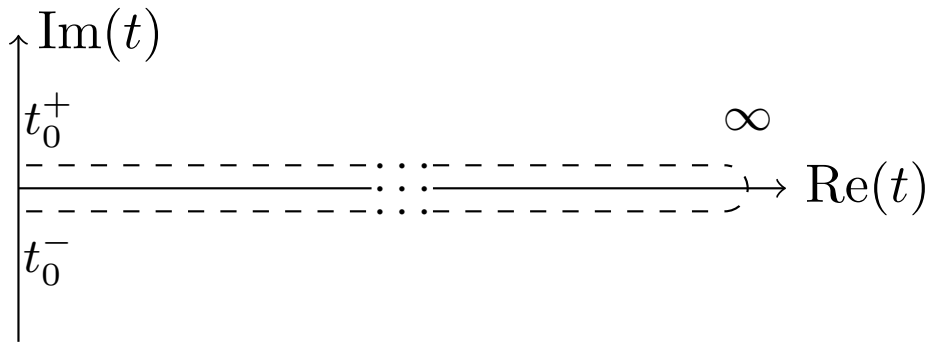


Figure 1.2: Extending the contour to infinity does not affect the values of an observable calculated along its path.

There is a simple but important implication of this. Consider the case where $O(t) = \hat{\mathbb{I}}$, and the contour extends to $t = \infty$. This means that

$$T\left[\exp\left(-i\int_\gamma \mathrm{d}t'\hat{H}(t')\right)\hat{\mathbb{I}}\right] = \hat{U}(\infty, t_0)\hat{U}(t_0, \infty) = \hat{\mathbb{I}}, \tag{1.5}$$

as the transforms will undo each other. It is worth noting here, that although the distant time $= \infty$ case is most useful for this work, this also applies for finite $t$. Both of these cases can be understood intuitively, and can be verified by inserting (1.1) into (1.2) with $t = \infty$. There exists a useful property of the contour here. Although the time extent has always been to the point of physical interest, $t$, nothing presented here has required that the path immediately turn and begin its return to the origin. Taking the contour shown in Figure 1.1 and extending it past $t$, all the way to $\infty$, as shown in Figure 1.2, it can be seen that (1.4) does not change. This can be seen by inserting an evolution to infinity and back within the time ordering operator,

$$\begin{aligned} T\left[\exp\left(-i\int_\gamma \mathrm{d}t'\hat{H}(t')\right)\hat{\mathcal{O}}(t_+)\right] &= \hat{U}(t_0, t_+)\hat{\mathcal{O}}(t)\hat{U}(t_+, \infty)\hat{U}(\infty, t_0) \\ &= \hat{U}(t_0, t_+)\hat{\mathcal{O}}(t)\hat{U}(t_+, \infty)\hat{U}(\infty, t_+)\hat{U}(t_+, t_0) \\ &= \hat{U}(t_0, t_+)\hat{\mathcal{O}}(t)\hat{U}(t_+, t_0), \end{aligned} \tag{1.6}$$

where the same logic used in (1.5) allows the contraction of the evolution operators that go to infinity. This touches on a property of physical operators on such a contour, that physical operators must obey the condition that $\hat{\mathcal{O}}(t) = \hat{\mathcal{O}}(t_-) = \hat{\mathcal{O}}(t_+)$, that physical operators must be valued at the same on both contours [29, 55, 56]. This process can be repeated along the other path, and both results show that the extension past the insertion of the operator cancels completely. This property is intuitive, a physical value cannot depend on a future state. However, it is a useful sanity check for the method, and a reassuring check that alterations to the contour made in Chapter 3 are valid.

This requirement that $\hat{\mathcal{O}}(t) = \hat{\mathcal{O}}(t_-) = \hat{\mathcal{O}}(t_+)$ enforces that two point correlators do not change depending on which branch or branches the arguments are on. Specifically $\left\langle \hat{\mathcal{O}}(t_{0-})\hat{\mathcal{O}}(t_{1+}) \right\rangle = \left\langle \hat{\mathcal{O}}(t_{0+})\hat{\mathcal{O}}(t_{1-}) \right\rangle$, along with their same branch correlators.

Moving from pure states to mixed states, the definition of the expectation value as defined in (1.2) can be updated to

$$\langle \hat{O}(t) \rangle = \sum_n \sigma_n \langle \phi_n | \hat{O}(t) | \phi_n \rangle , \tag{1.7}$$

where $\sigma_n$ represents the probability of finding the system in state $\phi_n$ [29]. This naturally leads to the definition of the density matrix,

$$\hat{\rho} = \sum_n \sigma_n | \phi_n \rangle \langle \phi_n | , \tag{1.8}$$

which can be used to define

$$\begin{aligned} \langle \hat{O}(t) \rangle &= \sum_i \sum_n \sigma_n \langle \phi_n | \Psi_i \rangle \langle \Psi_i | \hat{O}'(t) | \phi_n \rangle \\ &= \sum_i \langle \Psi_i | \hat{O}'(t) \hat{\rho} | \Psi_i \rangle \\ &= \mathrm{Tr}\Big\{ \hat{O}'(t)\hat{\rho} \Big\} = \mathrm{Tr}\Big\{ \hat{\rho}\hat{O}'(t) \Big\}, \end{aligned} \tag{1.9}$$

where a complete basis of states $|\Psi_i\rangle$ were inserted, $\hat{O}'(t)$ represents the operator in the RHS of (1.4), and in the final line the cyclic property of the trace was used to write this expression in its more common form [57, 58, 59]. The typical form for the density matrix operator in thermodynamic equilibrium is given by

$$\hat{\rho} = \frac{e^{-\beta\hat{H}}}{\mathrm{Tr}\Big\{e^{-\beta\hat{H}}\Big\}}, \tag{1.10}$$

where $\beta$ is the inverse temperature and the definition of $\beta$ is given to be $\beta = 1/k_B T$ [60, 61]. Combining this definition with (1.9), the full time dependent expectation value for a system in thermal equilibrium can be found

$$\langle\hat{O}(t)\rangle = \frac{\mathrm{Tr}\Big\{e^{-\beta\hat{H}}T\left[\exp\Big(-i\int_\gamma \mathrm{d}t'\hat{H}(t')\Big)\hat{O}(t)\right]\Big\}}{\mathrm{Tr}\Big\{e^{-\beta\hat{H}}\Big\}}. \tag{1.11}$$

The exponential factor can be written as

$$\exp\Big(-\beta\hat{H}\Big) = \exp\left(-i\int_{\gamma^v}\mathrm{d}t'\hat{H}(t')\right), \tag{1.12}$$

where $\gamma^v$ is any path in the complex plane between $t_1$ and $t_2$ such that $t_2 - t_1 = -i\beta$. This combined with inserting the LHS of (1.5) into the denominator of (1.11) it can be seen that

$$\langle\hat{O}(t)\rangle = \frac{\mathrm{Tr}\Big\{\exp\Big(-i\int_{\gamma^v}\mathrm{d}t'\hat{H}(t')\Big)T\left[\exp\Big(-i\int_\gamma \mathrm{d}t'\hat{H}(t')\Big)\hat{O}(t)\right]\Big\}}{\mathrm{Tr}\Big\{\exp\Big(-i\int_{\gamma^v}\mathrm{d}t'\hat{H}(t')\Big)T\left[\exp\Big(-i\int_\gamma \mathrm{d}t'\hat{H}(t')\Big)\right]\Big\}}. \tag{1.13}$$

This means that both the time evolution and the density matrix are implemented in the same way; the exponentiation of an imaginary line integral of the Hamiltonian operator [62, 29]. The difference is that the time evolution is integrated along a real time contour, and the density matrix is implemented along an imaginary time contour. However, mathematically these contours can be combined by allowing time to take on a complex value, working the density matrix into the structure of the contour itself. Typically this contour is defined

$$\gamma = \gamma^- \oplus \gamma^+ \oplus \gamma^v, \tag{1.14}$$

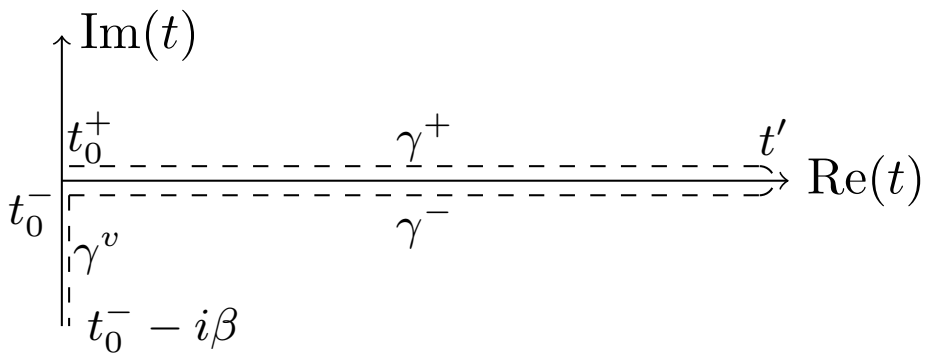


Figure 1.3: The traditional Schwinger-Keldysh contour, extending along the real axis to a specific point $t$ and back, before incorporating the equilibrium density matrix through the imaginary extension.

which is shown graphically in Figure 1.3, and is commonly known as the Schwinger-Keldysh contour [63, 64, 65]. This contour forms the basis for the numerical simulations undertaken in Chapter 2, and is the origin of the modified contour on which the simulations in Chapters 3 and 4 are based. (1.14) allows (1.13) to be rewritten in its final form

$$\langle \hat{O}(t) \rangle = \frac{\mathrm{Tr}\Big\{T\Big[\exp\Big(-i\int_\gamma \mathrm{d}t' \hat{H}(t')\Big)\hat{O}(t)\Big]\Big\}}{\mathrm{Tr}\Big\{T\Big[\exp\Big(-i\int_\gamma \mathrm{d}t' \hat{H}(t')\Big)\Big]\Big\}}. \tag{1.15}$$

For a system in thermal equilibrium, by definition there is no time dependence for the expectation value of an operator. Correspondingly, this results in two point functions that depends on the difference between the two time values, with no consideration of the specific time values [29]. The Wightman propagators are defined

$$i\Delta^>(t_2 - t_1) = \langle 0|\, \hat{q}(t_2)\hat{q}(t_1)\, |0\rangle \tag{1.16}$$

$$i\Delta^<(t_1 - t_2) = \langle 0|\, \hat{q}(t_2)\hat{q}(t_1)\, |0\rangle \quad , \tag{1.17}$$

with $t_2 > t_1$ and $\Delta^>$ represents forward time propagation $\Delta^<$ the opposite, and are examples of time separated two point functions as described above [66]. The advanced and retarded Green's functions can be defined in terms of the the Wight-

man propagators [66],

$$G^{>}(t_2 - t_1) = \theta(t_2 - t_1) i \left[\Delta^{>}(t_2 - t_1) - \Delta^{<}(t_2 - t_1)\right] \tag{1.18}$$

$$G^{<}(t_2 - t_1) = -\theta(t_1 - t_2) i \left[\Delta^{>}(t_1 - t_2) - \Delta^{<}(t_1 - t_2)\right] \quad . \tag{1.19}$$

These correlators will be of critical importance to the calculation of observables, such as the occupation number, in later chapters.

### 1.1.2 Discretisation to a Lattice

The discussion in this chapter has been analytic. However, the research work in this thesis has been done using numerical techniques and it is of use to briefly discuss what the impact of this will be. By discretising to a lattice the continuously valued fields are broken into specific points separated by a fixed finite separation, as shown in Figure 1.4; this allows the contour to be more efficiently parsed by a computer. The link sizes were taken to be constant throughout the lattice, including in the imaginary time direction. In principle, this is not required, a variable sized lattice can be useful for capturing interesting physics without wasting computational time. However, for the systems considered here, ease of implementation and error mitigation was prioritised. This has implications for the frequencies exhibited by systems modelled on such a lattice, as the maximum resolution of a Fourier transform is now dictated by the link size, and due care must be taken in interpreting physical results directly from frequency domain data.

This discretization and the periodic boundary conditions along the contour naturally leads to changes in the behaviour of the physics, which must be compensated for [67, 49, 68, 69]. Consider the discrete Fourier transforms of a field $\phi_n$ valued at each lattice site with $n \in [0, N-1]$ for $N$ total sites, as shown in Figure 1.4, and its frequency space counterpart $\tilde{\phi}_k$

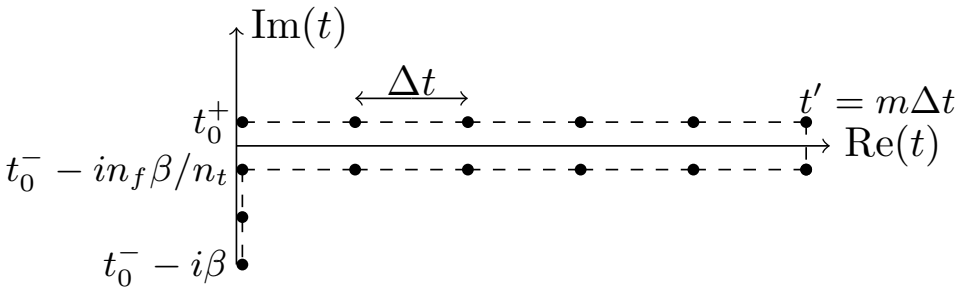


Figure 1.4: A discrete contour. Note that unlike previously, there can be a fixed separation between the two arms of the contour. $n_f/n_t$ dictates the proportion of the imaginary extension that is implemented at $t = t'$. $t'$ itself is an integer ($m$) multiple of the time link size.

$$\Delta\omega\tilde{\phi}_k = \sum_{n=0}^{N-1} \Delta t \phi_n \exp\left[-i\frac{2\pi kn}{N}\right] \tag{1.20}$$

$$\phi_n = \frac{1}{2\pi}\sum_{k=0}^{N-1} \frac{2\pi}{N\Delta t}\Delta t\tilde{\phi}_k \exp\left[i\frac{2\pi kn}{N}\right], \tag{1.21}$$

which allows for easy comparison to the continuous case. These can be summarised

$$\mathrm{d}t \to \Delta t \tag{1.22}$$

$$\frac{2\pi}{N\Delta t} \to \Delta\omega \tag{1.23}$$

$$\omega \to k\Delta\omega \tag{1.24}$$

$$t \to n\Delta t \tag{1.25}$$

$$\tilde{\phi}(\omega) \to \Delta t\tilde{\phi}_k. \tag{1.26}$$

In addition, the finite time derivative can be seen by inspection to be

$$\partial_t\phi_n = \frac{\phi_{n+1} - \phi_n}{\Delta t} \quad . \tag{1.27}$$

By repeated application of (1.27), the second derivative can be found

$$\partial_t \left(\partial_t \phi_n\right) = \frac{\frac{\phi_{n+1}-\phi_n}{\Delta t} - \frac{\phi_n - \phi_{n-1}}{\Delta t}}{\Delta t} \tag{1.28}$$

$$\partial_t \partial_t \phi_n = -\frac{2\phi_n - \phi_{n+1} - \phi_{n-1}}{\Delta t^2}, \tag{1.29}$$

and using these it is possible to define a lattice correction factor $R$,

$$\begin{aligned} \partial_t \phi_n &= \sum_{k=0}^{N-1} \frac{\Delta\omega}{2\pi} \tilde{\phi}_k e^{ikt} \frac{e^{ik\Delta t} - 1}{\Delta t} \\ &= \sum_{k=0}^{N-1} \frac{\Delta\omega}{2\pi} \tilde{\phi}_k iR e^{ikt}, \end{aligned} \tag{1.30}$$

such that

$$iR = \frac{e^{ik\Delta t} - 1}{\Delta t} \approx ik, \tag{1.31}$$

where the $i$ has been included for convenience. The continue $R_{sq}$ can be defined using the second derivative

$$\begin{aligned} \partial_t \partial_t \phi_n &= \sum_{k=0}^{N-1} \frac{\Delta\omega}{2\pi} \tilde{\phi}_k e^{ikt} \frac{-2 + e^{ik\Delta t} + e^{-ik\Delta t}}{\Delta t^2} \\ &= \sum_{k=0}^{N-1} \frac{\Delta\omega}{2\pi} \tilde{\phi}_k e^{ikt} \frac{-2[1 - \cos(k\Delta t)]}{\Delta t^2} \\ &= \sum_{k=0}^{N-1} -\frac{\Delta\omega}{2\pi} \tilde{\phi}_k R_{sq} e^{ikt}, \end{aligned} \tag{1.32}$$

where

$$R_{sq} = \frac{2[1 - \cos(k\Delta t)]}{\Delta t^2}. \tag{1.33}$$

This $R_{sq}$ is the lattice Laplacian, representing a shift from the continuous Laplacian to one set on a fixed lattice. In the limit $\Delta t \to 0$ $R_{sq} \approx k^2$, which can be seen through the application of l'Hopital's rule, recovering the original propagator. This demonstrates the importance of understanding these corrections, as $R_{sq} = k^2 + \mathcal{O}(\mathrm{d}t^2)$ gives insight into the behaviour of the lattice if the link size is set too large. These lattice correction factors are frequently used in Chapters 2 - 4.

## 1.2 Thimble Methods for Complex Integrals

Path integrals, despite their uses outlined in Chapter 1.1, are plagued by the so called 'Sign Problem'. Consider a path integral of the form

$$B = \int_{\mathbb{R}^n} \mathcal{D}\varphi \, e^{-\mathcal{I}(\varphi)}, \tag{1.34}$$

with real variables $\varphi$. Frequently in physics $\mathcal{I}$ will be purely imaginary, often of the form $\mathcal{I}(\varphi) = iS(\varphi)$, meaning the integrand is oscillatory with a constant amplitude but variable phase [67, 70, 71, 72, 73]. This variable phase is the root cause of this sign problem, and makes the integral difficult or impossible to evaluate even using numerical methods. This is due to the subtle cancellations that will occur between each peak and trough in the integrand. These cannot be captured on a computer with finite resolution as the frequency of the oscillations increases [34, 33, 40]. Consequently, the numerical error grows exponentially with the domain of the integral, dwarfing the result for any non-trivial integral [74, 75]. A possible solution to this problem is provided by a multidimensional version of Cauchy's theorem. By promoting the real integration variable $\varphi$ to a complex variable, denoted $\phi$, the integration contour can be deformed into the complex plane without altering the result of the integral, provided no poles are crossed during the deformation. All that is then required is to systematically find an appropriate new contour, where $\mathcal{I}(\phi)$ is now complex valued and damps the oscillations [74, 76, 40, 33, 75, 77, 78, 79, 80].

### 1.2.1 Picard-Lefshetz Thimbles

Picard-Lefshetz Thimbles are integration manifolds, denoted $\mathcal{M}_{PL}$, that match the above criteria [81, 82, 44, 83, 84]. To begin, promote the real integration variable to a complex number $\varphi \to \phi = a+ib$ and deform the integration manifold by solving the flow equation

$$\frac{\mathrm{d}\phi}{\mathrm{d}\tau} = \overline{\frac{\partial \mathcal{I}}{\partial \phi}}, \tag{1.35}$$

where the overbar denotes complex conjugation and $\tau$ represents the mathematical quantity known as 'flow time' [74, 42, 85]. Ideal initial conditions are provided by finding the critical point or points of $\mathcal{I}$, which are defined by

$$\left.\frac{\partial \mathcal{I}}{\partial \phi}\right|_{crit} = 0. \tag{1.36}$$

In practice it takes an infinitely long flow time to move away from a critical point, so the initial conditions should be taken from a small region near the critical point instead which must flow back to the critical point as $\tau \to -\infty$ [86, 83, 87, 1, 2, 88, 89].

It can be seen by applying the chain rule and (1.35) that

$$\begin{aligned} \frac{\mathrm{d}\mathcal{I}}{\mathrm{d}\tau} &= \frac{\partial \mathcal{I}}{\partial \phi}\frac{\mathrm{d}\phi}{\mathrm{d}\tau} \\ &= \frac{\partial \mathcal{I}}{\partial \phi}\overline{\frac{\mathrm{d}\mathcal{I}}{\mathrm{d}\phi}} \\ &= \left|\frac{\partial \mathcal{I}}{\partial \phi}\right|^2, \end{aligned} \tag{1.37}$$

and as the flow time is increased the real part of $\mathcal{I}$ increases monotonically while the imaginary part remains constant as $\phi$ moves away from the critical point. As a result, the integrand in (1.34) is exponentially suppressed as the flow time is increased, while keeping the frequency fixed at the value it had at the critical point. This behaviour gives these paths, denoted $\mathcal{J}$, their name: the paths of steepest descent, as they represent the minimisation of the real part of the exponential [90, 75, 41, 91].

Frequently (1.36) will have multiple solutions, and as these functions are often polynomial, for an $n$th order polynomial, up to $n-1$ solutions can be assumed [74, 90, 45, 92, 79, 1, 93]. Using the requirement that the real part of the integrand suppresses the oscillations we require that $\mathrm{Re}[\mathcal{I}(\phi)] \to \infty$ as $|\phi| \to \infty$ in the complex plane. This allows us to define convergent and divergent regions in the Argand plane of $\phi$. Only the solutions which are in a convergent region as $|\phi| \to \infty$ is the solution that corresponds to the Picard-Lefshetz thimbles. Once

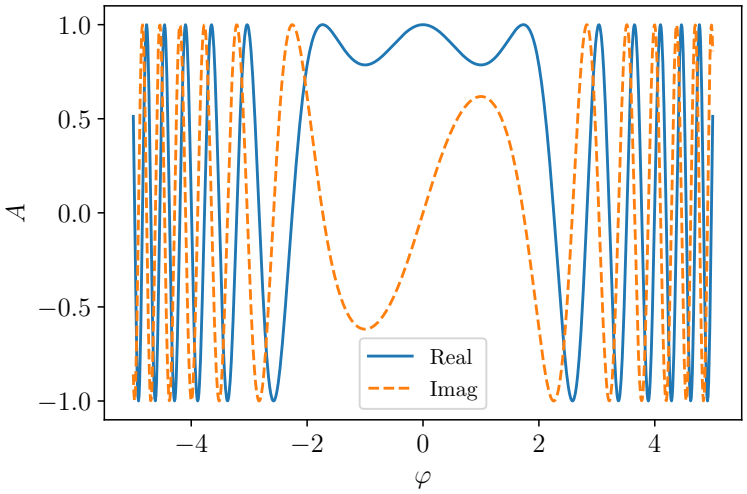


Figure 1.5: The integrand of the Airy function with $z = -1$, labeled $A$ on the y-axis

$\tau$ is taken to infinity, $\mathcal{M}_{PL}$ is a combination of these paths of steepest descent [45, 94, 42, 90, 95]. Examples of these regions are shown in Figure 1.6 where 1.6a corresponds to a simple example which will be continued later, and 1.6b corresponds to the exponent of the integrand of the Airy function with $z = -1$, as shown in Figure 1.5. The Airy function

$$y(z) = \frac{1}{2\pi}\int_{-\infty}^{\infty} \mathrm{d}\varphi \exp\left[i\left(\frac{\varphi^3}{3} + z\varphi\right)\right] \tag{1.38}$$

itself is a useful demonstration of the power of this technique as it is a solution to the Stokes equation, as shown in Appendix A, and is given by

$$\frac{\mathrm{d}^2 y}{\mathrm{d}z^2} = zy, \tag{1.39}$$

and occurs widely in physics, in quantum mechanics as the solution to a particle in a triangular potential well [96], optics [97], and probability [98]. As can be seen from Figure 1.6b, it is not required that the entire thimble exist within convergent regions, only that the thimble is within a convergent region for large $|\phi|$ [90, 99, 100, 101].

While the path of steepest decent of the real part of the integrand has been the most interesting so far, there exists a second path, denoted $\mathcal{K}$, which pre-

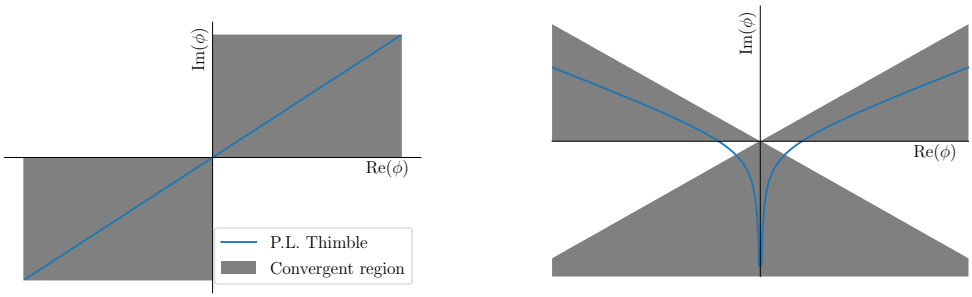


(a) $\mathcal{I} = -\frac{1}{2}i\phi^2$ (b) $\mathcal{I} = -i\left(\frac{\phi^3}{3} - \phi\right)$

Figure 1.6: The convergent regions and thimbles of two simple example functions.

serves the imaginary part while increasing the real part rather than suppressing it [86, 102, 103]. This path of steepest ascent can be found by reversing the sign on the right hand side of the flow equation described in (1.35). When there are multiple critical points given by (1.36), each of these critical points will have a path of steepest decent which could contribute to the deformed integral, though in practice often only the dominant steepest descent paths are considered. However it is not easy to see in advance which critical points create dominant paths and, to exacerbate the problem, paths that initially appeared dominant may undergo cancellations from other paths producing a final result that is controlled by a path which initially appeared sub-dominant [83, 88, 1, 104, 105]. Even worse, which path is dominant can switch very quickly depending on external parameters. This switching is called Stokes Phenomenon and is discussed below.

However it is possible to eliminate some paths' contributions immediately. For a generic number of critical points, indexed by $\sigma$, it can be seen that $\mathcal{J}_\sigma$ and $\mathcal{K}_{\sigma'}$ can cross a maximum of once [106, 91, 102, 107]. This is because along the $\mathcal{J}_\sigma$ contour the real part of $\mathcal{I}$ is decreasing monotonically, while the opposite is true for $\mathcal{K}_{\sigma'}$. As both the steepest decent and ascent paths are created by flowing from the critical point this is the one and only point at which the paths may cross [108, 109, 110, 111]. The intersection of the two paths ($\langle\ ,\ \rangle$) can then be defined

$$\langle \mathcal{J}_\sigma, \mathcal{K}_{\sigma'} \rangle = \delta_{\sigma,\sigma'}. \tag{1.40}$$

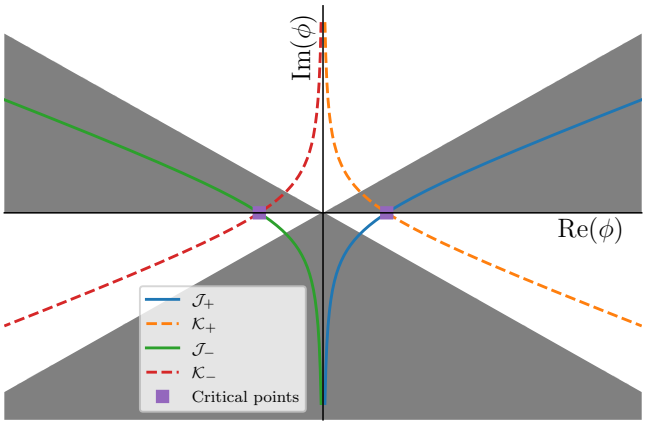


Figure 1.7: The two paths of steepest descent and ascent ascent of the Airy function, with $z = -1$

The real integration manifold, $\mathcal{M}_{\mathbb{R}}$, is equivalent to some combination of these paths, $\sum n_\sigma \mathcal{J}_\sigma$. $n_\sigma$ is defined to be the contribution of the matching path. However, by inserting (1.40) into the intersection between the integration manifold and the path of steepest ascent,

$$\begin{aligned} \langle \mathcal{M}_{\mathbb{R}}, \mathcal{K}_{\sigma'} \rangle &= \sum n_\sigma \langle \mathcal{J}_\sigma, \mathcal{K}_{\sigma'} \rangle \\ &= n_{\sigma'}, \end{aligned} \tag{1.41}$$

it can be seen that the contribution $n_\sigma$ is only non-zero if $\mathcal{K}_\sigma$ crosses the original domain of integration, typically the real axis. As a result, any paths of steepest ascent for which this is not the case can be discarded [104, 112, 91, 113, 114, 115].

A demonstration of this is shown in Figure 1.7, where critical points of the exponent in (1.38) are found to be at $\phi = \pm 1$. Paths of steepest descent are denoted $\mathcal{J}_\pm$, and ascent $\mathcal{K}_\pm$. Both critical points generate paths of steepest descent and both must contribute to the overall thimble, as both paths of steepest ascent cross the real axis. As a result, the thimble depicted in Figure 1.6b is recovered.

To briefly return to Stokes Phenomenon described above, this phenomenon can easily be seen even with models that have already been introduced. Consider

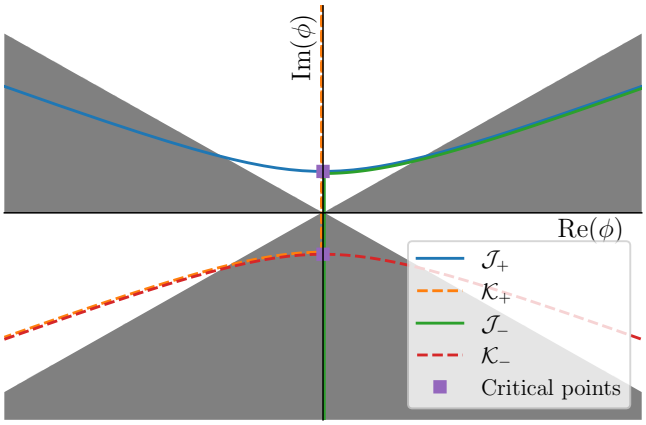


Figure 1.8: The two paths of steepest descent and ascent ascent of the Airy function, with $z = e^{0.01i}$

the solution to the Airy Function (1.38), with $z = e^{0.01i}$. This gives critical points at $\phi_c \approx \pm i$. As before, there are two critical points, however they now lie away from the real axis. This is shown in Figure 1.8. Clearly, the path structure has changed radically. This change is called a Stokes jump, and occurred as $z$ has changed from $-1$ to $e^{0.01i}$. Specifically the jump occurs as $z$ changes through a Stokes ray, a line in $z$ space defined between points where $\mathrm{Im}(\mathcal{I})$ is the same at multiple critical points [75]. For the example of the Airy function, this line is the positive real axis, as for all positive, real $z$ both critical points will be on the imaginary axis, with $\mathrm{Im}(\mathcal{I}) = 0$. Fortunately, in this example $\mathcal{K}_-$ does not cross the real axis, and therefore only $\mathcal{J}_+$ contributes to the overall thimble. Similarly, as will be discussed in Chapter 3, it is shown for the systems considered in this thesis that only a single critical point exists, and therefore only a single path contributes to the thimble, and the issue of Stokes jumps is circumvented.

Although the integrand along the thimble has a constant phase by construction, a small variable phase remains due to the transformation between manifolds, which is shown in (1.54), by the constant, but complex valued, $\det(J)$. This is referred to as the 'residual sign problem' [81, 94, 114, 112, 1, 114, 115]. There is also a second potential source of phase variance in the case where two or more thimbles exist. Although the thimbles are linked, the requirement that $\mathrm{Im}[\mathcal{I}]$ is

constant applies individually to each thimble. As a result, there can be a discrete jump in the phase of $\mathcal{I}$ at the connection. This is referred to as the 'global sign problem' [81, 112, 1]. Usually both of these effects are small enough that traditional techniques can resolve them, but can be a continued source of problems [104, 91].

Combining all of the above with the need to find the critical point for a non-trivial $\mathcal{I}$ it is obvious why a full Picard-Lefshetz thimble can be problematic to calculate on a computer. What is needed is a method that does not rely on isolating the critical points and can be done in general, regardless of the number of integration variables or number of paths of steepest descent.

**Picard-Lefshetz Example**

Using $\mathcal{I}(\varphi) = -\frac{1}{2}i\varphi^2$ as a toy model and complexifying $\varphi \to \phi$, it can be seen that by (1.35) the flow equation is

$$\frac{\mathrm{d}\phi}{\mathrm{d}\tau} = -\overline{i\phi} \tag{1.42}$$

and a single critical point as per (1.36) at $\phi = 0$. By writing $\phi = a + ib$ and separating the real and imaginary parts (1.42) gives

$$\dot{a} = b, \quad \dot{b} = a, \tag{1.43}$$

and by taking the derivative with respect to the flow time again gives

$$\ddot{a} = \dot{b} = a \tag{1.44}$$

$$\ddot{b} = \dot{a} = b. \tag{1.45}$$

These can be solved in the usual way, and using the boundary condition provided by taking the flow time to $-\infty$ will set $a, b = 0$ due to the critical point. This

leads to

$$\begin{aligned} a &= Ae^{\tau}, \quad b = Be^{\tau} \\ \dot{a} &= Ae^{\tau}, \quad \dot{b} = Be^{\tau} \\ b &= Ae^{\tau}, \quad a = Be^{\tau}, \end{aligned} \tag{1.46}$$

by using the derivatives in (1.43), and by comparing the first and third lines of (1.46) shows that $a = b$. It is obvious in this example that this thimble contributes to the integral, as firstly it is the only thimble present due to the action having only one critical point, and secondly the critical point is on the real axis and therefore the path of steepest ascent must pass through the axis. However as it can be found simply, it is included here for completeness' sake. By changing the sign on the right hand side of (1.42) and propagating this change through the same steps as above, we find that for the steepest ascent path, $a = -b$ instead. This does cross the real axis as expected.

Fortunately, as the example given here has only one integration variable, a second method may be used to verify this. By noting that along the thimble $\mathrm{Im}[\mathcal{I}(\phi)]$ must be constant and separating the real and imaginary parts of $\phi \to a + ib$ in the usual way, we see that

$$\mathrm{Im}[\mathcal{I}(\phi)] = -\frac{1}{2}(a^2 - b^2) = K, \tag{1.47}$$

where $K$ is the constant phase. It is also known that the thimble passes through the critical point at $\phi = 0$, and this can be used to fix $K = 0$. As a result this method also recovers $a = \pm b$ in a far more compact way. Unfortunately however this method does not make any distinction between finding the thimble or the path of steepest ascent, and if this method alone is being used knowledge of the convergent regions as shown in Figure 1.6a is required to identify which path is which.

**Evaluation of the Integral**

The knowledge gained earlier in this section can be used to evaluate the integral

$$T = \int_{-\infty}^{\infty} \mathrm{d}\varphi \; e^{-\mathcal{I}} = \int_{-\infty}^{\infty} \mathrm{d}\varphi \; e^{i\varphi^2/2}. \tag{1.48}$$

Following the procedure outlined above, complexify $\varphi \to \phi$, and the structure of the thimble is known from the above to be $\phi = a(1+i)$, which also gives

$$\phi^2 = 2ia^2 \tag{1.49}$$

$$\frac{\mathrm{d}\phi}{\mathrm{d}a} = 1 + i. \tag{1.50}$$

This allows for a change of variables in (1.48) such that

$$T = \int_{-\infty}^{\infty} \mathrm{d}a(1+i)e^{-a^2}, \tag{1.51}$$

which can be evaluated as a standard Gaussian integral to give

$$T = (1+i)\sqrt{\pi}. \tag{1.52}$$

This technique gives the same result as performing an analytic continuation of a normal Gaussian integral as shown in Appendix B. This technique has taken an integral that would have been intractable by normal numerical means and requires analytic continuation to evaluate, and transformed it into the standard Gaussian seen in (1.51) which could be tackled by any solver. Although for this example, other tools are available for verification this technique can be applied to many new situations.

### 1.2.2 Generalised Thimbles

As outlined in Section 1.2.1, the full Picard-Lefshetz thimble method has significant problems. However by noting that regardless of initial conditions the flow process leads asymptotically to the Picard-Lefshetz thimble, an example of

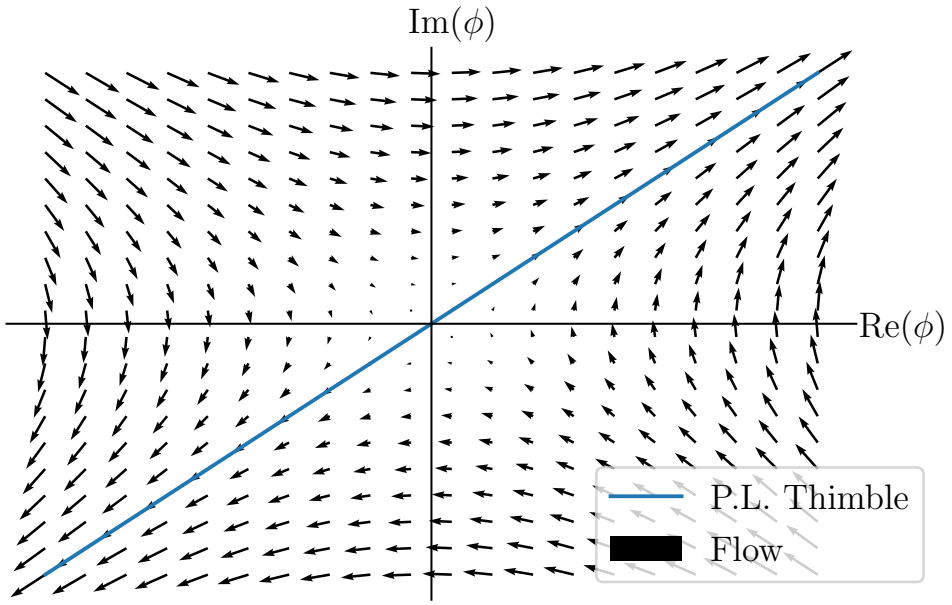


Figure 1.9: The direction of flow for any point in the Argand plane

which is shown in Figure 1.9, a significant number of these problems can be avoided [42, 47, 48, 2]. Consequently the entire integration manifold can be flowed for some fixed flow time, which is typically finite, $\tau_{max}$ to create a so called 'Generalised Thimble'. This Generalised Thimble, if taken with $\tau_{max} = \infty$ automatically captures the correct combination of Picard-Lefshetz thimbles regardless of the number of critical points [42, 1]. By doing this there is no need to calculate the critical point of the function $\mathcal{I}$. This greatly simplifies the implementation on a computer. However, in compromise, the effectiveness of the thimble in reducing the sign problem is reduced inversely with the magnitude of $\tau_{max}$.

By starting with the real n-dimensional integration manifold $\mathcal{M}_R = \mathbb{R}^n$, and applying the flow equation, we can create a generalised thimble manifold $\mathcal{M}_\tau$ and define a Jacobian matrix

$$J_{ij} = \frac{\partial \phi_i}{\partial \varphi_j} \tag{1.53}$$

to transform between the two. This allows the integral to be written as

$$\begin{aligned}\int_{\mathcal{M}_{\mathcal{R}}} \mathcal{D}\varphi\, e^{-\mathcal{I}(\varphi)} &= \int_{\mathcal{M}_{\tau}} \mathcal{D}\phi\, e^{-\mathcal{I}(\phi)} \\ &= \int_{\mathcal{M}_{\mathcal{R}}} \mathcal{D}\varphi\ \det(J) e^{-\mathcal{I}(\phi)}\end{aligned} \tag{1.54}$$

and doing so reveals an important part of this approach: by transforming the integrand onto a thimble the details of the integral are written in the transform, not the integral itself [116, 1, 2, 42].

Clearly it is extremely important to calculate $J$, and it will become more important still in later chapters. Fortunately this calculation is not mathematically difficult (although computationally it poses problems, see Chapter 2), as by combining the flow equation (1.35) and the definition of the Jacobian (1.53) yields

$$\frac{\mathrm{d}}{\mathrm{d}\tau} J_{ij} = \sum_{s} \overline{\frac{\partial^2 \mathcal{I}}{\partial\phi_i \partial\phi_s}} J_{sj}, \tag{1.55}$$

noting that the initial conditions require that at $\tau = 0$, $J = \mathbb{I}$.

A note of caution must be expressed however. In practical usage, generalised thimbles will usually be applied to problems using an MCMC technique to probe the manifold generated to create samples to evaluate integrals of the form in (1.54). This works well, as presented later in this work. However as it is not possible to take $\tau$ to infinity on a computer, the generalised thimble will only ever be an approximation of the Picard-Lefshetz thimble. This is relevant when two paths of steepest descent connect, such as from a form of $\mathcal{I}$ with multiple critical points, as the region between the paths will highly distorted and difficult to probe. This can lead to simulations getting trapped behind high potential walls in such areas and efficiency gains in this class of problem are the subject of ongoing study [104, 117, 84, 107, 79]. Despite the fact that these Generalised Thimbles are approximations of Picard-Lefshetz thimbles, the results acquired by their use are not. This is because a Picard-Lefshetz thimble eliminates the Sign Problem completely along a specific path (although still suffers from the residual sign problem), while the Generalised Thimble simply reduces it to a

manageable level, suppressing the worst of the oscillations, this is shown in Figure 1.10. It is important to stress however, that both results are exact rather than approximations, as both the combination of Picard-Lefshetz thimbles and the Generalised Thimbles are exact re-writings of the integral, and are therefore precisely equivalent to the original.

### Generalised Thimble Example

This section reuses the example given in Section 1.2.1 for comparison, $\mathcal{I}(\varphi) = -\frac{1}{2}i\varphi^2$. Complexifying and separating in the same way as above $\phi \to a + ib$, and noting that $\phi(\tau = 0) = \varphi$ as the entire real manifold is being flowed rather than a small region around the critical point. For this example, (1.35) gives

$$\begin{aligned} a &= \varphi \cosh(\tau) \\ b &= \varphi \sinh(\tau). \end{aligned} \tag{1.56}$$

These can then be combined to give

$$b = \tanh(\tau)a, \tag{1.57}$$

which, in the limit $\tau \to \infty$ recovers the thimble $a = b$, as calculated in Section 1.2.1. This example is also shown for a variety of flow times in Figure 1.10. Figure 1.10a shows the generalised thimble contour for a range of flow times from 0 to $\infty$, and demonstrates graphically that as the flow time increases the generalised thimble converges to the Picard Lefshetz result. Figures 1.10b through 1.10f show the integrand along the respective contour, suppressing the sign problem as $\tau$ increases. Clearly Figure 1.10b is intractable over a large domain, but for even low flow times, such as $\tau_{max} = 0.1$ this simple case can be rendered trivial for a numerical solver.

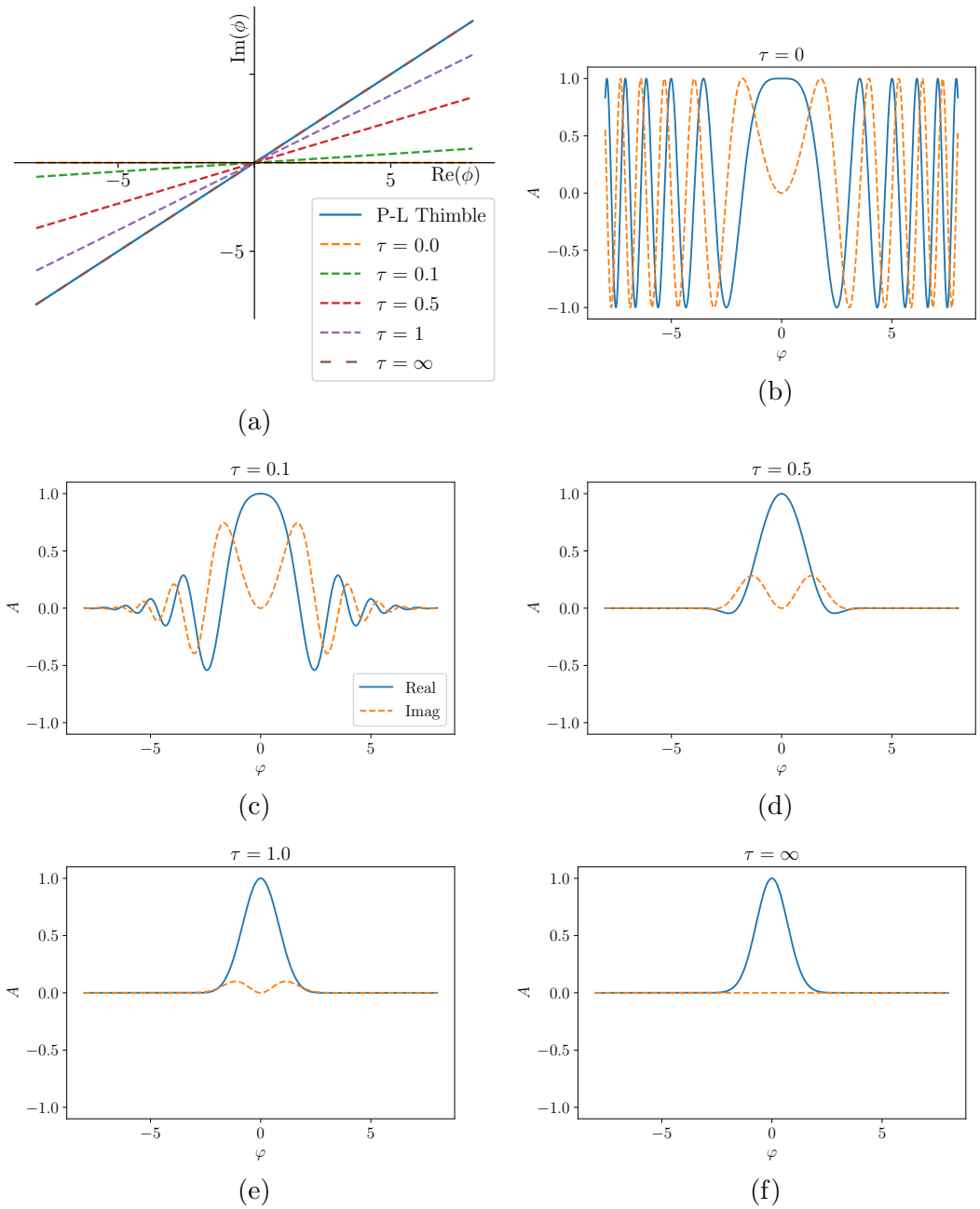


Figure 1.10: The Picard-Lefshetz thimble and Generalised Thimbles for a range of flow times, and the respective integrands.

### 1.2.3 Comparison to Langevin Dynamics

There are significant similarities between the Langevin approach and the thimble methods outlined above. Both methods rely on the complexification of real integration variables to suppress the sign problem, and find the imaginary component of the variable by introducing a flow process along a 'mathematical' i.e. non-physical time-like parameter [118, 119, 120, 116, 121, 122]. In Picard-Lefshetz theory, this flow time $\tau$ is used to map the thimble from a critical point as seen above. In Langevin dynamics however the flow equations are written with flow parameter $t_5$. After complexifying $\varphi \to \phi$ in the usual way the flow is given by

$$\frac{\mathrm{d}\phi}{\mathrm{d}t_5} = -\frac{\partial \mathcal{I}}{\partial \phi} + \eta, \tag{1.58}$$

where $\eta$ represents a real Gaussian noise term [110, 123, 124, 116, 125, 126]. It can clearly be seen that in the absence of the noise term, this is a gradient descent optimisation equation. The noise term ensures that the solution does not become trapped in the first local minima it encounters [127, 128, 129, 130, 131] and improves the overall stability of the simulations. Combined with adaptive step size numerical solvers can suppress the problem entirely [132, 38, 133]. Although (1.58) clearly resembles the flow equation (1.35) for thimble calculations, it is important to note the lack of the conjugation on the right hand side.

Langevin dynamics has seen enormous success, it has been used to accurately map the QCD phase diagram [120], calculate correlation functions [48], model biological ion gate interactions [134], diffusion in polymers [135], among a huge array of others [136]. For a formal derivation of the method and how the probability weights change see [37].

A toy model, heavily inspired by [137], has been included for discussion. This model is a $0+0$D model, with a real action of the form

$$S(\phi) = \frac{\mu}{2}\phi^2 + \frac{\lambda}{4!}\phi^4, \tag{1.59}$$

with $\mu = \pm 1$ and $\lambda = 0.4$, with key results of this toy model shown in Figure 1.11. The model was then run for $10^5$ update steps. It is important to note here that integrals of exponetials with arguments of the from of (1.59) can be solved using Bessel functions. However, as this is a toy model for demonstration, it is treated using Langevin and compared to a generalised thimble.

For reference the shape of the action in both values of $\mu$ is shown in Figures 1.11a and 1.11b. In the one well case, the Langevin technique conforms well in the distribution of $\phi$ values as would be expected from an action of this shape as shown in Figure 1.11c. However once a second well is introduced in 1.11d, the model starts to show issues, appearing to overly weight the negative well over the positive well. Figure 1.11b however shows that this is not because the simulation has stuck in one well or the other, as the simulation frequently jumps between the two. This indicates that system would even itself out over a longer simulation. As expected however the simpler one well model forms nicely around the expected value at the minima in Figure 1.11e. Figures 1.12a - 1.11j show the behaviour of the expectation values of two simple observables as the simulation runs. For the $\langle\phi\rangle$ case the one well model rapidly converges within $2 \times 10^4$ steps, however even by the end of the simulation the two well model shows poor convergence with the expected result. The $\langle\phi^2\rangle$ results do not converge well either. Neither model converges completely, nor shows any significant improvement with increased simulation length.

Analytic results for the probability distributions in Figures 1.11c, 1.11d were found using $\exp(-S(\phi))$. The analytic values for the distributions in 1.11e, 1.11f are the minima of the respective actions. The analytic mean values were found in the usual way for a continuous distribution

$$\langle\phi^n\rangle = \frac{\langle\phi^n e^{-S}\rangle}{\langle e^{-S}\rangle}. \tag{1.60}$$

The simulation above was repeated using a thimble technique for comparison, as shown in Figure 1.12, which was updated using the same MCMC method that will be described later in Chapter 2 for the use in simulations. For ease of comparison,

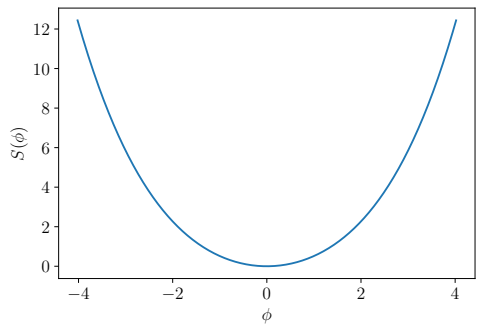


(a) The action for the $\mu = 1$ case.

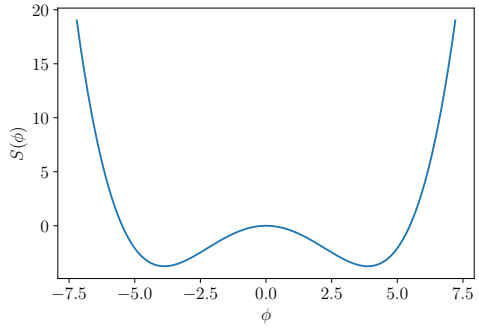


(b) The action for the $\mu = -1$ case.

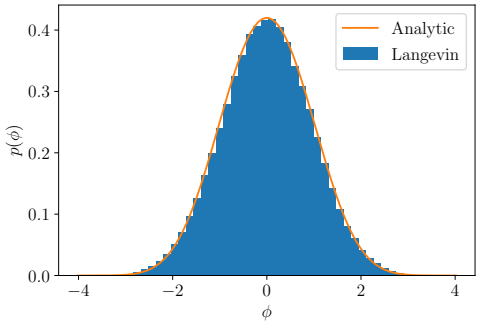


(c) The analytic and numerical probability distributions for the $\mu = 1$ case.

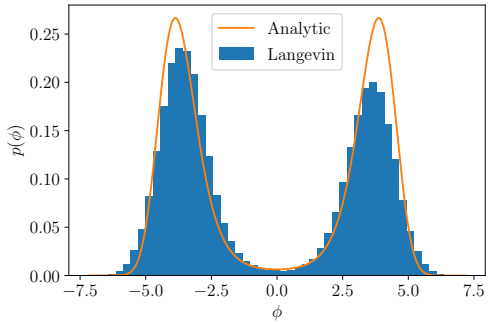


(d) The analytic and numerical probability distributions for the $\mu = -1$ case.

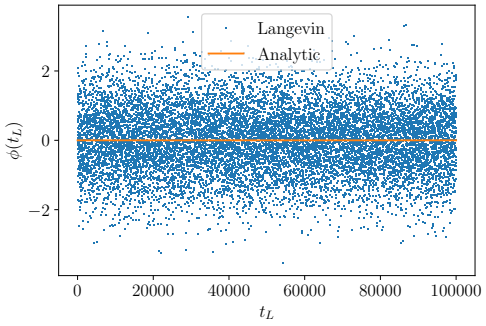


(e) The distribution of Langevin points around the analytic minimum in the $\mu = 1$ case.

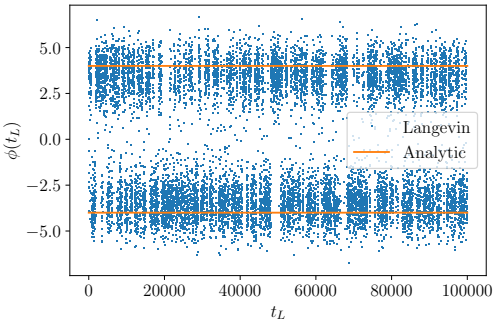


(f) The distribution of Langevin points around the analytic minima in the $\mu = -1$ case.

Figure 1.11: Showing a comparison of parameter behaviours between models.

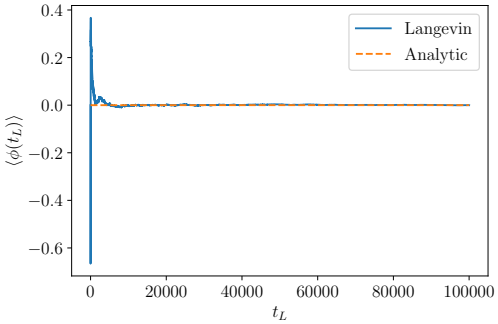


(g) Running average of the expectation value of $\phi$ compared to the analytic solution for the $\mu = 1$ case.

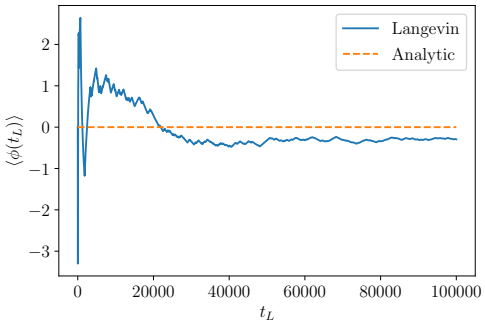


(h) Running average of the expectation value of $\phi$ compared to the analytic solution for the $\mu = -1$ case.

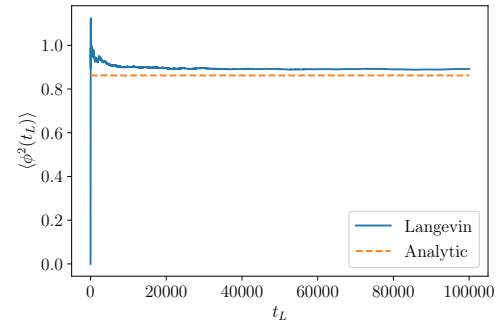


(i) Running average of the expectation value of $\phi^2$ compared to the analytic solution for the $\mu = 1$ case.

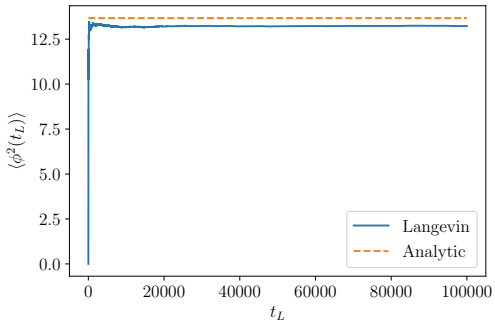


(j) Running average of the expectation value of $\phi^2$ compared to the analytic solution for the $\mu = -1$ case.

Figure 1.11: Showing a comparison of parameter behaviours between models.

the flow time was set $\tau_{max} = 0.8$ and the simulation was run for $5 \times 10^4$ update steps. These parameters gave a comparable wall clock run time to the Langevin case, while the reduction in the number of update steps can be justified as the results converge well within it. This is notably faster (in terms of update-time) compared to the Langevin case and to be expected; the thimble technique is, in principle, exact (although obviously numerically implemented and solved using a MCMC techniques here) while the Langevin technique inherently relies on random noise, and therefore cannot be considered exact in the same way. However this also brings in Langevin's greatest strength compared to thimble techniques; computational resources. Each MCMC update of this simulation has required the solution of four, coupled differential equations from (1.35) and (1.55) once separated into their real and imaginary parts. If convergence is guaranteed, and the results are comparatively simple an accurate expectation value for $\phi$ could be found in the one well case in 20% of the wall clock time, had the simulation been terminated early. However, it also demonstrates the strength of the thimble technique, as the thimble simulations reliably return all four observables, three of them faster than the Langevin simulations, and does not seem to struggle with the bimodal distribution in the two well case. However, it can be shown using the Fokker-Planck equation that the Langevin technique will always converge when using a variable step size if the action is real (as in this case) [138, 139]. Even in such a case, corrections for finite step size must be made before determining the accuracy.

Unfortunately, despite significant early success, the Langevin technique has been found to suffer from general convergence issues [121, 140, 141]. A particularly relevant physical example of this problem is in the case of an equilibrium simulation the correlator function

$$\langle \mathcal{O}_1(t)\mathcal{O}_2(t')\rangle = \mathrm{Tr}\left(e^{-\beta H}\mathcal{O}_1(t)\mathcal{O}_2(t')\right), \tag{1.61}$$

will not converge unless $t - t' < \beta$ where $\beta$ is the inverse temperature and given by $1/k_B T$ [1, 142, 143]. A bigger issue is where the technique converges but to an incorrect result [132, 144, 145]. A posteriori conditions for correctness have since

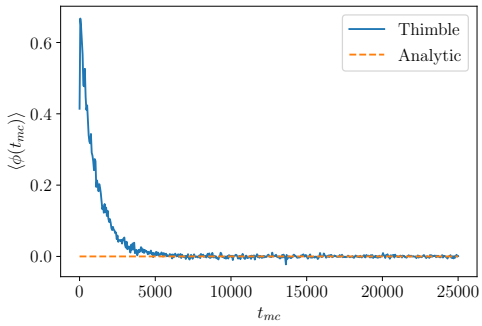


(a) Running average of the expectation value of $\phi$ compared to the analytic solution for the $\mu = 1$ case.

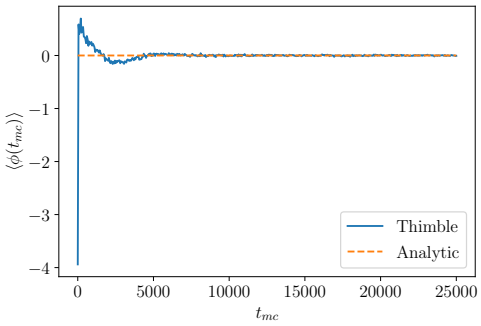


(b) Running average of the expectation value of $\phi$ compared to the analytic solution for the $\mu = -1$ case.

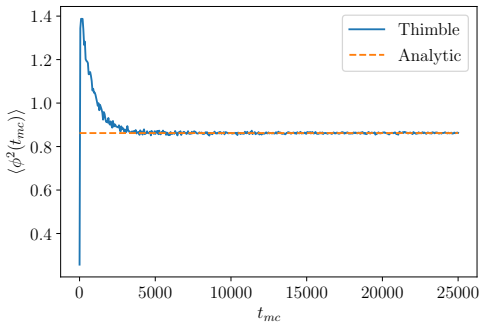


(c) Running average of the expectation value of $\phi^2$ compared to the analytic solution for the $\mu = 1$ case.

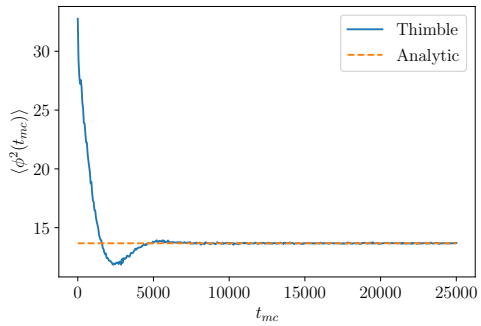


(d) Running average of the expectation value of $\phi^2$ compared to the analytic solution for the $\mu = -1$ case.

Figure 1.12: Showing a comparison of parameter behaviours between models using a generalised thimble technique

been developed, however commitment of significant computational resources to a technique who's validity can only be validated once results have been calculated can present its own challenge.

# Chapter 2

# Equilibrium Simulations

Before applying this new technique to non-equilibrium systems, it was first applied to well understood equilibrium situations to verify it. In order to do so the physical results of [1, 2] were reproduced and used as a basis for exploring more complicated systems.

## 2.1 Equilibrium $0+1D$ Correlators

In the equilibrium $0+1D$ case, a periodic lattice was set up as per Figure 1.4. A corresponding discretized action

$$\mathcal{I} = -i\sum_{j=0}^{N}\left[\frac{\left(\phi_j-\phi_{j-1}\right)^2}{2\Delta t_j}+\left(\frac{\Delta t_j+\Delta t_{j-1}}{2}\right)\left(-\frac{1}{2}m^2\phi_j^2-\frac{\lambda}{4!}\phi_j^4\right)\right], \tag{2.1}$$

where $\Delta t_j$ varies with position along the contour such that

$$\Delta t_j = \begin{cases} \mathrm{d}t & 0 \le j < N_t \\ -i\mathrm{d}t & N_t \le j < N_t + N_\beta/2 \\ -\mathrm{d}t & N_t + N_\beta/2 \le j < 2N_t + N_\beta/2 \\ -i\mathrm{d}t & 2N_t + N_\beta/2 \le j < N_t + N_\beta, \end{cases} \tag{2.2}$$

and $N = 2N_t + N_\beta$ was set up. The $(\Delta t_j + \Delta t_{j-1}/2)$ term exists to smooth the behaviour at the contour's 'corners'. This lattice was then flowed in the manner outlined in Section 1.2.2 to create a generalized thimble which could be sampled to compute correlation functions. This is done by noting that for any operator

$$\left\langle \hat{\mathcal{O}}(t) \right\rangle = \frac{\int \mathcal{D}\phi \; e^{-\mathcal{I}(\phi)} \hat{\mathcal{O}}}{\int \mathcal{D}\phi \; e^{-\mathcal{I}(\phi)}} = \frac{\left\langle e^{-i\mathrm{Im}[\mathcal{I}(\phi)] + i \arg[\det(J)]} \hat{\mathcal{O}} \right\rangle_P}{\left\langle e^{-i\mathrm{Im}[\mathcal{I}(\phi)] + i \arg[\det(J)]} \right\rangle_P}, \tag{2.3}$$

where the expectation values are evaluated by Monte-carlo sampling the integrals over a distribution P, defined as

$$P(\phi) = e^{-\mathrm{Re}[\mathcal{I}(\phi)] + \ln|\det(J)|}. \tag{2.4}$$

This process is typically called reweighting. It is generally ineffective and can lead to convergence to incorrect results, as the phase of the denominator fluctuates as seen in Chapter 1.1, and the expectation value will converge to a value dictated more by the sampling rate than the true value. This, fortunately, is not the case when using thimbles with sufficient flow time, as the sign problem is suppressed, as the argument of $\det(J)$ will act to reduce the oscillations, and move the expected value away from 0. For further details see [1].

Although (2.4) initially looks like a phase-quenched weight, such as the one presented in [116], as the matrix refers to the transformation between manifolds not (for example) the fermion matrix. Consequently, the use of this weight does not introduce the overlap problem, where importance sampling is suppressed due to distortions between 'important' regions of the parameter space by the matrix.

The validity of using (2.4) can be seen using (1.54), as the complex Jacobian determinant term can be combined with the existing exponential. Real terms can then be separated to provide the weight during the Markov process and improve convergence times. The result is then reweighted by the remaining imaginary parts to give a physical result. Unlike [1] however, the proposals were drawn on the complex manifold $\mathcal{M}$ and transported to the real manifold using the Jacobian. This maintained the requirement that the proposals be isotropic on the complex

manifold, without attempting to adjust the proposals on the real manifold to account for the distortion introduced by the flow process.

The algorithm used to generate samples is critical for this work. It is required that a Markov chain of states is constructed. For each of these states, the generalised thimble must be calculated, and a proposal for the next state on the thimble. This algorithm is outlined here:

1. Flow the system to $\tau_{max}$ using (1.35) and create the Jacobian using (1.55) which transforms the real valued vector of field values across the lattice, $\varphi$, in state $n$ $\varphi_n \to \phi_n$.

2. Create a complex proposal vector $\eta$ on the manifold created in step 1 by drawing $2N$ values from a normal distribution $\exp\left(-\eta^\dagger\eta/\delta^2\right)$, where $N$ is the number of lattice sites to populate both real and imaginary parts of $\eta$.

3. Transport the proposal vector to the real manifold by solving $\eta = J\Delta$ for the real space proposal $\Delta$. This is equivalent to having drawn the elements of $\Delta$ from a distribution given by

$$g(\phi_{n+1}|\phi_n) = \frac{|\det J_n|}{\sqrt{\pi^{N_{tot}}\delta^{2N_{tot}}}} e^{-\Delta^T J_n^\dagger J_n \Delta/\delta^2} \tag{2.5}$$

   instead, which is isotropic along the thimble manifold. Unfortunately, values cannot be drawn from this distribution directly, as the vector-matrix product in the exponent makes this a non trivial distribution on the real manifold.

4. Create a new state $\varphi_{n+1} = \varphi_n + \mathrm{Re}(\Delta)$. Although mathematically $\Delta$ is already purely real, numerical error in the calculation and use of $J$ results in non-zero imaginary parts of $\Delta$. This ensures the real manifold remains purely real.

5. Create a new proposed manifold by flowing $\varphi_{n+1}$ in the same manner as for $\varphi_n$ in step 1.

6. Accept the proposal with a probability

$$Pr = \min\left(e^{\mathrm{Re}(\mathcal{I}_n)-\mathrm{Re}(\mathcal{I}_{n+1})+2\ln|\det J_{n+1}|-2\ln|\det J_n|+\Delta^T(J_n^\dagger J_n)\Delta/\delta^2-\Delta^T(J_{n+1}^\dagger J_{n+1})\Delta/\delta^2}, 1\right) \tag{2.6}$$

7. Store the result, regardless of the acceptance.

This process is repeated until a Markov Chain of sufficient length is generated. Here $\delta$ is a parameter used to control the size of the proposal and correspondingly the step size around the manifold. The acceptance probability is calculated in the usual way for the Metropolis-Hastings algorithm,

$$Pr = \min\left(\frac{P(\phi_{n+1})}{P(\phi_n)}\frac{g(\phi_n|\phi_{n+1})}{g(\phi_{n+1}|\phi_n)}, 1\right), \tag{2.7}$$

where $P(\phi)$ is given in (2.4) and $g(\phi_{n+1}|\phi_n)$ is the probability of proposing state $\phi_{n+1}$ given state $\phi_n$ as used in (2.5). This was found to be systematically reliable for flow times up to $\tau_{max} = 0.25$, with a fixed step size $\delta = 0.1$, unit mass, $\mathrm{d}t = 0.2$, $\lambda \in [0, 24]$, $N_t = 12$, $N_\beta = 4$, and simulations were run for $5 \times 10^6$ Monte Carlo steps after the burn in. This process was completed for time separated correlators, as shown in Figure 2.1. Clearly the results for $\lambda = 24$ match the work done in [1] well, despite the slight variation in the proposal production mechanism and acceptance probability. The LU decomposition was employed to calculate the determinant of $J$ directly. This decomposition was also used to solve the matrix equation in step 3. By drawing isotropic proposals on the complex manifold and transporting them to the real manifold for use, the problems introduced by the distortions along the flow path are not encountered meaning that the proposals do not need to be adjusted by an estimate of the action, as was done in [1]. These changes appear to have improved the convergence rate of the Markov chain, as comparable results were found with only 50% of the update steps.

The parameters used here match those in [1], and unfortunately due to the short

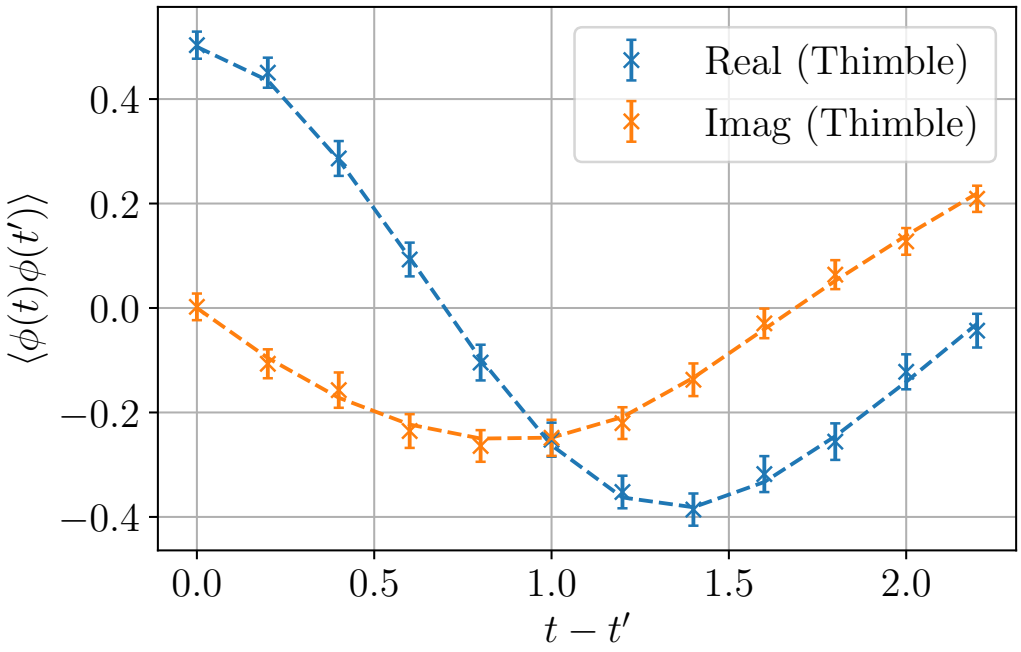


Figure 2.1: Matching the time separated correlator results from [1]. The dashed line represents the results found by numerically solving the quantum mechanical case using the technique that will be described in Section 4.4

link size and small lattice, the maximum time difference is small. However, qualitatively, these results match the form of those later in the chapter which were performed with longer link sizes and consequently larger time differences, and longer time behaviour may be reasonably inferred from them.

It is worth noting that this method of updating a lattice is unusual. Typically a single site is chosen to be updated [146]. This is done so that a beneficial change in one region of the lattice is not rejected due to a larger detrimental change in another region, and as the proposals for each site should be independent, it makes no difference if a single site is considered or all sites at once. Computationally the improved convergence due to not rejecting beneficial updates outweighs the increased cost of recomputing the transition probability at each update. Unfortunately, this is not the case for the method employed here. Due to the high cost of both the flow process and the calculation of the determinant of the Jacobian, calculating this for each site update would not be practical. Consequently updates are performed by 'sweeping' the entire lattice at once. This naturally

results in small scale proposals to improve the acceptance rate.

Having established that these results match literature well, a further set of simulations were run with a much larger link size $\mathrm{d}t = 0.75$, and a reduced coupling of $\lambda = 4$. This was done in part to test the large $t$ behaviour and check that it was consistent, while as a by product allowing the flow time to be set much higher. As shown in Sections 1.2.1 and 1.2.2, the flow is very sensitive to the action. Decreasing the link size, which appears inversely in the kinetic term, can cause the RHS values of (1.35) and (1.55) to rapidly blow up. This can cause an adaptive step solver to become impractically slow, or worse cause a numerical overflow if the link size is set too small. However, as will be shown later, increasing the flow time is critical to finding results in reasonable wall clock time.

This proved to be successful. The increased lattice spacing and increased flow time ensured that the results were convergent much quicker. A correlator generated with only $10^5$ MCMC updates with a flow time of $\tau = 2$, as shown in Figure 2.2 has smaller error while covering a much greater span of real time. In general, these characteristics were preferred, and moving forward all $0+1D$ simulations were run with larger link sizes and corresponding flow times. The time separated correlator behaves as expected from the free theory and quantum mechanics, the free correlator forms a sine wave, the period of which is set by the mass, and the phase set by difference in the times considered. The coupled case is similar with a lower period, and is distorted, as expected from perturbation theory. The simulations here are performed with unit mass, and each plot represents a different pair of $\langle \phi_i \phi_j \rangle$ correlators. This combination of link size and lattice size was chosen to capture at least one elementary oscillation of the system. Unfortunately, further time was not calculated due to the computational cost of adding new lattice sites and the associated Jacobian calculation.

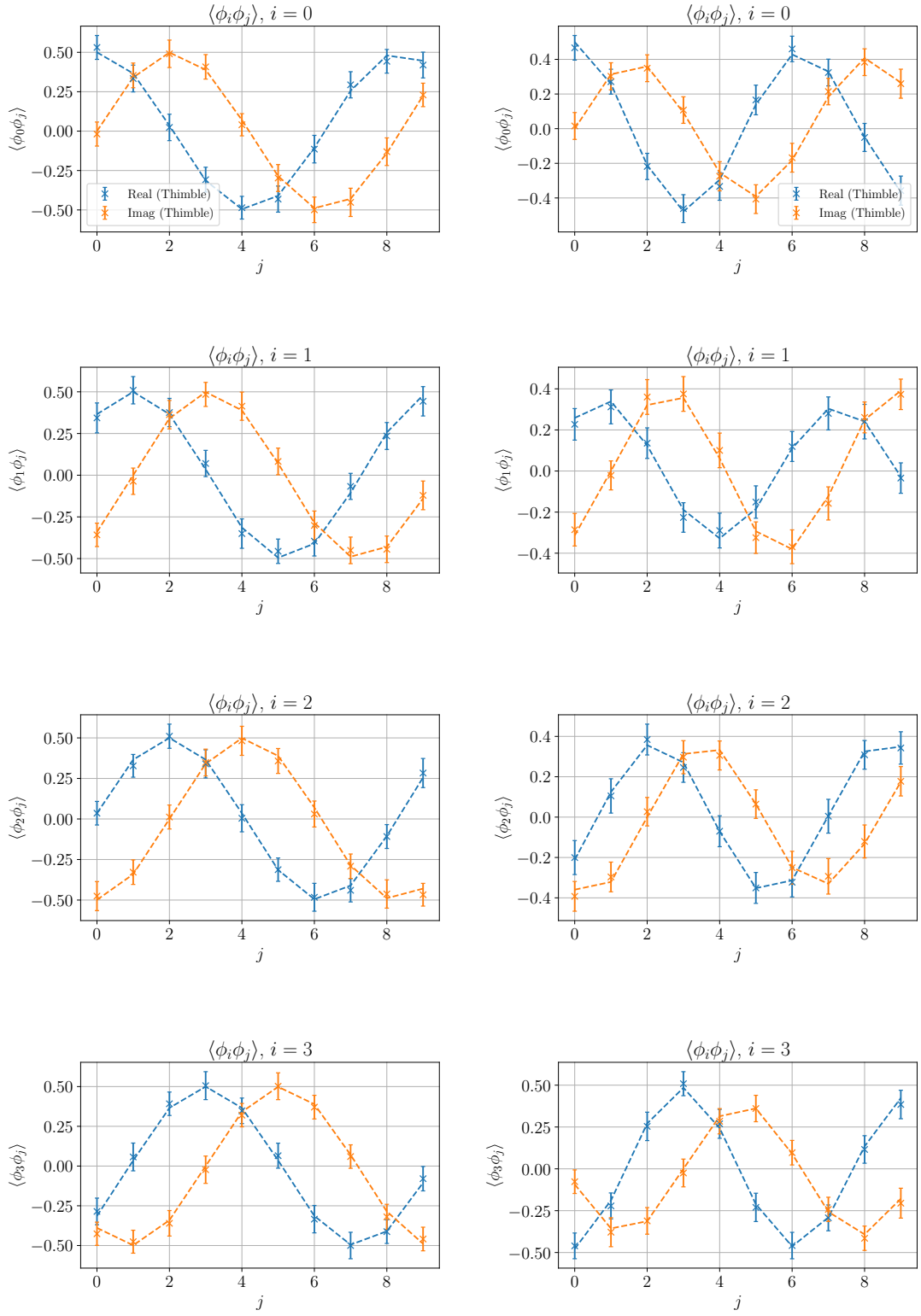


Figure 2.2: A range of time separated correlataors in the free case (left) and coupled $\lambda = 4$ case (right). The link size of $\mathrm{d}t = 0.75$ means that this covers more than three times the physical time as the case shown in Figure 2.1. As before, the dashed line represents the semi-analytic solution.

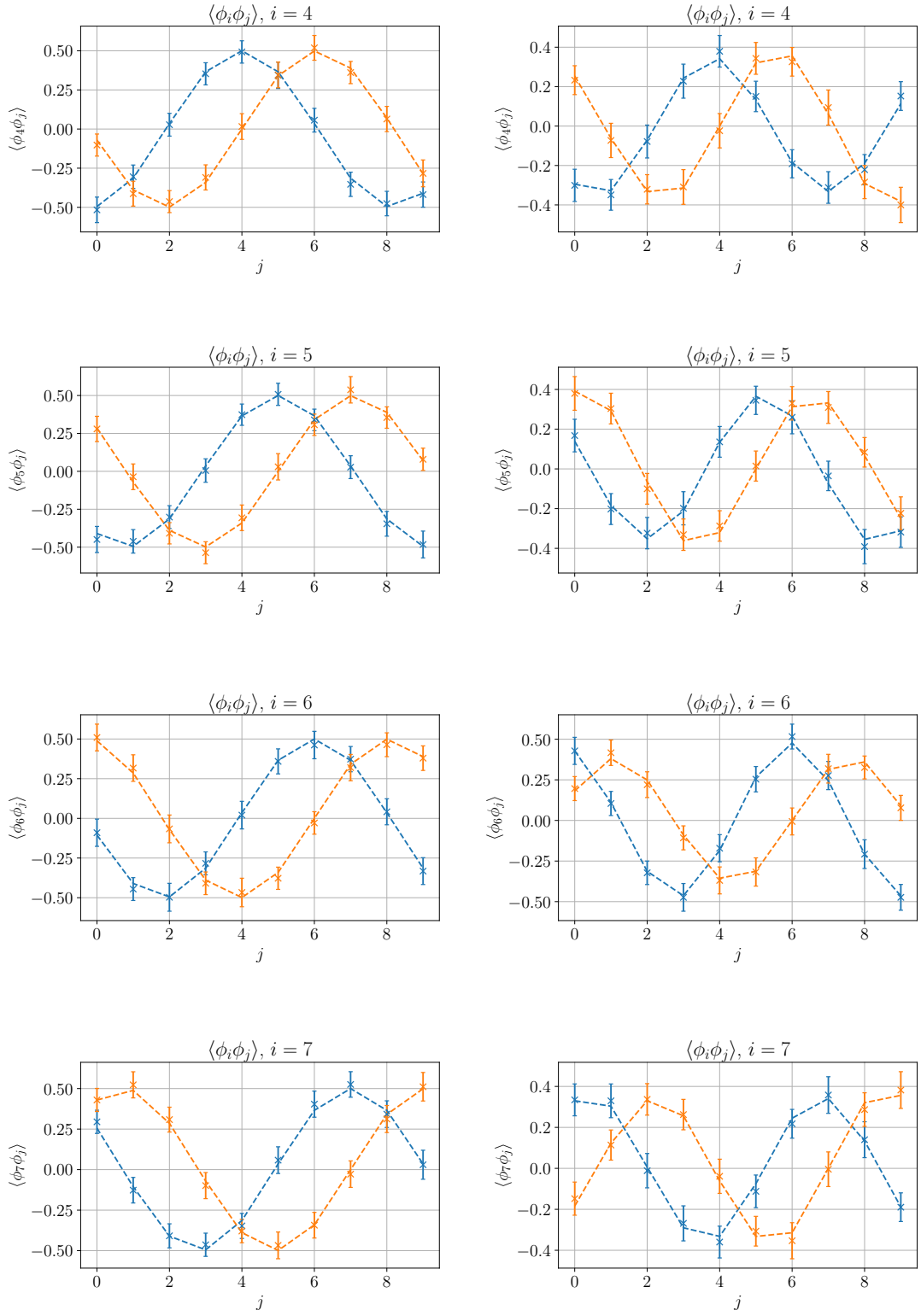


Figure 2.2: A range of time separated correlataors in the free case (left) and coupled $\lambda = 4$ case (right). The link size of $\mathrm{d}t = 0.75$ means that this covers more than three times the physical time as the case shown in Figure 2.1. As before, the dashed line represents the semi-analytic solution.

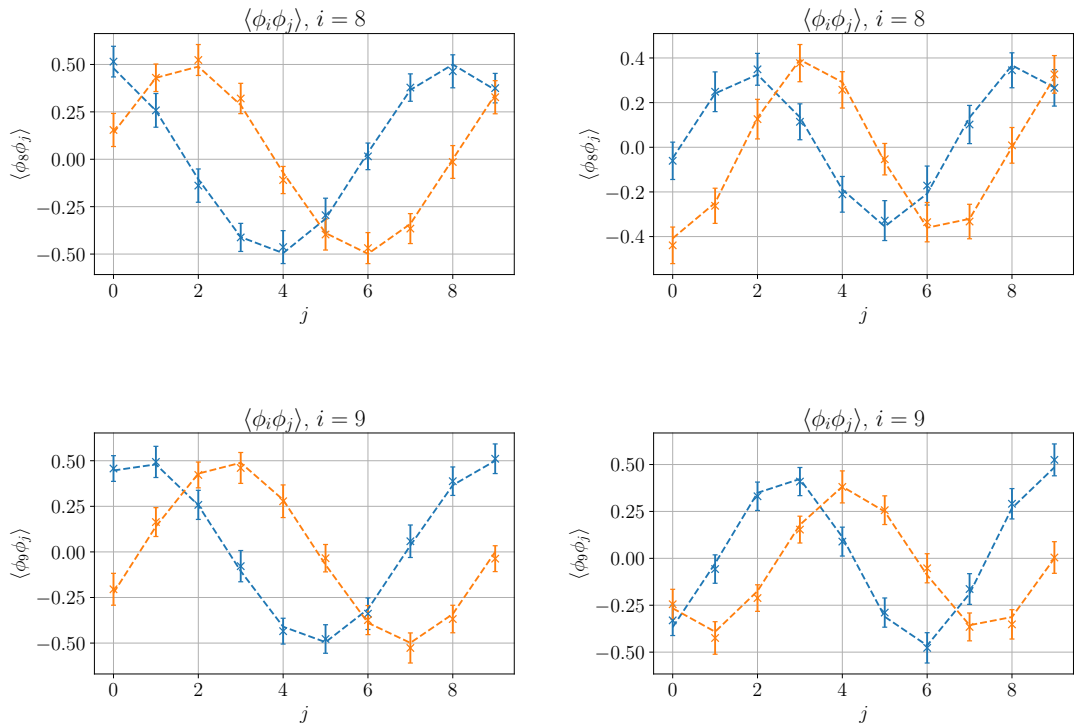


Figure 2.2: A range of time separated correlataors in the free case (left) and coupled $\lambda = 4$ case (right). The link size of $\mathrm{d}t = 0.75$ means that this covers more than three times the physical time as the case shown in Figure 2.1. As before, the dashed line represents the semi-analytic solution.

## 2.2 Equilibrium $1+1D$ Correlators

Having verified the method in the $0+1D$ case, the lattice presented in Figure 1.4 was modified to include a spatial dimension. This is done in the usual way by 'stacking' $0+1D$ contours, such that sites can interact with their neighbours on nearby spatial layers. This gives an action of the form

$$\mathcal{I} = -i\mathrm{d}x \sum_{j,n} \left[ \frac{(\phi_{j+1,n} - \phi_{j,n})^2}{2\Delta t_j} + \frac{\Delta t_j + \Delta t_{j-1}}{2} \left( -\frac{(\phi_{j,n+1} - \phi_{j,n})^2}{2\mathrm{d}x^2} - \frac{1}{2} m^2 \phi_{j,n}^2 - \frac{\lambda}{4!} \phi_{j,n}^4 \right) \right], \quad (2.8)$$

where $\mathrm{d}x$ represents the spacing between the stacked layers. Other than the change in the lattice and action, the algorithm was implemented as described in Section 2.1. Unfortunately even with the limited parameters of $N_x = 8$, where $N_x$ is the number of spacial layers, the computational effort rapidly becomes insurmountable. This is because the total number of lattice sites is now given by $N = N_x(2N_t + N_\beta) = 144$, and step 1 of the process as outlined in Section 2.1 requires the solution of $N + N^2$ complex coupled ODEs for each update of the MCMC chain. To compound this problem, calculations involving the Jacobian became increasingly prohibitive as the Jacobian itself is an $N \times N$ complex matrix. Because of this, the results presented in this work are on $0+1D$ lattices, as any attempts to produce results on a $1+1D$ lattice were cut short, giving results that look no better than random.

## 2.3 Alternatives to Jacobian Calculation

As discussed previously the calculation and manipulation of the Jacobian is computationally very difficult. It was found in our implementation that operations relating to the Jacobian, either its calculation or use, accounted for more than 75% of the computational time in the $0+1D$ case and more than 97% in the $1+1D$ case. Clearly if a method could be developed that did not require the calculation and manipulation of the Jacobian, this would significantly increase

the method's viability. To this end, two methods were trialed. However, neither had significant success.

### 2.3.1 The $J_0$ Method

The $J_0$ method relies on the assumption that variations in the manifold $\mathcal{M}$ created by the update process are small enough that the Jacobian can be approximated to be constant. If this assumption is valid, then this immediately solves the issues outlined above as the Jacobian, its inverse, and determinant can be calculated once for the entire simulation. However, this imposes a tight requirement on the maximum value of the flow parameter $\tau$, due to the fact the manifold is increasingly sensitive to changes as $\tau$ increases due to the growing mode of (1.35). In practice this results in a flow time limited to 0.1, even in the large physical time case outlined in Section 2.1. This poses a problem, as the sign problem is much less well suppressed at such a low flow time that the MCMC chain must be made much longer to compensate. This quickly erodes all speed improvements made by switching to a fixed Jacobian, and presents a new problem; the storage and processing of the much larger sets of data produced. Despite this the improvements to the rate of data generation were too impressive to ignore, and further attempts were made to increase the maximum viable flow time.

The primary method for increasing the flow time came from a hybrid of this method with the original algorithm. While the benefits of calculating the Jacobian once per simulation were not worth the drawbacks, it may not be required to calculate the Jacobian at each MCMC update either. By recalculating every $M$ updates, the preferred optimisation between speed and high flow time could be set by choosing a value for $M$. This was tested using the same set up as the large link $0 + 1D$ model discussed above with $\lambda = 24$. Selected results of the improvements for different values of $M$ are shown in Table 2.1, with more results in Appendix C.

| $M$ | Mean time per update (ms) | $\tau$ | Accurate |
|---|---|---|---|
| 1 | $0.7 \pm 0.1$ | 0.1 | Yes |
| 1 | $1.1 \pm 0.1$ | 0.2 | Yes |
| 1 | $2.6 \pm 0.3$ | 0.5 | Yes |
| 1 | $5.0 \pm 0.5$ | 1 | Yes |
| 10 | $0.02 \pm 0.01$ | 0.1 | Yes |
| 10 | $0.04 \pm 0.02$ | 0.2 | Yes |
| 10 | $0.19 \pm 0.04$ | 0.5 | Yes |
| 10 | $0.4 \pm 0.1$ | 1 | Yes |

Table 2.1: Showing the effect of skipping Jacobian updates on runtime.

The accuracy parameter was calculated by checking that the error calculated shared at least a 90% overlap with the $M = 1$ case, which corresponds to how the previous results have been calculated, with the Jacobian updated at each step. The wall clock time of these simulations scaled as expected $t_{WC} \propto 1/M$. Although superficially this appears to provide a significant improvement, the requirement to 'fine tune' this parameter $M$ defeats much of the optimisation. As $J$ is non linearly dependant on the coupling strength $\lambda$, the process of finding a suitable combination of $M$ and $\tau$ must be repeated for every action. Pragmatically, this limits the use of this technique. It is of significant note however that (1.55) depends only on the second derivative of the action. This means that the Jacobian is constant for free fields, and this property was used extensively in Section 4.1.

As this project reached its conclusion a new method for achieving this was proposed, inspired by the methods used in adaptive step size ODE solvers. Two methods of evaluating the flowed state of a scalar field exist, solving (1.35) and $\phi(\tau_{max}) = J\phi(0)$. As a result, (1.35) can be used to check the accuracy of the Jacobian, allowing for error estimation. This, in effect, allows $M$ to be dynamically set, similar to the step size in an ODE solver. As calculating (1.35) is computationally cheap compared to solving for the entire Jacobian this can be done at each update step and the results of the two methods can be compared. If they are

within a defined tolerance, the Jacobian is kept. If they are not, the Jacobian is recalculated. This method, while obviously slower than a tuned fixed $M$ model, is a considerable improvement over the standard technique in the low $\lambda$ region in which it has been tested decreasing the average time required to perform an MC update by approximately 50%. In large part this is due to the fact that as the system burns in and moves away from its initial conditions and towards a natural state, the manifold is changing more rapidly than at any other point in the simulation, and having an adaptive $J$ update rate ensures that this process is done as quickly as possible in a way that would be impossible even for the tuned approach to match. Unfortunately due to time constraints this technique has not been explored well in general, but remains an open avenue of investigation.

### 2.3.2 BiCGSTAB

Although not the only contributor to the enormous fraction of the run time that the Jacobian takes up, solving matrix equations of the form $\Delta = J\eta$ represents a significant computational cost of the algorithm. Replacing this matrix equation with an iterative solver therefore could significantly improve the run time, especially if it could be combined with other changes to reduce or eliminate a dependence on the Jacobian in other aspects of the program. The iterative solver used for this was the Biconjugate Gradient Stablized Method, or BiCGSTAB. This was implemented in the standard way:

1. Choose an estimated guess for $\Delta$, denoted $\Delta_0$. Due to the fact that $\eta$ has been drawn from a random distribution, it is difficult to estimate a reasonable $\Delta_0$ and consequently $\Delta_0$ was typically set with all elements at 0.

2. Create a new complex vector with size $N$ for $J$ being an $N \times N$ matrix, $\vec{r_0}$ = $\eta$ - $J\Delta_0$, and its unit vector $\hat{\vec{r_0}}$.

3. Define scalars $\rho_0 = \alpha = \omega_0 = \beta = 1$

4. Define vectors $\vec{v_0} = \vec{p_0} = \vec{h} = \vec{s} = \vec{t} = 0$.

5. $\rho_{i+1} = \hat{\vec{r_0}} \cdot \vec{r_i}$
6. $\beta = \rho_{i+1}\alpha/\rho_i\omega_i$
7. $\vec{p_{i+1}} = \vec{r} + \beta(\vec{p_i} - \omega_i\vec{v_i})$
8. $\vec{v_{i+1}} = J\vec{p_{i+1}}$
9. $\alpha = \rho_{i+1}/\hat{\vec{r_0}} \cdot \vec{v_{i+1}}$
10. $\vec{h} = \Delta_i + \alpha\vec{p_{i+1}}$
11. If $Jh$ is within tolerance of $\eta$, set $\Delta = \vec{h}$ and exit.
12. $\vec{s} = \vec{r_i} - \alpha\vec{v_{i+1}}$
13. $\vec{t} = J\vec{s}$
14. $\omega_{i+1} = \vec{t} \cdot \vec{s}/|t|^2$
15. $\Delta_{i+1} = \vec{h} + \omega_{i+1}\vec{s}$
16. If $J\Delta_{i+1}$ is within tolerance of $\eta$, exit.
17. $\vec{r_{i+1}} = \vec{s} - \omega_{i+1}\vec{t}$
18. Repeat from step 5 until a solution is found.

The critical part of the method is that every instance of using $J$ to transport between the manifolds can be replaced with a flow process. If the acceptance probability and calculation of the expectation values as given in 2.3 could be reformulated to not require the Jacobian, then the costly matrix operations can be completely eliminated. Furthermore the $N^2$ coupled complex ODEs do not need to be solved to calculate it either. As can be seen in Figure 2.3 using BiCGSTAB is marginally faster than solving the matrix equation using LU decomposition for the typical use case for reasonable flow time.

However, for a number of reasons this technique was not adapted into the full algorithm. Firstly the increased variance as shown in Figure 2.3 made estimations of the run time of the algorithm much less precise, causing issues for the

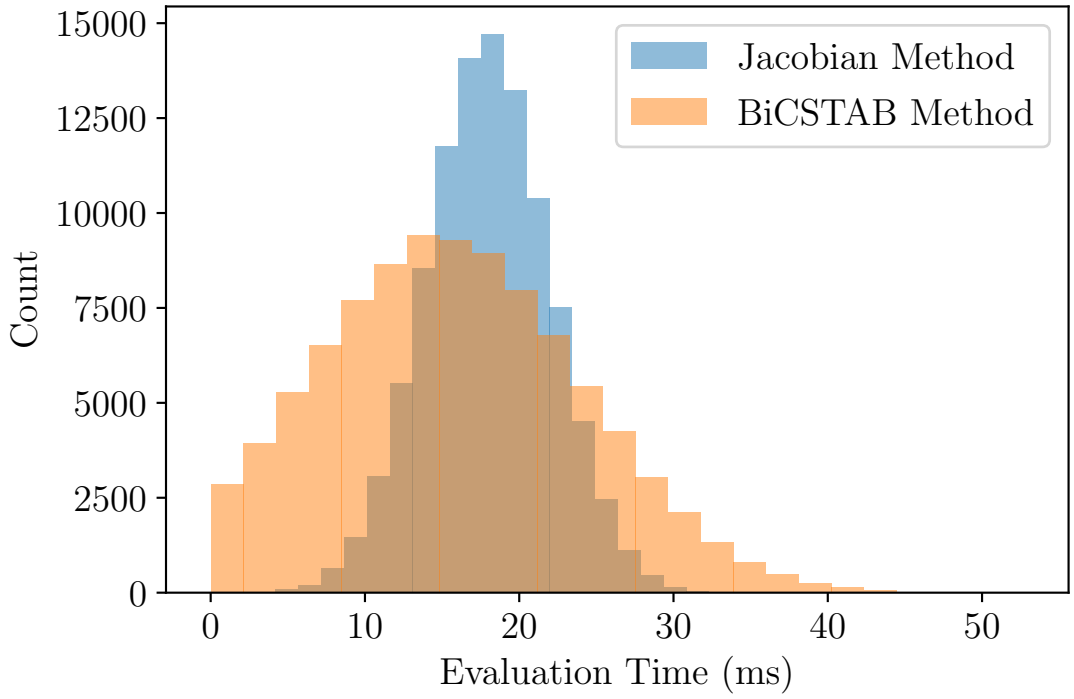


Figure 2.3: Showing the distributions in runtimes of using BiCGSTAB and the Jacobian methods over a simulation with $10^5$ steps.

allocation of resources. Secondly, BiCGSTAB becomes less effective relative to the 'brute force' method as the flow time is increased, as the manifold typically becomes more distorted often requiring that the iterative solver requires more passes to converge and solving the scalar flow equation in place of the matrix algebra becomes more computationally expensive. Thirdly this method still required the restructuring of the rest of the MCMC system to not depend on the Jacobian. Finally an optimisation that can be applied when working with the Jacobian but not BiCGSTAB is that the when evaluating the $n+1$th state, $J_n$ is already known from the previous MCMC update. This reuse of the Jacobian firmly puts it ahead of BiCGSTAB in practical terms.

# Chapter 3

# Initial Conditions Separate From the Contour

This chapter is based on the work published in [49].

## 3.1 Removing the Imaginary Time Extension

As shown in Chapter 1.1, the Schwinger-Keldysh contour typically uses an imaginary time extension to regulate its initial conditions. This method is intuitive, and highly efficient, but does not allow the contour to be used to its full potential. By removing this extension and replacing it with a fixed set of initial conditions at $t = 0, dt$, drawn from a distribution dictated by a density matrix, it is possible to simulate a much wider range of non-equilibrium phenomena. Unfortunately, in doing this much of the inherent computational efficiency is lost, and significant alterations to the contour must be made.

## 3.2 A New Density Matrix

In order to orient conventions it is convenient to start by deriving the path integral expression for calculating operator expectation values in the Heisenberg picture,

$\langle\hat{\mathcal{O}}\big(\hat{\Phi},\hat{\Pi}\big)\rangle$, with operator $\hat{\mathcal{O}}$ consisting of the scalar field operator $\hat{\Phi}$ and its canonical conjugate, $\hat{\Pi}$, at one or more times for a contour that does not have an imaginary time extension. This chapter will be following the convention in Chapter 9 of textbook [147] and, specifically, making use of following formulae[1]:

$$\begin{aligned}\int \mathcal{D}\phi|\phi;t\rangle\langle\phi;t| &= 1,\\ \int \mathcal{D}\pi|\pi;t\rangle\langle\pi;t| &= 1,\\ \langle\phi;t|\pi;t\rangle &= \left[\frac{\mathrm{d}^d x}{2\pi\hbar}\right]^{\frac{(N_s)^d}{2}} \exp\left(\frac{i}{\hbar}\int \mathrm{d}^d x\pi(x)\phi(x)\right),\end{aligned} \tag{3.1}$$

where $|\phi;t\rangle$ and $|\pi;t\rangle$ are eigenvectors of operator $\hat{\Phi}(t)$ and $\hat{\Pi}(t)$ respectively. In the formulae above, a discretized $d$-dimensional space was assumed. That is, $N_s$ sites along each spatial direction and distance $\mathrm{d}x$ between two neighbouring sites, so the volume $V = (N_s\mathrm{d}x)^d$ and, furthermore, the spatial notation can be suppressed. For instance, $\mathcal{D}\phi = \prod_x \mathrm{d}\phi(x)$. It is also convenient to switch between continuous and discrete expressions via,

$$\int \mathrm{d}^d x \quad \Leftrightarrow \quad \sum_x \mathrm{d}^d x \tag{3.2}$$

$$\frac{\delta}{\delta\phi(x)} \quad \Leftrightarrow \quad \frac{1}{\mathrm{d}x^d}\frac{\partial}{\partial\phi(x)}. \tag{3.3}$$

$\langle\hat{\mathcal{O}}\big(\hat{\Phi},\hat{\Pi}\big)\rangle$ can then be calculated by inserting complete sets of $|\phi;t_i\rangle\langle\phi;t_i|$ in succession along the temporal direction, leading to

$$\begin{aligned}\langle\hat{\mathcal{O}}\big(\hat{\Phi},\hat{\Pi}\big)\rangle = \mathrm{Tr}\left[\hat{\mathcal{O}}\big(\hat{\Phi},\hat{\Pi}\big)\hat{\rho}\big(\hat{\Phi}(t_0),\hat{\Pi}(t_0)\big)\right] =\\ \int \mathcal{D}\phi\langle\phi_0^-;t_0|\phi_1^-;t_1\rangle\langle\phi_1^-;t_1|\cdots\hat{\mathcal{O}}\cdots|\phi_1^+;t_1\rangle\langle\phi_1^+;t_1|\phi_0^+;t_0\rangle\langle\phi_0^+;t_0|\ \hat{\rho}\ |\phi_0^-;t_0\rangle\end{aligned} \tag{3.4}$$

with $\hat{\rho}\big(\hat{\Phi}(t_0),\hat{\Pi}(t_0)\big)$ the initial density matrix operator at $t_0$. Figure 3.1 gives a graphic demonstration of the insertion along the temporal direction. As discussed

[1]The third formula is the solution of,

$$-i\hbar\frac{\delta}{\delta\phi(x)}\langle\phi;t|\pi;t\rangle = \langle\phi;t|\hat{\Pi}(t,x)|\pi;t\rangle = \pi(x)\langle\phi;t|\pi;t\rangle,$$

where the first equality is derived from $[\hat{\Phi}(t,x),\ \hat{\Pi}(t,y)] = i\hbar\delta^d(x-y)$. One can further fix the coefficient through $\int\mathcal{D}\pi\langle\phi_1;t|\pi;t\rangle\langle\pi;t|\phi_2;t\rangle = \delta(\phi_1-\phi_2)$, with $\langle\phi_1;t|\phi_2;t\rangle = \delta(\phi_1-\phi_2)$.

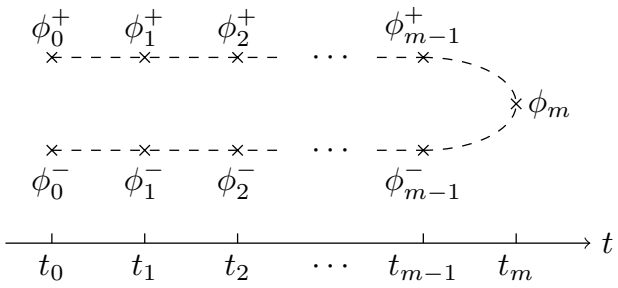


Figure 3.1: Illustration of the new $\phi$ contour. Here $\phi^+$ and $\phi^-$ are separated vertically for demonstration purposes only, as both elements of the contour lie on the real axis. The difference between two neighbouring $t$ is a constant, given by $\mathrm{d}t$, which changes sign between the two branches.

in Chapter 1.1, $m$ may be freely chosen provided it is greater than any $t$ that appears in an operator. It is also worth noting there are different ways for the operators to appear in the expression. For instance, in the case of $\hat{\mathcal{O}} = \hat{\Phi}(t_\alpha)\hat{\Phi}(t_\beta)$ and $t_\alpha > t_\beta$, if $\hat{\Phi}(t_\beta)$ appears in the upper ($\phi^+$) layer, then $\hat{\Phi}(t_\alpha)$ can appear either in the upper ($\phi^+$) or lower ($\phi^-$) layer. Later in this chapter the implications of this for the path integral will be explored.

To begin, calculate each Feynman kernel $\langle \phi_i; t_i | \phi_j; t_j \rangle$. Here it is assumed that the time difference $|t_i - t_j|$ is small, but do not specify which time is earlier. As it is required to derive the path integral with finite $\mathrm{d}t$, a symmetric expression of the kernel seems a better choice, as it will converge more quickly in the limit $\mathrm{d}t \to 0$. Thus by evolving each state to the equal time $\tilde{t} = (t_i + t_j)/2$, and then inserting the complete set of $|\pi; \tilde{t}\rangle\langle\pi; \tilde{t}|$, the expression

$$
\begin{aligned}
&\langle \phi_i; t_i | \phi_j; t_j \rangle = \langle \phi_i; \tilde{t}| \exp\left(-\frac{i}{\hbar}\frac{t_i - t_j}{2}\hat{H}\right) \exp\left(-\frac{i}{\hbar}\frac{t_i - t_j}{2}\hat{H}\right) |\phi_j; \tilde{t}\rangle \\
&= \int \mathcal{D}\pi \langle \phi_i; \tilde{t}| \exp\left(-\frac{i}{\hbar}\frac{t_i - t_j}{2}\hat{H}\right) |\pi; \tilde{t}\rangle\langle\pi; \tilde{t}| \exp\left(-\frac{i}{\hbar}\frac{t_i - t_j}{2}\hat{H}\right) |\phi_j; \tilde{t}\rangle \\
&= \left[\frac{\mathrm{d}^d x}{2\pi\hbar}\right]^{(N_s)^d} \int \mathcal{D}\pi \exp\left(-\frac{i}{\hbar}(t_i - t_j)\frac{H\big(\phi_i, \pi\big) + H\big(\phi_j, \pi\big)}{2} + \frac{i}{\hbar}\int \mathrm{d}^d x \pi(\phi_i - \phi_j)\right) \\
&= \left[\frac{\mathrm{d}^d x}{i2\pi\hbar(t_i - t_j)}\right]^{\frac{(N_s)^d}{2}} \exp\left(\frac{i}{\hbar}(t_i - t_j) L\big(\phi_i, \phi_j\big)\right)
\end{aligned}
\tag{3.5}
$$

is reached, where the operator $\hat{H}$ is the Hamiltonian which contains only up to quadratic terms of $\hat{\Pi}$. For the scalar theory, the general expression,

$$\hat{H} = \int \mathrm{d}^d x \left( \frac{\hat{\Pi}^2}{2} + \hat{C}(\hat{\Phi}) \right), \tag{3.6}$$

is assumed with $\hat{C}(\hat{\Phi})$ composed of spatial derivative terms and a field potential. Fortunately it is not required to know the exact expression of $\hat{C}(\hat{\Phi})$ at the moment, but it is important to notice $\hat{C}(\hat{\Phi})$ is local in time. The function $H(\phi_i, \pi)$ is then the result of the operator $\hat{H}$ acting on states. It is also expected that by this approach all operators, for instance $\hat{\mathcal{O}}$, may be written as functions of variables $\phi$, $\pi$. With the Hamiltonian, the Lagrangian in the equation is defined as,

$$L\big(\phi_i, \phi_j\big) = \int \mathrm{d}^d x \left( \frac{1}{2} \left[ \frac{\phi_i(x) - \phi_j(x)}{\Delta t} \right]^2 - \frac{C(\phi_i) + C(\phi_j)}{2} \right). \tag{3.7}$$

which is symmetric in $i$ and $j$. In light of (3.5), the wave function $\langle \phi; t | \mathrm{in} \rangle = \int \mathcal{D}\phi' \langle \phi; t | \phi'; t - \mathrm{d}t \rangle \langle \phi'; t - \mathrm{d}t | \mathrm{in} \rangle$ satisfies the Schrödinger functional equation [148],

$$i\hbar \frac{\partial}{\partial t} \langle \phi, t | \mathrm{in} \rangle = \int \mathrm{d}^d x \left[ -\frac{\hbar^2}{2} \frac{\delta^2}{\delta \phi(t,x)^2} + C(\phi(t,x)) \right] \langle \phi, t | \mathrm{in} \rangle. \tag{3.8}$$

Thus, Feynman's kernel is the propagator for small time intervals. It is important to emphasize that the derivations in (3.5) are valid for both $t_i > t_j$ and $t_i < t_j$. In fact, from $\phi^+_{m-1}$ to $\phi_m$, the time difference is $\mathrm{d}t$, but from $\phi_m$ to $\phi^-_{m-1}$, it is $-\mathrm{d}t$. Continuing to work with (3.4), slightly rewritten as

$$\begin{aligned} \langle \hat{\mathcal{O}}\big(\hat{\Phi}, \hat{\Pi}\big) \rangle &= \mathrm{Tr} \left[ \hat{\mathcal{O}}\big(\hat{\Phi}, \hat{\Pi}\big) \hat{\rho}\big(\hat{\Phi}(t_0), \hat{\Pi}(t_0)\big) \right] \\ &= \mathcal{N} \int \mathcal{D}\phi \exp\left( \frac{i}{\hbar} \int_{\mathcal{C}} \mathrm{d}t L \right) \mathcal{O}\big(\phi, \pi\big) \langle \phi_0; t_0 | \hat{\rho}\Big(\hat{\Phi}(t_0), \hat{\Pi}(t_0)\Big) | \phi_n; t_0 \rangle \end{aligned} \tag{3.9}$$

where $\mathcal{N}$ is a collection of numerical constants that appear in kernel (3.5), and the integration contour $\mathcal{C}$ is understood as the contour shown in Figure 3.1. In the discrete theory, the integral over $\mathcal{C}$ in the exponent is really an abbreviation

of,

$$\int_{\mathcal{C}} \mathrm{d}tL = \mathrm{d}t \sum_{i=1}^{m} \left( L\big(\phi_i^+, \phi_{i-1}^+\big) - L\big(\phi_{i-1}^-, \phi_i^-\big) \right) \tag{3.10}$$

where, to write the expression elegantly, denote $\phi_m = \phi_m^+ = \phi_m^-$. On the other hand, since the numerical constant $\mathcal{N}$ does not depend on the operator $\hat{\mathcal{O}}$, it can be fixed by taking the case $\hat{\mathcal{O}} = 1$,

$$1 = \mathrm{Tr}\left[\hat{\rho}\big(\hat{\Phi}(t_0), \hat{\Pi}(t_0)\big)\right] = \mathcal{N} \int \mathcal{D}\phi \exp\left(\frac{i}{\hbar}\int_{\mathcal{C}} \mathrm{d}tL\right) \langle \phi_0; t_0 | \hat{\rho}\Big(\hat{\Phi}(t_0), \hat{\Pi}(t_0)\Big) | \phi_n; t_0 \rangle, \tag{3.11}$$

noting that the trace of the density matrix is one. It can be noted that due to (3.10), $\mathcal{N}$ is not fixed to be 1 as the upper and lower branches may be different valued. Therefore, it is possible to write the expectation value of the operator as a ratio,

$$\langle \hat{\mathcal{O}}\big(\hat{\Phi}, \hat{\Pi}\big) \rangle = \frac{\int \mathcal{D}\phi \exp\left(\frac{i}{\hbar}\int_{\mathcal{C}} \mathrm{d}tL\right) \mathcal{O}\big(\phi, \pi\big) \langle \phi_0; t_0 | \hat{\rho}\Big(\hat{\Phi}(t_0), \hat{\Pi}(t_0)\Big) | \phi_n; t_0 \rangle}{\int \mathcal{D}\phi \exp\left(\frac{i}{\hbar}\int_{\mathcal{C}} \mathrm{d}tL\right) \langle \phi_0; t_0 | \hat{\rho}\Big(\hat{\Phi}(t_0), \hat{\Pi}(t_0)\Big) | \phi_n; t_0 \rangle}, \tag{3.12}$$

and so any overall constants are cancelled. In this chapter (3.12) will be computed by showing that it admits a Monte Carlo evaluation, where one generates samples according to the distribution in the denominator,

$$\int \mathcal{D}\phi \exp\left(\frac{i}{\hbar}\int_{\mathcal{C}} \mathrm{d}tL\right) \langle \phi_0; t_0 | \hat{\rho}\Big[\Phi(t_0), \Pi(t_0)\Big] | \phi_n; t_0 \rangle. \tag{3.13}$$

### 3.2.1 Critical Points

Using this information, it is now possible to calculate the critical points in (3.13). Here it is helpful to introduce $\mathcal{I} = -i\int_{\mathcal{C}} \mathrm{d}tL/\hbar + \cdots$, with ellipsis denoting extra terms coming from the initial density matrix, which are functions of $\phi_0$ only, i.e. $\phi_0^+$ and $\phi_0^-$. To study the critical points it is convenient to use another basis, $\phi^{cl}$

and $\phi^q$, defined through [149, 150, 151, 3, 152][2],

$$\phi_i^+(x) = \phi_i^{cl}(x) + \frac{\phi_i^q}{2}(x), \quad \phi_i^-(x) = \phi_i^{cl}(x) - \frac{\phi_i^q}{2}(x). \tag{3.14}$$

(Even though change of basis to $\phi_m(x)$ does not apply, as there is only one field, it will be useful to introduce $\phi_m^{cl}(x) = \phi_m(x)$ and $\phi_m^q(x) = 0$. However $\phi_m^q(x)$ is not treated as a variable.) With these, the integration becomes

$$\int_{\mathcal{C}} \mathrm{d}tL = \mathrm{d}t \sum_{i=1}^{m} \left[ \int \mathrm{d}^d x \left( \frac{\left(\phi_i^{cl}(x) - \phi_{i-1}^{cl}(x)\right)\left(\phi_i^q(x) - \phi_{i-1}^q(x)\right)}{(dt)^2} \right) - \frac{E_i + E_{i-1}}{2} \right] \tag{3.15}$$

where

$$E_i = \int \mathrm{d}^d x \left[ C\left(\phi_i^{cl}(x) + \frac{\phi_i^q(x)}{2}\right) - C\left(\phi_i^{cl}(x) - \frac{\phi_i^q(x)}{2}\right) \right] \tag{3.16}$$

There are two general features that can already be derived even without knowing the exact form of the Lagrangian.

1. $E_m = 0$. The only term in the exponent containing $\phi_m(x)$ is the product of $\phi_m(x)$ and $\phi_{m-1}^q(x)$. Actually, in (3.13), one can integrate $\phi_m(x)$ out, and get a delta function, as follows,

$$\begin{aligned} \int \mathcal{D}\phi_m e^{-\frac{i}{\hbar \mathrm{d}t}\int \mathrm{d}^d x \phi_m(x)\phi_{m-1}^q(x)} &= \prod_x (2\pi)\delta\left(-\frac{\mathrm{d}x^d}{\hbar \mathrm{d}t}\phi_{m-1}^q(x)\right) \\ &= \left(\frac{2\pi\hbar \mathrm{d}t}{\mathrm{d}x^d}\right)^{(N_s)^d} \prod_x \delta\left(\phi_{m-1}^q(x)\right). \end{aligned} \tag{3.17}$$

If one further integrates out $\phi_{m-1}^q(x)$, (3.13) would become the same form as the original integral, but with the turning point $\phi_m$ replaced by $\phi_{m-1}^{cl}$, and with an extra overall constant. It is important to emphasise the fact that the integration over $(\phi_m^{cl},\ \phi_{m-1}^q)$ together is a constant and it will not alter the remaining path integral, except through the overall constant. One can perform the integration

[2]In the literature there exists alternative ways to transform $\phi^+$ and $\phi^-$, with Keldysh's original convention [150, 152] corresponding to $\phi^{\pm} = \left(\phi^{cl} \pm \phi^q\right)/\sqrt{2}$. Here the approach of [151, 3] is followed, but adopting the names $\phi^{cl}$ and $\phi^q$ from [152].

on any $(\phi_i^{cl},\ \phi_{i-1}^q)$ as long as it is the last pair along the real-time direction. By continuing this process down to $\phi_0$,

$$\int \mathcal{D}\phi \exp\left(\frac{i}{\hbar}\int_{\mathcal{C}} \mathrm{d}tL\right) \langle \phi_0; t_0|\hat{\rho}|\phi_n; t_0\rangle = \cdots = \frac{1}{\mathcal{N}}\int \mathcal{D}\phi \langle \phi_0; t_0|\hat{\rho}|\phi_0; t_0\rangle = \frac{1}{\mathcal{N}}, \tag{3.18}$$

is reached. This is just (3.11), written in reverse order, and also provides an alternative way to compute the constant $\mathcal{N}$. Of course, to avoid keeping numerical constants, one can execute such contraction simultaneously in both the numerator and denominator of (3.12). However, the contraction in the numerator is no longer valid once $\hat{\mathcal{O}}(t)$ is reached. For instance, with a $\phi_m$ inserted one can not execute the integral $\int \mathcal{D}\phi\phi_m e^{-\frac{i}{\hbar dt}\int d^dx \phi_m(x)\phi^q_{m-1}(x)}$, as in (3.17). Generally, if $t_{max}$ is the maximum time that the operator $\hat{\mathcal{O}}$ depends on, then as long as $t_m \geqslant t_{max}$, the path beyond $t_{max}$ is contractible. This corresponds to the freedom that one can have in choosing the closed time path when restricted to the real-time line.

In principle the traditional way of writing the contour with two values at point $m$ could be kept. However, due to the contraction, there is no need to keep two points at the $m$th point. This simplifies the mathematical and computational structure.

2. All terms in $E_i$ must contain odd powers of $\phi_i^q(x)$, as even powers of $\phi_i^q(x)$ cancel out. This can be checked by expanding (3.15), (3.16) as a Taylor series in $\phi_i^q$, or more explicitly for an arbitrary function $f$,

$$\begin{aligned}
\phi_i^+ = \phi_i^{cl} + \phi_i^q/2 \implies \frac{\mathrm{d}f(\phi_i^+)}{\mathrm{d}\phi_i^q} &= \frac{1}{2}\frac{\mathrm{d}f(\phi_i^+)}{\mathrm{d}\phi_i^+}, \\
\phi_i^- = \phi_i^{cl} - \phi_i^q/2 \implies \frac{\mathrm{d}f(\phi_i^-)}{\mathrm{d}\phi_i^q} &= -\frac{1}{2}\frac{\mathrm{d}f(\phi_i^-)}{\mathrm{d}\phi_i^-}.
\end{aligned}$$

This difference in sign in the derivative ensures that even powers of $\phi_i^q$ in the expansion of $C(\phi_i^{\pm})$ will match, while odd power terms will differ by a sign. Using that, and the definition in (3.16), even powers will cancel, leaving only odd powers. In fact, the quantum field theory can be computed through the

perturbation theory of $\phi^q$ [3]. The leading order theory has a term linear in $\phi^q$ appearing in the exponent, and if the integration of $\phi^q$ is carried out explicitly, the leading order theory is the classical theory. A simple example is $\lambda\phi^4$ theory,

$$\begin{aligned}
&\int \mathcal{D}\phi \exp\left(\frac{i}{\hbar}\int_{\mathcal{C}} \mathrm{d}t \int \mathrm{d}^d x \left[\frac{1}{2}\left(\dot{\phi}\right)^2 - \frac{1}{2}\left(\nabla\phi\right)^2 - \frac{1}{2}m^2\phi^2 - \frac{\lambda}{4!}\phi^4\right]\right) \\
&= \int \mathcal{D}\phi \\
&\qquad \exp\left(\frac{i}{\hbar}\int \mathrm{d}t \int \mathrm{d}^d x \left[\dot{\phi}^{cl}\dot{\phi}^q - \nabla\phi^{cl}\nabla\phi^q - m^2\phi^{cl}\phi^q - \frac{\lambda}{4!}\left[4\phi^q(\phi^{cl})^3 + (\phi^q)^3\phi^{cl}\right]\right]\right) \\
&= \int \mathcal{D}\phi \\
&\qquad e^{\frac{i}{\hbar}\int \mathrm{d}t \int \mathrm{d}^d x\left[\dot{\phi}^{cl}\dot{\phi}^q - \nabla\phi^{cl}\nabla\phi^q - m^2\phi^{cl}\phi^q - \frac{\lambda}{3!}\phi^q(\phi^{cl})^3\right]} \exp\left(-\frac{i\lambda}{4!\hbar}\int \mathrm{d}t \int \mathrm{d}^d x (\phi^q)^3\phi^{cl}\right) \\
&= \int \mathcal{D}\phi \\
&\qquad e^{\frac{i}{\hbar}\int \mathrm{d}t \int \mathrm{d}^d x\left[\dot{\phi}^{cl}\dot{\phi}^q - \nabla\phi^{cl}\nabla\phi^q - m^2\phi^{cl}\phi^q - \frac{\lambda}{3!}\phi^q(\phi^{cl})^3\right]} \left(1 - \frac{i\lambda}{4!\hbar}\int \mathrm{d}t \int \mathrm{d}^d x (\phi^q)^3\phi^{cl} + \cdots\right)
\end{aligned} \tag{3.19}$$

where the initial density matrix has been omitted for the time being. A note on the notation, as $\phi$ is evaluated along $\mathcal{C}$, and as in Figure 3.1 $\mathrm{d}t$ will be negative along the $\phi^-$ branch. As a result, $\int_{\mathcal{C}} \mathcal{D}\phi\ \phi^n = \int \mathcal{D}\phi\ [\phi(\phi^+)^n - \phi(\phi^-)^n]$ in the first line of (3.19). By keeping the leading term in the expansion of the exponential and integrating out $\phi^q$, the delta function, $\delta\left(-\frac{\partial^2\phi^{cl}}{\partial t^2} + \nabla^2\phi^{cl} - m^2\phi_i^{cl} - \frac{\lambda}{3!}\left(\phi_i^{cl}\right)^3\right)$, can be found, which means in the leading order theory, $\phi^{cl}$ satisfies the equation of motion of the classical field. When $\phi_i^q(x) = 0$ at any $x$, then $\partial E_i/\partial\phi_i^{cl}(x)$ must also vanish, since it consists of odd terms of $\phi_i^q$, and can therefore have no constant part. To proceed with the goal of finding the critical points it is useful to remember that the critical points are determined by $\partial\mathcal{I}/\partial\phi|_{crit} = 0$ for all $\phi$. The derivation is straightforward for $0 < i < m$ using $\mathcal{I} = -i/\hbar\int_{\mathcal{C}} \mathrm{d}tL$ and $\int_{\mathcal{C}} \mathrm{d}tL$ defined as in (3.15),

$$\frac{\partial\mathcal{I}}{\partial\phi_i^q(x)} = -\frac{i(\mathrm{d}t)(\mathrm{d}x^d)}{\hbar}\left[\frac{2\phi_i^{cl}(x) - \phi_{i-1}^{cl}(x) - \phi_{i+1}^{cl}(x)}{(\mathrm{d}t)^2} - \frac{\partial E_i}{\partial\phi_i^q(x)}\right] \tag{3.20}$$

$$\frac{\partial\mathcal{I}}{\partial\phi_i^{cl}(x)} = -\frac{i(\mathrm{d}t)(\mathrm{d}x^d)}{\hbar}\left[\frac{2\phi_i^{q}(x) - \phi_{i-1}^{q}(x) - \phi_{i+1}^{q}(x)}{(\mathrm{d}t)^2} - \frac{\partial E_i}{\partial\phi_i^{cl}(x)}\right] \tag{3.21}$$

and for $i = m$,

$$\frac{\partial \mathcal{I}}{\partial \phi_m(x)} = \frac{i(\mathrm{d}x^d)}{\hbar \mathrm{d}t}\phi^q_{m-1}(x) \tag{3.22}$$

At critical points, (3.20) - (3.22) all vanish, by definition. It can now be proven via induction, that critical points require all $\phi^q_i(x) = 0$ with $0 < i < m$. This is true for $i = m - 1$, as the vanishing (3.22) alone indicates $\phi^q_{m-1}(x) = 0$ at any $x$. Given this, if $\phi^q_{i+1}(x) = 0$ along with $\phi^q_i(x) = 0$ at any $x$, then as this implies $\partial E_i/\partial \phi^{cl}_i(x) = 0$. This is because (3.16) relies on the difference between $\phi^+_i$ and $\phi^-_i$ and once $\phi^q_i$ is fixed to zero for all $x$, $\phi^+_i = \phi^-_i$ and the integrand vanishes. However this does not apply to $\partial E_i/\partial \phi^q_i$, as by varying $\phi^q_i$, the integrand is no longer zero. It can then be seen that the vanishing of (3.21) leads to $\phi^q_{i-1}(x) = 0$. This induction can be applied all the way down to $\partial \mathcal{I}/\partial \phi^{cl}_2 = 0$, such that all $\phi^q_i(x) = 0$ with $0 < i < m$.

Now that $\phi^q_i(x) = 0$ has been fixed at the critical point, the vanishing of (3.20) can be used to lead us to the classical equation of motion, i.e. $\partial \mathcal{I}/\partial \phi^q_i(x) = 0$,

$$\frac{2\phi^{cl}_i(x) - \phi^{cl}_{i-1}(x) - \phi^{cl}_{i+1}(x)}{(\mathrm{d}t)^2} - \frac{\partial E_i}{\partial \phi^q_i(x)}\Big|_{\phi^q_i = 0} = 0. \tag{3.23}$$

Notice that the second term on the left-hand side contains only $\phi^{cl}_i$. Therefore, (3.23) determines $\phi^{cl}_{i+1}(x)$ uniquely once $\phi^{cl}_i(x)$ and $\phi^{cl}_{i-1}(x)$ are known. In other words once $\phi^{cl}_0(x)$ and $\phi^{cl}_1(x)$ are known, it is simple to uniquely solve all subsequent $\phi^{cl}$. In this sense the critical points are completely determined by $\phi^{cl}_0(x)$ and $\phi^{cl}_1(x)$. The results of this is essential to understanding the rest of the approach. For a general field theory, there are many critical points. However for a specific initialisation, parameterised by $\phi^{cl}_0$, $\phi^{cl}_1$, there is only one critical point for systems set up in this way. In exchange however, the entire $\phi^{cl}_0$, $\phi^{cl}_1$ parameter space must be mapped, essentially trading a many critical points system for many single critical point systems.

What has been shown here therefore, is that there is a single critical point for each given $\phi^{cl}_0(x)$ and $\phi^{cl}_1(x)$, and so by picking $\phi^{cl}_0(x)$ and $\phi^{cl}_1(x)$ there will be a single thimble associated to that single critical point. Now a scheme is needed to

select $\phi_0^{cl}(x)$ and $\phi_1^{cl}(x)$, and for this an explicit expression of the initial density matrix is required.

## 3.3 Initial Density Matrix

There are several situations where one can have an explicit expression for the density matrix, one of which is thermal equilibrium, for which the density matrix may be written as a path integral of imaginary time. Another situation is free theory, where only Gaussian integrals are involved.

### 3.3.1 Thermal Density Matrix

The density matrix operator for thermal equilibrium is $\hat{\rho} = e^{-\beta\hat{H}}/Z$, where $1/\beta = k_B T$, with $k_B$ being Boltzmann's constant and $T$ the temperature. Since the partition function $Z = \mathrm{Tr}\left[e^{-\beta\hat{H}}\right]$ is an overall constant, the focus can be on calculating the expectation value of $e^{-\beta\hat{H}}$. In this case, the insertion of complete sets leads to,

$$\begin{aligned}\langle\phi_0^+;t_0|e^{-\beta\hat{H}}|\phi_0^-;t_0\rangle &= \langle\phi_0^+;t_0|e^{-\Delta\beta\hat{H}}\cdots e^{-\Delta\beta\hat{H}}|\phi_0^-;t_0\rangle \\ &= \int\prod_{k=I}^{N-1}\mathcal{D}\phi_k\langle\phi_0^+;t_0|e^{-\Delta\beta\hat{H}}|\phi_I;t_0\rangle\langle\phi_I;t_0|e^{-\Delta\beta\hat{H}}|\phi_{II};t_0\rangle \\ &\qquad \langle\phi_{II};t_0|\cdots\langle\phi_{N-1};t_0|e^{-\Delta\beta\hat{H}}|\phi_0^-;t_0\rangle \quad (3.24)\end{aligned}$$

with $\Delta\beta = \beta/N$. As the label suggests, it would be convenient to also denote $\phi_0^+$ as $\phi_0$ and $\phi_0^-$ as $\phi_N$. The computation of each single kernel is similar as in (3.5),

and it can also be computed in a symmetric way,

$$\begin{aligned}
&\langle\phi_k;t_0|e^{-\Delta\beta\hat{H}}|\phi_{k+1};t_0\rangle = \int\mathcal{D}\pi\langle\phi_k;t_0|e^{-\frac{d\beta}{2}\hat{H}}|\pi_k;t_0\rangle\langle\pi_k;t_0|e^{-\frac{d\beta}{2}\hat{H}}|\phi_{k+1};t_0\rangle \\
&= \left[\frac{d^dx}{2\pi\hbar}\right]^{(N_s)^d}\int\mathcal{D}\pi\exp\left(-\Delta\beta\frac{H\big[\phi_k,\pi\big]+H\big[\phi_{k+1},\pi\big]}{2}+\frac{i}{\hbar}\int\mathrm{d}^dx\pi(\phi_k-\phi_{k+1})\right) \\
&= \left[\frac{\mathrm{d}^dx}{2\pi\hbar^2\Delta\beta}\right]^{\frac{(N_s)^d}{2}}\exp\left(\Delta\beta L\big[\phi_k,\phi_{k+1}\big]\right), \qquad (3.25)
\end{aligned}$$

where Lagrangian is defined similarly to the real-time one, but with $\mathrm{d}t$ substituted by $-i\hbar\Delta\beta$,

$$L\big[\phi_k,\phi_{k+1}\big] = \int\mathrm{d}^dx\left[\frac{1}{2}\left(\frac{\phi_k(x)-\phi_{k+1}(x)}{-i\hbar\Delta\beta}\right)^2-\frac{C(\phi_k)+C(\phi_{k+1})}{2}\right]. \qquad (3.26)$$

It is then straightforward to compose the expectation value as a series of integrals, along a trajectory from $\phi_N$ (so $\phi_0^-$) to $\phi_0$ (so $\phi_0^+$), through negative imaginary time,

$$\begin{aligned}
&\langle\phi_0;t_0|e^{-\beta\hat{H}}|\phi_N;t_0\rangle = \\
&\left[\frac{\mathrm{d}^dx}{2\pi\hbar^2\Delta\beta}\right]^{\frac{N(N_s)^d}{2}}\int\prod_{k=I}^{N-1}\mathcal{D}\phi_k\exp\left(\Delta\beta L_0\big[\phi_0,\phi_I\big]\right)\exp\left(\Delta\beta L_0\big[\phi_k,\phi_{k+1}\big]\right). \qquad (3.27)
\end{aligned}$$

In combination with the integral along the real-time as in (3.13), the whole path integral is defined on a closed contour in the complex time plane, which is periodic along the imaginary time, with a period $\hbar\beta$. Since there exist different ways to insert complete sets, there is great freedom in choosing the contour in the complex time plane. For a graphic illustration, see Figure 3.2. So far, this work has only considered the density matrix of a general scalar field, but for free fields it is possible to carry out the integrals in (3.27). It is more convenient to do this in momentum space, where one can treat quantum field theory as a collection of harmonic oscillators interacting with each other. With free fields this generates independent harmonic oscillators, and the integrals for these situations are well known. To be precise, the integration variable in the oscillator case is real, but $\phi(p)$ is generally complex, since $\phi(x)$ is real. Thus it would be more

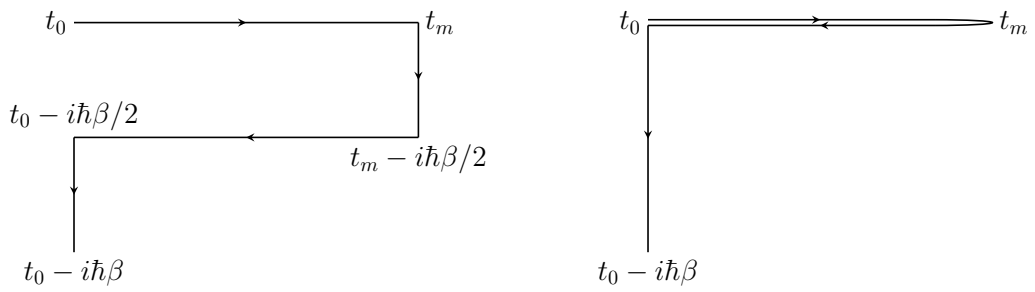


Figure 3.2: For thermal equilibrium, the complex time path is periodic along the imaginary time direction, with the period $\hbar\beta$, and there exists great freedom in choosing the contour in the complex time plane. (L) The Schwinger-Keldysh closed time contour used in [1, 2]; (R) The Schwinger-Keldysh closed time contour used in [3]. In Section 3.3 the right-hand side path was utilised to derive analytic expressions, where both trajectories of $t_0 \to t_m$ and $t_m \to t_0$ are located on the real-time line, and the vertical offset between them exists only for demonstration purposes.

appropriate to use its real and imaginary components as integration variables, in particular $\sqrt{2}\phi_{\rm re}(p)$ and $\sqrt{2}\phi_{\rm im}(p)$, which can be regarded as the result of a unitary transformation of $(\phi(p),\ \phi(-p))$. On the other hand, one can also arrive at the same variables, by performing a real-to-real Fourier transform in the first place. Later on, the use of $p, re, im$ will mean that it is these real integration variables that have been used. It is easy to switch between $\phi(p),\ \phi(-p)$ and $\sqrt{2}\phi_{\rm re}(p),\ \sqrt{2}\phi_{\rm im}(p)$. The free Lagrangian in momentum space then takes the form,

$$L_0\big[\phi_n, \phi_{n+1}\big] = \frac{1}{V}\sum_{p,re,im}\left[\frac{1}{2}\frac{\left(\phi_n(p) - \phi_{n+1}(p)\right)^2}{\left(-i\hbar\Delta\beta\right)^2}\right. \tag{3.28}$$

$$\left. - \frac{1}{2}\frac{\phi_n(-p)\omega_p^2\phi_n(p) + \phi_{n+1}(-p)\omega_p^2\phi_{n+1}(p)}{2}\right], \tag{3.29}$$

where $\omega_p = \sqrt{p^2 + m^2}$ in the continuum, but as discussed in Chapter 1.1 the lattice momentum needs to be replaced by $p \to p_{latt} = -(i/\Delta x)(e^{ik\Delta x} - 1)$, and $V$ is the spatial volume. The symbols $\int \frac{d^d p}{(2\pi)^d}$ and $\frac{1}{V}\sum_p$ are treated as being interchangeable. Switching (3.27) into momentum space, the integrals can now

be performed,

$$\begin{aligned}
&\langle\phi_0;t_0|e^{-\beta\hat{H}}|\phi_N;t_0\rangle \\
&= \left[\frac{1}{2\pi V\hbar^2\Delta\beta}\right]^{\frac{N(N_s)^d}{2}} \prod_{p,re,im}\int\prod_{k=I}^{N-1}\mathcal{D}\phi_k \exp\left(\Delta\beta L_0\big[\phi_0,\phi_I\big]\right)\exp\left(\Delta\beta L_0\big[\phi_k,\phi_{k+1}\big]\right) \\
&= \prod_{p,re,im}\left[\left(\frac{\omega_p}{2\pi V\hbar\sinh(\hbar\omega_p\beta)}\right)^{1/2}\right. \\
&\qquad\left.\exp\left(-\frac{\omega_p\left[\cosh(\hbar\omega_p\beta)\left(\phi_N^2(p)+\phi_0^2(p)\right)-2\phi_N(p)\phi_0(p)\right]}{2\hbar V\sinh(\hbar\omega_p\beta)}\right)\right]
\end{aligned} \tag{3.30}$$

where the overall constant on the second line is changed due to the Fourier transform, and to reach the last line the limit $\Delta\beta \to 0$ is taken. The partition function can now be calculated as,

$$\begin{aligned}
Z &= \prod_{p,re,im}\int \mathrm{d}\phi(p)\langle\phi;t_0|e^{-\beta\hat{H}}|\phi;t_0\rangle \\
&= \prod_p \frac{1}{2\sinh(\hbar\omega_p\beta/2)} \\
&= \prod_p\left(\sum_{n_p=0}^{\infty} e^{-\hbar\omega_p\beta(n_p+1/2)}\right) \\
&= \prod_p \frac{e^{-\hbar\omega_p\beta/2}}{1-e^{-\hbar\omega_p\beta}},
\end{aligned} \tag{3.31}$$

where in the final line the observation that the sum can be treated as a geometric series is used to complete the sum. The free energy is defined

$$\begin{aligned}
F &= -T\ln(Z) \\
&= -T\sum_p \ln\left(\frac{e^{-\hbar\omega_p\beta/2}}{1-e^{-\hbar\omega_p\beta}}\right).
\end{aligned} \tag{3.32}$$

This depends on a sum over momentum sates, which depends on the setup of the lattice.

### 3.3.2 Initial density matrix for vacuum and $n$-particle states

Alternatively, everything can also be derived from the $n$-particle eigenstates. The free theory is equivalent to a sum of independent harmonic oscillators with different $\omega_p$. Therefore, it is possible to derive $n$-particle eigenstates for the free field theory as one does in the harmonic oscillator.

In momentum space, the vacuum wave function is[3]

$$\begin{aligned}\langle\phi|\text{vac}\rangle &= \prod_{p,re,im}\left(\frac{\omega_p}{V\hbar\pi}\right)^{1/4}\exp\left(-\frac{\omega_p\phi^2(p)}{2V\hbar}\right) \\ &= \left(\prod_p\left(\frac{\omega_p}{V\hbar\pi}\right)^{1/4}\right)\exp\left(-\frac{1}{\hbar}\int\frac{\mathrm{d}^dp}{(2\pi)^d}\frac{\omega_p\phi^2(p)}{2}\right).\end{aligned} \tag{3.33}$$

With it, the density matrix of the vacuum state can be written as,

$$\langle\phi_0;t_0|\text{vac}\rangle\langle\text{vac}|\phi_n;t_0\rangle = \prod_{p,re,im}\left(\frac{\omega_p}{V\hbar\pi}\right)^{1/2}\exp\left(-\frac{\omega_p}{V\hbar}\frac{\phi_0(p)\phi_0(p)+\phi_n(p)\phi_n(p)}{2}\right). \tag{3.34}$$

The wave function of the $n$-particle state is

$$\langle\phi|n\rangle = \prod_{p,re,im}\left(\frac{\omega_p}{V\hbar\pi}\right)^{1/4}\frac{1}{\sqrt{2^{n_p}n_p!}}h_{n_p}\left(\sqrt{\frac{\omega_p}{V\hbar}}\phi(p)\right)\exp\left(-\frac{1}{2}\left(\sqrt{\frac{\omega_p}{V\hbar}}\phi(p)\right)^2\right), \tag{3.35}$$

where the Hermite polynomial $h_n(z)$ is defined as:

$$h_n(z) = e^{z^2/2}\left(z-\frac{\mathrm{d}}{\mathrm{d}z}\right)^n e^{-z^2/2}. \tag{3.36}$$

This allows for the computation of the density matrix of any pure state or mixed state, as long as it can be expanded as $n$-particle states. For instance, it is straightforward to calculate the density matrix for the thermal states, up to the

[3]The wave function here is understood as a stationary wave function. With the time-dependent phase term $e^{-i\omega_p t/2}$, the wave function is the ground-state solution of Schrödinger functional equation (3.8), and the energy of the ground state is $\hbar\omega_p/2$.

partition function $Z$,

$$\begin{aligned}
&\langle\phi_0;t_0|e^{-\beta\hat{H}}|\phi_N;t_0\rangle \qquad (3.37)\\
&=\prod_{p,re,im}\left(\frac{\omega_p}{V\hbar\pi}\right)^{1/2}\sum_{n_p=0}^{+\infty}\frac{1}{\sqrt{2^{n_p}n_p!}}h_{n_p}\left(\sqrt{\frac{\omega_p}{V\hbar}}\phi_0(p)\right)\exp\left(-\frac{1}{2}\left(\sqrt{\frac{\omega_p}{V\hbar}}\phi_0(p)\right)^2\right)\\
&\quad\frac{1}{\sqrt{2^{n_p}n_p!}}h_{n_p}\left(\sqrt{\frac{\omega_p}{V\hbar}}\phi_N(p)\right)\exp\left(-\frac{1}{2}\left(\sqrt{\frac{\omega_p}{V\hbar}}\phi_N(p)\right)^2\right)e^{-\hbar\omega_p\beta\left(n_p+\frac{1}{2}\right)}\\
&=\prod_{p,re,im}\left(\frac{\omega_p}{2\pi V\hbar\sinh(\hbar\omega_p\beta)}\right)^{1/2}\exp\left(-\frac{\omega_p}{V\hbar}\frac{\cosh(\hbar\omega_p\beta)(\phi_0^2(p)+\phi_N^2(p))-2\phi_0(p)\phi_N(p)}{2\sinh(\hbar\omega_p\beta)}\right),
\end{aligned}$$

where to get the final expression Mehler's formula has been used. Mehler's formula reads

$$\sum_{n=0}^{\infty}\frac{(\rho/2)^n}{n!}h_n(x)h_n(y)=\frac{1}{\sqrt{1-\rho^2}}\exp\left(-\frac{\rho^2(x^2+y^2)-2\rho xy}{(1-\rho^2)}\right), \qquad (3.38)$$

here used with

$$\begin{aligned}
\rho&=e^{-i\hbar\omega_p\beta}\\
x&=\sqrt{\frac{\omega_p}{V\hbar}}\phi_0(p) \qquad (3.39)\\
y&=\sqrt{\frac{\omega_p}{V\hbar}}\phi_N(p).
\end{aligned}$$

### 3.3.3 Path integral with a free initial density matrix

Given a free initial density matrix, the full path integral has the general form,

$$\begin{aligned}
Z=\int\mathcal{D}\phi\exp\Bigg(&-\frac{1}{\hbar}\int\frac{\mathrm{d}^dp}{(2\pi)^d}\frac{\omega_p\left(\cosh(\hbar\omega_p\beta)\left[(\phi_0^+)^2+(\phi_0^-)^2\right]-2\phi_0^+\phi_0^-\right)}{2\sinh(\hbar\omega_p\beta)}\\
&+\frac{i}{\hbar}\int_{\mathcal{C}}\mathrm{d}tL\Bigg), \qquad (3.40)
\end{aligned}$$

or, in the $\phi^{cl}$ and $\phi^q$ basis,

$$Z = \int \mathcal{D}\phi \exp\left(-\frac{1}{\hbar}\int \frac{\mathrm{d}^d p}{(2\pi)^d}\omega_p \left[\frac{(\phi_0^{cl})^2}{2n_p+1} + \frac{(\phi_0^q)^2}{4}(2n_p+1)\right] + \frac{i}{\hbar}\int_{\mathcal{C}} \mathrm{d}t L\right), \quad (3.41)$$

with the occupation number given by

$$n_p = \frac{1}{e^{\hbar\omega_p\beta}-1}. \quad (3.42)$$

The initial density matrix in (3.41) implies that the field $\phi_0^{cl}$ is drawn from a normal distribution with the variance proportional to $2n_p+1$, while $\phi_0^q$ comes from a normal distribution with variance proportional to $1/(2n_p+1)$. A better understanding of this observation can be gained by integrating out $\phi_0^q$, noting that $\phi_0^q$ also appears in the last term of (3.41). However, by assuming the theory to be free at $t_0$ no higher order terms of $\phi_0^q$ will be encountered,

$$\frac{i}{\hbar}\int_{\mathcal{C}} \mathrm{d}t L = \left(\frac{i}{\hbar \mathrm{d}t}\right)\int \frac{d^d p}{(2\pi)^d}\left[\phi_0^{cl}\phi_0^q - \phi_1^{cl}\phi_0^q - \frac{\omega_p^2 \mathrm{d}t^2}{2}\phi_0^{cl}\phi_0^q + \cdots\right], \quad (3.43)$$

and it can be seen that $\phi_0^q$ interacts only with $\phi_0^{cl}$ and $\phi_1^{cl}$. After integrating out $\phi_0^q$ the path integral takes the form,

$$\int \mathcal{D}\phi \exp\left(-\frac{1}{\hbar}\int \frac{\mathrm{d}^d p}{(2\pi)^d}\left[\frac{\omega_p(\phi_0^{cl}(p))^2}{2n_p+1} + \frac{1}{\omega_p(2n_p+1)}\left(\frac{\phi_1^{cl}-\phi_0^{cl}\left(1-\omega_p^2\mathrm{d}t^2/2\right)}{\mathrm{d}t}\right)^2\right] + \frac{i}{\hbar}\int_{\mathcal{C}} \mathrm{d}t L'\right), \quad (3.44)$$

where $L'$ denotes $L$ with all $\phi_0^q$ related terms removed. It can now be recognized the new term in the square bracket above as just the time derivative of the scalar, but with finite $\mathrm{d}t$,

$$\dot{\phi}_0^{cl} = \frac{\phi_1^{cl}-\phi_0^{cl}\left(1-\omega_p^2\mathrm{d}t^2/2\right)}{\mathrm{d}t}, \quad (3.45)$$

and that the density matrix gives Gaussian distributions to $\phi_0^{cl}$ and $\dot{\phi}_0^{cl}$ with variances given by,

$$\langle \phi_0^{cl}(p) \Big( \phi_0^{cl}(p') \Big)^\dagger \rangle = \frac{\hbar}{\omega_p} \left( n_p + \frac{1}{2} \right) (2\pi)^d \delta^d(p - p'),$$
$$\langle \dot{\phi}_0^{cl}(p) \Big( \dot{\phi}_0^{cl}(p') \Big)^\dagger \rangle = \omega_p \hbar \left( n_p + \frac{1}{2} \right) (2\pi)^d \delta^d(p - p'). \tag{3.46}$$

In Section 3.2.1, it was discussed that in the perturbation theory of $\phi^q$, the leading order theory has linear $\phi^q$ terms in the exponent, and therefore $\phi^q$ can be integrated out and obtain the classical equation of motion. This however leaves the initial density matrix part, which means that the initialization of the classical theory should respect the distribution (3.46). In practice, ensembles of initializations of $\phi_0^{cl}$ and $\phi_1^{cl}$ can be generated according to (3.45) and (3.46), and then use (3.23) to find the full classical history. As will be shown below, this classical history may then be used as the starting point for Monte Carlo simulations of the path integral although the Monte Carlo process essentially washes out the memory of the classical history (except $\phi_0^{cl}$ and $\phi_1^{cl}$, which are held fixed for a given Monte Carlo run).

In the full quantum field theory, it is also desirable to separate the initial density matrix contribution from the rest of the closed time path in the path integral. There are two reasons for doing this:

(1) It is much easier to write the initial density matrix part in momentum space, and the subsequent dynamical part of the path integral in configuration space.

(2) There is no 'sign problem' in the initial density matrix piece.

The distributions in the initial density matrix piece of (3.46) are ordinary Gaussian distributions, and simple Monte Carlo methods are sufficient to generate samples of $\phi_0^{cl}$ and $\phi_1^{cl}$. Thus $\phi_0^{cl}$ and $\phi_1^{cl}$ should be treated on a different footing from the other integration variables. However, while the initial density matrix part involves only $\phi_0^{cl}$ and $\phi_1^{cl}$, the remaining part of the path integral also contains $\phi_0^{cl}$ and $\phi_1^{cl}$. This separation can be performed legitimately with the requirement that certain conditions are met, as will be described in the next section.

### 3.3.4 Separating variables

When separating $\phi_0^{cl}$ and $\phi_1^{cl}$ from the other integration variables, it is important to following equality holds

$$\int \mathcal{D}\phi_0^{cl}\mathcal{D}\phi_1^{cl} \int \prod_{i=1}^{m-1} \mathcal{D}\phi_i^q \mathcal{D}\phi_{i+1}^{cl} \rho\left(\phi_0^{cl}, \phi_1^{cl}\right) \exp\left(\frac{i}{\hbar}\int_{\mathcal{C}} \mathrm{d}tL'\right) = \int \mathcal{D}\phi_0^{cl}\mathcal{D}\phi_1^{cl} \rho\left(\phi_0^{cl}, \phi_1^{cl}\right) \times \int \prod_{i=1}^{m-1} \mathcal{D}\phi_i^q \mathcal{D}\phi_{i+1}^{cl} \exp\left(\frac{i}{\hbar}\int_{\mathcal{C}} \mathrm{d}tL'\right), \tag{3.47}$$

where $\rho\left(\phi_0^{cl}, \phi_1^{cl}\right)$ is the density matrix part in (3.44), and is a function of $\phi_0^{cl}$ and $\phi_1^{cl}$ only. Therefore to have the equality hold, it is only required that $\int_{\mathcal{C}} dtL'$ be independent of $\phi_0^{cl}$ and $\phi_1^{cl}$. To show that this is true, a feature that has already been explored can be used: The only term in $L'$ containing $\phi_m^{cl}$ is from $\phi_m^{cl}(x)\phi_{m-1}^q(x)$, and by integrating out $\phi_m^{cl}$, we obtain a delta function, $\delta(\phi_{m-1}^q)$. Then by integrating out $\phi_{m-1}^q$, we obtain an integral similar to the previous one, but with $\phi_{m-1}^{cl}$ now playing the role of $\phi_m^{cl}$. We can continue this contraction of the closed time path down to $\phi_1^q$, where we then find $\delta(\phi_1^q)$. It is now known that all $\phi_0^{cl}$ and $\phi_1^{cl}$ appear in $L'$ only through their products with $\phi_1^q$, and therefore by integrating out the delta function of $\phi_1^q$, we know the result has no dependence on $\phi_0^{cl}$ and $\phi_1^{cl}$. Concretely, the result of the integral is

$$\int \prod_{i=1}^{m-1} \mathcal{D}\phi_i^q \mathcal{D}\phi_{i+1}^{cl} \exp\left(\frac{i}{\hbar}\int_{\mathcal{C}} \mathrm{d}tL'\right) = \left(\frac{2\pi\hbar \mathrm{d}t}{\mathrm{d}^d x}\right)^{(N_s)^d(m-1)}. \tag{3.48}$$

which is independent of $\phi_0^{cl}$ and $\phi_1^{cl}$, and so a constant from the point of view of the integral over initial conditions. The separation of variables in (3.47) is therefore valid.

### 3.3.5 One critical point for one initialization

The path integral can be separated into two parts: the initial density matrix and the rest of the path integral. Distinct Monte Carlo simulations were used to sample these different parts.

1. It is assumed that the initial density matrix is known, so $\phi_0^{cl}$ and $\phi_1^{cl}$ can be sampled directly according to the initial density matrix, using typical Monte Carlo algorithms. There is no "sign problem" in the procedure, as in momentum space the distribution function is real and vanishes exponentially as $|\phi| \to \infty$ [153]. It is of note that the initial density matrix is a function of $\phi_0^{cl}$ and $\phi_1^{cl}$ only, but the rest of the path integral also depends on $\phi_0^{cl}$ and $\phi_1^{cl}$. Here sampled fields are denoted as $\tilde{\phi}_0^{cl}$ and $\tilde{\phi}_1^{cl}$, and a Fourier transform is necessary to bring the fields into configuration space for later use. All these $\tilde{\phi}_0^{cl}(x)$ and $\tilde{\phi}_1^{cl}(x)$ are real.

2. Once a $\tilde{\phi}_0^{cl}$ and $\tilde{\phi}_1^{cl}$ are drawn as above, importance sampling according to

$$\int \prod_{i=1}^{m-1} \mathcal{D}\phi_i^q \mathcal{D}\phi_{i+1}^{cl} \exp\left(\frac{i}{\hbar}\int_{\mathcal{C}} \mathrm{d}tL'\right), \tag{3.49}$$

is performed in line with the Generalized Thimble Method, according to an algorithm such as in [2]. Note that the quantum and classical fields start at 1 and 2 in the product, respectively, because $\phi_0^q$ has been integrated out, while $\phi_1^{cl}$ and $\phi_2^{cl}$ are specified as initial data for each initialization. The sampled $\phi_{i+1}^{cl}$ and $\phi_i^q$ with $1 \leq i \leq m-1$ in this procedure are complex. With reweighting (2.3), the expectation value of an operator $\hat{\mathcal{O}}$ can be calculated over a single initialization which is equivalent to,

$$\langle\hat{\mathcal{O}}\rangle_{single} = \frac{\int \prod_{i=1}^{m-1} \mathcal{D}\phi_i^q \mathcal{D}\phi_{i+1}^{cl} \exp\left(\frac{i}{\hbar}\int_{\mathcal{C}} \mathrm{d}tL'\right) \mathcal{O}}{\int \prod_{i=1}^{m-1} \mathcal{D}\phi_i^q \mathcal{D}\phi_{i+1}^{cl} \exp\left(\frac{i}{\hbar}\int_{\mathcal{C}} \mathrm{d}tL'\right)}. \tag{3.50}$$

The full expectation, $\langle\hat{\mathcal{O}}\rangle$, in (3.47) will then be the mean of all the singles, $\langle\hat{\mathcal{O}}\rangle_{single}$.

For the integral in (3.49) above,the analysis in Section 3.2.1 to find all the critical points, this time with $\mathcal{I} = -i\int_{\mathcal{C}} \mathrm{d}tL'/\hbar$. In fact, the conclusions in (3.2.1) are still valid here: At critical points, all $\phi_i^q(x) = 0$, so $\mathcal{I} = 0$, as it consists of odd terms of $\phi^q$, and all $\phi_{i+1}^{cl}(x)$ are uniquely determined through the classical equation of motion (3.23), once $\tilde{\phi}_0^{cl}$ and $\tilde{\phi}_1^{cl}$ are specified. In other words, for each initialization, there exists one and only one critical point. This means that for step 2 above, no multimodal problems that would be caused by the existence of

multiple critical points will be encountered.

However, the initial density matrix could possess multiple saddle points in its distribution. For instance, it is expected to happen in the density matrix of $n$-particle state when $n \neq 0$, or in the case of multi-scalar fields where there exists some symmetry among those scalars. Still, this does not change the conclusion that there exists one and only one critical point for the thimble part of the calculation, and only one thimble/critical point will be encountered.

It is important to note that the derivation is valid on the complexified fields, and the thimble must contribute to the original integral, as the critical point is located on the real field plane. There is one more thing that can be predicted. With each initialization, the averaged phase $\langle e^{-i\mathrm{Im}[\mathcal{I}]+i\arg(\det(J))}\rangle_P$ must be real and positive, due to (3.48).

### 3.3.6 Two-point functions

In order to test the formalism the two-point correlators will be calculated analytically, and compared with numerical results based on the procedure described above. This can be done in the framework of perturbation theory, that is first compute free correlators and then add the loop corrections. In this section only the free two-point functions will be derived, while a 1-loop correction will be included in Section 3.4. See also [3]. Since in the free theory, different momentum modes are independent of each other, the calculation can be focused on a single mode. There are two equivalent ways, up to a constant due to the integration of $\phi_0^q$, to write the path integral,

$$Z = \int \mathcal{D}\phi^+\mathcal{D}\phi^- \exp\left(-\frac{\omega_p}{V\hbar}\frac{\cosh(\hbar\omega_p\beta)\left[(\phi_0^+)^2+(\phi_0^-)^2\right]-2\phi_0^+\phi_0^-}{2\sinh(\hbar\omega_p\beta)}\right)$$
$$\exp\left(\left(\frac{i\mathrm{d}t}{V\hbar}\right)\sum_{i=0}^{m-1}\left[\frac{1}{2}\left(\frac{\phi_{i+1}^+-\phi_i^+}{\mathrm{d}t}\right)^2-\frac{\omega_p^2}{2}\frac{\left(\phi_{i+1}^+\right)^2+\left(\phi_i^+\right)^2}{2}-\left(\phi^+\to\phi^-\right)\right]\right), \tag{3.51}$$

$$Z = \int \mathcal{D}\phi_0^{cl}\mathcal{D}\phi_1^{cl} \exp\left(-\frac{1}{V\hbar}\left[\frac{\omega_p}{2n_p+1}(\phi_0^{cl}(p))^2 + \frac{1}{\omega_p(2n_p+1)}\left(\frac{\phi_1^{cl}-\phi_0^{cl}\cos(\tilde{\omega}_p \mathrm{d}t)}{\mathrm{d}t}\right)^2\right]\right)$$
$$\int \prod_{i=1}^{m-1} \mathcal{D}\phi_i^q \mathcal{D}\phi_{i+1}^{cl} \exp\left(\left(\frac{i}{V\hbar \mathrm{d}t}\right)\phi_i^q(p)\left[2\cos(\tilde{\omega}_p \mathrm{d}t)\phi_i^{cl}(p) - \phi_{i-1}^{cl}(p) - \phi_{i+1}^{cl}(p)\right]\right), \tag{3.52}$$

with constants

$$n_p = \frac{1}{e^{\hbar\omega_p\beta}-1}, \quad \cos(\tilde{\omega}_p \mathrm{d}t) \stackrel{!}{=} 1 - \frac{\omega_p^2 \mathrm{d}t^2}{2}, \tag{3.53}$$

where $\omega_p$ is the frequency in the continuous theory but, because of the discretization, it is $\tilde{\omega}_p$ that propagates on the lattice. In the limit $\mathrm{d}t \to 0$, $\tilde{\omega}_p$ converges to $\omega_p$. For finite $\mathrm{d}t$, it is convenient to replace $\omega_p$ in (3.51) and (3.52) with $\sin(\tilde{\omega}_p \mathrm{d}t)/\mathrm{d}t$. With only Gaussian functions in (3.51) and (3.52), free two-point functions can be calculated as,

$$\langle xx^T\rangle_0 = \frac{\int d^n x\ xx^T e^{-x^T A x}}{\int d^n x\ e^{-x^T A x}} = \frac{A^{-1}}{2}, \tag{3.54}$$

where $A$ and $x$ are understood to be a symmetric complex matrix and a real vector respectively. The size is given by the number of discrete points on the time contour of choice. The above normalization is appropriate for the discrete theory, as in the continuous theory there is a factor of $V$ in the definition. To compensate this, $V$ is taken to be 1 in the following derivation.

### 3.3.7 Time-ordered correlators

It is straightforward to identify the matrix $A$ in (3.51), then calculate its inverse, and use (3.54) to discover that the two-point functions in the $(\phi^+,\ \phi^-)$ basis are

$$\frac{\hbar \mathrm{d}t}{\sin(\tilde{\omega}_p \mathrm{d}t)}\left(\frac{n_p+1}{2}F+\frac{n_p}{2}F^*\right)= \tag{3.55}$$
$$\begin{pmatrix} \langle\phi_0^+\phi_0^+\rangle_0 & \langle\phi_0^+\phi_1^+\rangle_0 & \cdots & \langle\phi_0^+\phi_m\rangle_0 & \cdots & \langle\phi_0^+\phi_1^-\rangle_0 & \langle\phi_0^+\phi_0^-\rangle_0 \\ \langle\phi_1^+\phi_0^+\rangle_0 & \langle\phi_1^+\phi_1^+\rangle_0 & \cdots & \langle\phi_1^+\phi_m\rangle_0 & \cdots & \langle\phi_1^+\phi_1^-\rangle_0 & \langle\phi_1^+\phi_0^-\rangle_0 \\ \vdots & \vdots & \ddots & \vdots & \iddots & \vdots & \vdots \\ \langle\phi_m\phi_0^+\rangle_0 & \langle\phi_m\phi_1^+\rangle_0 & \cdots & \langle\phi_m\phi_m\rangle_0 & \cdots & \langle\phi_m\phi_1^-\rangle_0 & \langle\phi_m\phi_0^-\rangle_0 \\ \vdots & \vdots & \iddots & \vdots & \ddots & \vdots & \vdots \\ \langle\phi_1^-\phi_0^+\rangle_0 & \langle\phi_1^-\phi_1^+\rangle_0 & \cdots & \langle\phi_1^-\phi_m\rangle_0 & \cdots & \langle\phi_1^-\phi_1^-\rangle_0 & \langle\phi_1^-\phi_0^-\rangle_0 \\ \langle\phi_0^-\phi_0^+\rangle_0 & \langle\phi_0^-\phi_1^+\rangle_0 & \cdots & \langle\phi_0^-\phi_m\rangle_0 & \cdots & \langle\phi_0^-\phi_1^-\rangle_0 & \langle\phi_0^-\phi_0^-\rangle_0 \end{pmatrix},$$

where the star denotes complex conjugation, and the matrix $F$ is

$$F=\begin{pmatrix} 1 & e^{-i\tilde{\omega}_p \mathrm{d}t} & \cdots & e^{-im\tilde{\omega}_p \mathrm{d}t} & \cdots & e^{-i\tilde{\omega}_p \mathrm{d}t} & 1 \\ e^{-i\tilde{\omega}_p \mathrm{d}t} & 1 & \cdots & e^{-i[m-1]\tilde{\omega}_p \mathrm{d}t} & \cdots & 1 & e^{i\tilde{\omega}_p \mathrm{d}t} \\ \vdots & \vdots & \ddots & \vdots & \iddots & \vdots & \vdots \\ e^{-im\tilde{\omega}_p \mathrm{d}t} & e^{-i[m-1]\tilde{\omega}_p \mathrm{d}t} & \cdots & 1 & \cdots & e^{i[m-1]\tilde{\omega}_p \mathrm{d}t} & e^{im\tilde{\omega}_p \mathrm{d}t} \\ \vdots & \vdots & \iddots & \vdots & \ddots & \vdots & \vdots \\ e^{-i\tilde{\omega}_p \mathrm{d}t} & 1 & \cdots & e^{i[m-1]\tilde{\omega}_p \mathrm{d}t} & \cdots & 1 & e^{i\tilde{\omega}_p \mathrm{d}t} \\ 1 & e^{i\tilde{\omega}_p \mathrm{d}t} & \cdots & e^{im\tilde{\omega}_p \mathrm{d}t} & \cdots & e^{i\tilde{\omega}_p \mathrm{d}t} & 1 \end{pmatrix}. \tag{3.56}$$

There are two features worth emphasizing in the above expression.

1. In the vacuum, $(n_p = 0)$, the rows and columns corresponding to $\phi_0^+ \to \phi_m$ (i.e. the upper-left part of $F$) lead to $F_{jk} = \exp\left(-i\omega_p|t_j - t_k|\right)$ give the Feynman

propagator, which is defined as [4]

$$-i\langle 0|T\Phi(x)\Phi(y)|0\rangle_0 = \hbar\int\frac{d\omega}{2\pi}\frac{d^dp}{(2\pi)^d}\frac{e^{-i\omega(t_x-t_y)+ip(x-y)}}{\omega^2-p^2-m^2+i\epsilon}$$
$$= -i\hbar\int\frac{d^dp}{(2\pi)^d}\frac{e^{-i\omega_p|t_x-t_y|+ip(x-y)}}{2\omega_p}. \tag{3.57}$$

Thus the correct $i\epsilon$ prescription in the propagator is found. This also means the correlators $\langle\phi_i^+\phi_j^+\rangle_0$ are time-ordered, while the correlators $\langle\phi_i^-\phi_j^-\rangle_0$ are anti-time-ordered. On the other hand, when $n_p \neq 0$, the correlator can be calculated by summing the Matsubara frequencies,

$$\langle 0|\Phi(x)\Phi(y)|0\rangle = -\frac{\hbar}{\hbar\beta}\sum_n\int\frac{d^dp}{(2\pi)^d}\frac{e^{ip(x-y)}}{(i2\pi n/(\hbar\beta))^2-\omega_p^2}$$
$$= \hbar\int\frac{d^dp}{(2\pi)^d}e^{ip(x-y)}\frac{2n_p+1}{2\omega_p}. \tag{3.58}$$

This corresponds to calculating the equal-time elements in (3.55).

2. There exist symmetries in the above two-point functions. For instance, $\langle\phi_i^+\phi_j^+\rangle_0 = \langle\phi_i^-\phi_j^+\rangle_0$ if $i > j$. Although there are many integration variables $\phi_i$ at time $t_i$, there is only one operator $\hat{\Phi}_i$, and it is actually easier to discern the symmetries from the operator formalism,

$$\langle\phi_i^+\phi_j^+\rangle = \theta(t_i-t_j)G^> + \theta(t_j-t_i)G^<,$$
$$\langle\phi_i^+\phi_j^-\rangle = G^<, \qquad \langle\phi_i^-\phi_j^+\rangle = G^>,$$
$$\langle\phi_i^-\phi_j^-\rangle = \theta(t_j-t_i)G^> + \theta(t_i-t_j)G^<, \tag{3.59}$$

with

$$G^> = \langle\hat{\Phi}_i\hat{\Phi}_j\rangle, \qquad G^< = \langle\hat{\Phi}_j\hat{\Phi}_i\rangle. \tag{3.60}$$

[4] To obtain the Feynman propagator in $d+1$ dimension, one can first do the Fourier transform to get the two-point function in the momentum space. Since two-point correlators with different frequencies vanish, one can then write the final expression as a sum or integral over momentum, where as before the sum and integral are treated to be interchangeable.

On the other hand, as in (3.55),

$$G_0^>(t_i - t_j) \propto e^{-i(t_i-t_j)\tilde{\omega}_p}(n_p+1) + e^{i(t_i-t_j)\tilde{\omega}_p} n_p,$$
$$G_0^<(t_i - t_j) \propto e^{i(t_i-t_j)\tilde{\omega}_p}(n_p+1) + e^{-i(t_i-t_j)\tilde{\omega}_p} n_p, \tag{3.61}$$

and this makes manifest the KMS condition $G^>(t_i - t_j) = G^<(t_i - t_j + i\hbar\beta)$ [3].

### 3.3.8 Classical-Classical and Quantum-Classical correlators

The $\phi_i^{cl}\phi_j^{cl}$ or $\phi_i^q\phi_j^{cl}$ could be found through a rotation of $\phi_i^\pm\phi_j^\pm$ in (3.55), but it is useful to derive the expression from scratch with a simple example. Consider $m = 3$. Then the matrix $A$ in (3.54) is

$$A = \left(\begin{array}{cccc:cc} a & -a\cos(\tilde{\omega}_p \mathrm{d}t) & 0 & 0 & -b & 0 \\ -a\cos(\tilde{\omega}_p \mathrm{d}t) & a & 0 & 0 & 2b\cos(\tilde{\omega}_p \mathrm{d}t) & -b \\ 0 & 0 & 0 & 0 & -b & 2b\cos(\tilde{\omega}_p \mathrm{d}t) \\ 0 & 0 & 0 & 0 & 0 & -b \\ \hdashline -b & 2b\cos(\tilde{\omega}_p \mathrm{d}t) & -b & 0 & 0 & 0 \\ 0 & -b & 2b\cos(\tilde{\omega}_p \mathrm{d}t) & -b & 0 & 0 \end{array}\right), \tag{3.62}$$

with

$$x = \begin{pmatrix} \phi_0^{cl} \\ \phi_1^{cl} \\ \phi_2^{cl} \\ \phi_3 \\ \phi_1^q \\ \phi_2^q \end{pmatrix}, \tag{3.63}$$

with constants

$$a = \frac{1}{\hbar(2n_p+1)\mathrm{d}t\sin(\tilde{\omega}_p \mathrm{d}t)}, \quad b = -\frac{i}{2\mathrm{d}t\hbar}. \tag{3.64}$$

Where $\phi_m$ is treated as a $\phi^{cl}$ field. Since $\phi_0^q$ has also been integrated out, in the end there are two more $\phi^{cl}$ fields than $\phi^q$ fields. Following (3.54),

$$\left(\begin{array}{c:c} \langle\phi^{cl}\phi^{cl}\rangle & \langle\phi^{cl}\phi^{q}\rangle \\ \hdashline \langle\phi^{q}\phi^{cl}\rangle & \langle\phi^{q}\phi^{q}\rangle \end{array}\right) =$$

$$\left(\begin{array}{cccc:cc} f & f\cos(\tilde{\omega}_p\mathrm{d}t) & f\cos(2\tilde{\omega}_p\mathrm{d}t) & f\cos(3\tilde{\omega}_p\mathrm{d}t) & 0 & 0 \\ f\cos(\tilde{\omega}_p\mathrm{d}t) & f & f\cos(\tilde{\omega}_p\mathrm{d}t) & f\cos(2\tilde{\omega}_p\mathrm{d}t) & 0 & 0 \\ f\cos(2\tilde{\omega}_p\mathrm{d}t) & f\cos(\tilde{\omega}_p\mathrm{d}t) & f & f\cos(\tilde{\omega}_p\mathrm{d}t) & r\sin(\tilde{\omega}_p\mathrm{d}t) & 0 \\ f\cos(3\tilde{\omega}_p\mathrm{d}t) & f\cos(2\tilde{\omega}_p\mathrm{d}t) & f\cos(\tilde{\omega}_p\mathrm{d}t) & f & r\sin(2\tilde{\omega}_p\mathrm{d}t) & r\sin(\tilde{\omega}_p\mathrm{d}t) \\ \hdashline 0 & 0 & r\sin(\tilde{\omega}_p\mathrm{d}t) & r\sin(2\tilde{\omega}_p\mathrm{d}t) & 0 & 0 \\ 0 & 0 & 0 & r\sin(\tilde{\omega}_p\mathrm{d}t) & 0 & 0 \end{array}\right), \tag{3.65}$$

where

$$f = \left(n_p + \frac{1}{2}\right)\frac{\hbar\mathrm{d}t}{\sin(\tilde{\omega}_p\mathrm{d}t)}, \quad r = -\frac{i\hbar\mathrm{d}t}{\sin(\tilde{\omega}_p\mathrm{d}t)}, \tag{3.66}$$

is found. This may be summarized by the following:

$$\langle\phi_i^{cl}\phi_j^{cl}\rangle_0 = \hbar\left(n_p + \frac{1}{2}\right)\frac{\mathrm{d}t}{\sin(\tilde{\omega}_p\mathrm{d}t)}\cos(\tilde{\omega}_p(i-j)\mathrm{d}t), \tag{3.67}$$

$$\langle\phi_i^{cl}\phi_j^{q}\rangle_0 = -i\hbar\theta(i-j)\frac{\mathrm{d}t}{\sin(\tilde{\omega}_p\mathrm{d}t)}\sin(\tilde{\omega}_p(i-j)\mathrm{d}t), \tag{3.68}$$

$$\langle\phi_i^{q}\phi_j^{cl}\rangle_0 = -i\hbar\theta(j-i)\frac{\mathrm{d}t}{\sin(\tilde{\omega}_p\mathrm{d}t)}\sin(\tilde{\omega}_p(j-i)\mathrm{d}t), \tag{3.69}$$

$$\langle\phi_i^{q}\phi_j^{q}\rangle_0 = 0, \tag{3.70}$$

$$\theta(i-j) = \begin{cases} 1 & i > j, \\ 0 & i \leq j. \end{cases} \tag{3.71}$$

It can be seen for example, that the correlators $\langle\phi_i^q\phi_j^{cl}\rangle$ vanish unless $i < j$, and so correspond to the advanced propagators. Furthermore because of the advanced propagators, any loop correction will not alter $\langle\phi^q\phi^q\rangle = 0$. This result

Figure 3.3: Loop correction to the time-ordered two-point correlator, with the thick solid line being the Feynman propagator.

can be derived much more quickly from the operator formalism (3.59): $\langle\phi^q\phi^q\rangle = \langle\phi^+\phi^+\rangle + \langle\phi^-\phi^-\rangle - \langle\phi^+\phi^-\rangle - \langle\phi^-\phi^+\rangle = 0$.

## 3.4 Loop corrections

In this section the loop corrections to the two-point functions will be considered, and using the continuum expressions in approximate expressions to the discrete cases will be provided. To begin look at the loop corrections to the Feynman propagator, and then see how the computation will be adapted to the $(\phi^{cl}, \phi^q)$ basis.

The Feynman propagator is given in (3.57) as $i\hbar\int\frac{\mathrm{d}\omega}{2\pi}\frac{e^{-i\omega(t_x-t_y)+ip(x-y)}}{\omega^2-\omega_p^2+i\epsilon}$, while the interaction vertex is $-\frac{i\lambda}{4!\hbar}$. The loop correction to the propagator is shown in Figure 3.3, where the thick solid lines correspond to the Feynman propagator. This may be calculated in zero spatial dimensions as follows.

$$
\begin{aligned}
\langle T\hat{\Phi}_1\hat{\Phi}_2\rangle &= i\hbar\int\frac{\mathrm{d}\omega}{2\pi}\frac{e^{-i\omega(t_1-t_2)}}{\omega^2-\omega_p^2+i\epsilon} \qquad (3.72)\\
&+ 12\int\mathrm{d}t\; i\hbar\int\frac{\mathrm{d}\omega_1}{2\pi}\frac{e^{-i\omega_1(t_1-t)}}{\omega_1^2-\omega_p^2+i\epsilon}\frac{-i\lambda}{4!\hbar}i\hbar\frac{\mathrm{d}\omega_2}{2\pi}\frac{1}{\omega_2^2-\omega_p^2+i\epsilon}i\hbar\frac{\mathrm{d}\omega_3}{2\pi}\frac{e^{-i\omega_3(t-t_2)}}{\omega_3^2-\omega_p^2+i\epsilon}+\ldots\\
&= i\hbar\int\frac{\mathrm{d}\omega}{2\pi}\frac{e^{-i\omega(t_1-t_2)}}{\omega^2-\omega_p^2+i\epsilon}\\
&- \frac{\lambda\hbar^2}{2}\int\frac{\mathrm{d}\omega_1}{2\pi}\frac{\mathrm{d}\omega_2}{2\pi}e^{-i\omega_1(t_1-t_2)}\frac{1}{\omega_1^2-\omega_p^2+i\epsilon}\frac{1}{\omega_2^2-\omega_p^2+i\epsilon}\frac{1}{\omega_1^2-\omega_p^2+i\epsilon}+\ldots\\
&= i\hbar\int\frac{\mathrm{d}\omega}{2\pi}\frac{e^{-i\omega(t_1-t_2)}}{\omega^2-\omega_p^2+i\epsilon}\\
&+ i\hbar\int\frac{\mathrm{d}\omega}{2\pi}e^{-i\omega(t_1-t_2)}\frac{1}{\omega^2-\omega_p^2+i\epsilon}\frac{\hbar\lambda}{4\omega_p}\frac{1}{\omega^2-\omega_p^2+i\epsilon}+\ldots\\
&= i\hbar\int\frac{\mathrm{d}\omega}{2\pi}\frac{e^{-i\omega(t_1-t_2)}}{\omega^2-\omega_p^2-\delta m^2+i\epsilon},
\end{aligned}
$$

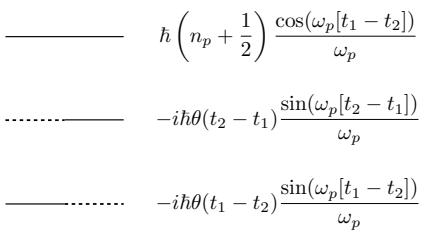


Figure 3.4: Feynman propagators, with the solid line being the $\langle\phi^{cl}\phi^{cl}\rangle_0$ propagator, and the dash-solid line being the $\langle\phi^{q}\phi^{cl}\rangle_0$ propagator.


Figure 3.5: Feynman diagrams for the interactions, with the solid line representing $\phi^{cl}$, and the dashed line corresponding $\phi^{q}$.

where $\delta m^2=\frac{\hbar\lambda}{4\omega_p}$, and $\int\frac{\mathrm{d}\omega}{2\pi}\frac{1}{\omega^2-\omega_p^2+i\epsilon}=-\frac{i}{2\omega_p}$, was used. It is also helpful to use the $(\phi^{cl},\phi^{q})$ basis, for which the continuum expressions can be used to give an approximation to the discrete calculation. Start by noting from (3.67)-(3.70) that the continuum propagators are given by Figure 3.4, while the interaction vertices are given by Figure 3.5.

The loop correction to the advanced propagator can now be calculated, $\langle\phi^{q}\phi^{cl}\rangle$, which can be seen in terms of diagrams in Figure 3.6.

$$
\begin{aligned}
\langle\phi_1^q\phi_2^{cl}\rangle &= -i\hbar\theta(t_2-t_1)\frac{\sin(\omega_p(t_2-t_1))}{\omega_p} \qquad (3.73)\\
&+\int \mathrm{d}t[-i\hbar]\theta(t-t_1)\frac{\sin(\omega_p(t-t_1))}{\omega_p}\frac{\hbar}{2\omega_p}\frac{-i\lambda}{2\hbar}[-i\hbar]\theta(t_2-t)\frac{\sin(\omega_p(t_2-t))}{\omega_p}+...\\
&= -i\hbar\theta(t_2-t_1)\frac{\sin(\omega_p(t_2-t_1))}{\omega_p}\\
&+\int \mathrm{d}t[-i\hbar]\theta(t-t_1)\frac{\sin(\omega_p(t-t_1))}{\omega_p}\frac{\hbar}{2\omega_p}\frac{-i\lambda}{2\hbar}[-i\hbar]\theta(t_2-t)\frac{\sin(\omega_p(t_2-t))}{\omega_p}+...\\
&= -i\hbar\theta(t_2-t_1)\frac{\sin(\omega_p(t_2-t_1))}{\omega_p}\\
&+i\hbar\theta(t_2-t_1)\frac{\hbar\lambda}{4\omega_p^2}\frac{\sin(\omega_p(t-t_1))-\omega_p(t_2-t_1)\cos(\omega_p(t-t_1))}{\omega_p^2}+...
\end{aligned}
$$

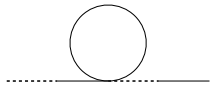

Figure 3.6: Loop correction to the advanced propagator, $\langle\phi^{q}\phi^{cl}\rangle$.

Figure 3.7: There are no non-zero loop corrections to the $\langle \phi^q \phi^q \rangle$ propagator.

where the Heaviside step functions have been used in the propagators to limit the range of the $t$ integration to $t_1 \to t_2$. Noting that the second piece may be written as $-i\hbar\theta(t_2 - t_1)\frac{\hbar\lambda}{4\omega_p}\frac{\partial}{\partial\omega_p^2}\left[\frac{\sin(\omega_p(t_2-t_1))}{\omega_p}\right]$, and so it can be seen that the loop correction corresponds to a correction in $\omega_p^2$ of $\frac{\hbar\lambda}{4\omega_p}$, which matches what was found in the Feynman propagator calculation.

The loop correction for the $\langle \phi^q \phi^q \rangle$ correlator is shown, in the generic sense, in Figure 3.7, where the blocked out region is any set of lines that follow from the Feynman rules of Figures 3.4 and 3.5. However, what is found in such diagrams is the appearance of a loop of either advanced or retarded propagators, which vanishes. As a result there are no perturbative loop corrections to $\langle \phi^q \phi^q \rangle$.

## 3.5 Numerical Simulation

With what has been established in this chapter and the previous one, it is now possible to demonstrate how to carry out numerical simulations. This is done with an example of $\lambda\phi^4$ theory (see also [2, 3]) using the following action,

$$S = \int \mathrm{d}t \mathrm{d}^d x \left[\frac{1}{2}\dot{\phi}^2 - \frac{1}{2}\left(\nabla\phi\right)^2 - \frac{1}{2}m^2\phi^2 - \frac{\lambda}{4!}\phi^4\right]. \tag{3.74}$$

A $1+1$ or even $3+1$-dimensional system simulation would be of immense interest. However in those cases a specific renormalization scheme should be used in order to compare with the result of continuum theory, and as discussed in Chapter 2, higher dimensional simulations suffer heavily from computational limitations. The combination of these two concerns means that at the time this work was performed and at time of writing this was beyond the scope of the present work. Instead, it is straightforward to compare with theoretical predictions in

$0+1$-dimensional system so quantum mechanics[5], where no divergence exists and therefore no renormalization scheme is required. The definitions used here are set up in $d = 1$ spatial dimensions, whereas in the actual simulations presented here, we have further reduced to $d = 0$ quantum mechanics. Throughout the rest of this chapter $dt$ is set to 0.75 for small couplings, and 0.5 for large couplings, while $m = 1$. This is done to ensure the link size is small enough to capture the details of the large couplings, while retaining the maximum possible real time span for the low couplings.

Using a similar but notably different lattice to the one employed in Chapter 2 Space is discretized on $N_s$ sites, with periodic boundary conditions, and the time direction is discretized as above onto $N_t = 2m + 1$ sites going back and forth on the Keldysh contour (see Figure 3.1).

### 3.5.1 Warm-up: Classical statistical approximation

The initial $\phi_0^{cl}(p)$ and $\phi_1^{cl}(p)$ was set according to (3.46), a Gaussian thermal density matrix.[6] Given the distribution, random samples of momentum-space variables $\phi_0^{cl}(p)$ and $\phi_1^{cl}(p)$ were generated which were then Fourier transformed to position space $\phi_0^{cl}(x)$ and $\phi_1^{cl}(x)$. At this point the classical field evolution can be calculated through the equation of motion,

$$\frac{\tilde{\phi}_{i+1}^{cl}(x) - 2\tilde{\phi}_i^{cl}(x) + \tilde{\phi}_{i-1}^{cl}(x)}{dt^2} - \frac{\tilde{\phi}_i^{cl}(x+1) - 2\tilde{\phi}_i^{cl}(x) + \tilde{\phi}_i^{cl}(x-1)}{dx^2} + m^2\tilde{\phi}_i^{cl}(x) + \frac{\lambda}{6}\left(\tilde{\phi}_i^{cl}(x)\right)^3 = 0. \quad (3.75)$$

$\tilde{\phi}$ is used to refer to the fact that these are not variables of integration in the path integral. They represent the critical configuration in the complexified field configuration space, $\phi^{cl} = \tilde{\phi}^{cl},\ \phi^q = 0$, from which Monte-Carlo simulations will

[5]For the application of Lefschetz thimble on quantum mechanics from a different perspective, see [74, 154].

[6]For initial $n$-particle states, the expression given in (3.35) could be used, with some Hermite polynomial function.

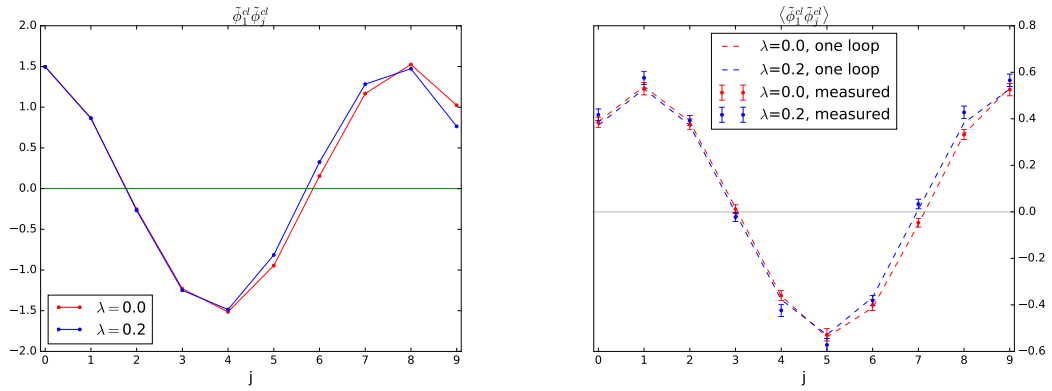


Figure 3.8: Correlators for a single classical realisation (left) and averaged over initial conditions (right).

be launched in later sections.

Figure 3.8 (left) shows the correlator for a single such classical trajectory. In a classical simulation, only the classical-classical correlator can be computed. By averaging over the ensemble of initial conditions, the "classical-statistical" approximation to quantum dynamics can be recovered, as shown in Figure 3.8 (right). The results for a free field, $\lambda = 0$ and an interacting theory $\lambda = 0.2$ are shown here. The correlators are very similar, but deviate enough that it is possible to tell the difference with moderate statistics. The loop calculation is discussed in Section 3.4, where it is found that at 1-loop all that is needed is to make the replacement $\omega_p^2 \to \omega_p^2 + \frac{\hbar\lambda}{4\omega}$, and evidently changes nothing in the $\lambda = 0$ case. This is substituted into (3.53) to find $\tilde{\omega}_p$, which is then used in expression (3.67) for the classical-classical correlator.

### 3.5.2 Warm-up: Quantum average of a single initial realisation

Going beyond the classical approximation then amounts to performing the complete path integral, the integrations of all the field variables not associated with the initial condition, see Figure 3.9. As in Section 3.3.5, the integrand can be written as $e^{-\mathcal{I}}$, with $\mathcal{I} = -i\int_{\mathcal{C}} \mathrm{d}t L'/\hbar$. It turns out that the exponent $\mathcal{I}$ is more conveniently expressed in the $(\phi^+,\ \phi^-)$ basis than using $(\phi^{cl},\ \phi^q)$, as the inter-

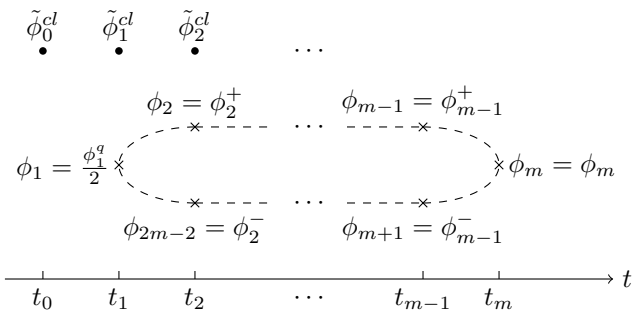


Figure 3.9: The variables to be integrated over on the real-time contour, after the initial conditions are fixed.

action terms are simpler there. It is therefore prefereable to switch to $(\phi^+,\ \phi^-)$, except that at $t_1$ should be treated differently, since $\phi_1^{cl}$ is counted into the initial condition, leaving $\phi_1^q$ as the only variable at $t_1$. The exponent $\mathcal{I}$ also contains $\tilde{\phi}_0^{cl}$ and $\tilde{\phi}_1^{cl}$, and may be written as

$$\begin{aligned}\mathcal{I} = \left(\frac{-i\mathrm{d}x}{\hbar}\right)\sum_x \Bigg\{ & 2\phi_1(x)\frac{\tilde{\phi}_2^{cl}(x)}{\mathrm{d}t} - \frac{\lambda \mathrm{d}t}{3}\tilde{\phi}_1^{cl}(x)\big(\phi_1(x)\big)^3 - \phi_2(x)\frac{\tilde{\phi}_1^{cl}(x)}{\mathrm{d}t} \\ & + \phi_{2m-2}(x)\frac{\tilde{\phi}_1^{cl}(x)}{\mathrm{d}t} + \sum_{i=1}^{2m-2}\frac{\big[\phi_{i+1}(x)-\phi_i(x)\big]^2}{2\Delta_i} \\ & + \left(\frac{\Delta_i+\Delta_{i-1}}{2}\right)\left(-\frac{\big[\phi_i(x+1)-\phi_i(x)\big]^2}{2\mathrm{d}x^2} - \frac{m^2}{2}\phi_i^2(x) - \frac{\lambda}{24}\phi_i^4(x)\right)\Bigg\}, \end{aligned} \tag{3.76}$$

where a field redefinition has been adopted as illustrated in Figure 3.9, and the time differences are denoted as

$$\Delta_i = \begin{cases} \mathrm{d}t, \text{ if } 1 \le i < m; \\ -\mathrm{d}t, \text{ if } m \le i < 2m-1. \end{cases} \tag{3.77}$$

In the exponent, there are terms like $\phi_1^q(x)\tilde{\phi}_0^{cl}(x) - 2\phi_1^q(x)\tilde{\phi}_1^{cl}(x) + \cdots$, where $\tilde{\phi}_0^{cl}$ and $\tilde{\phi}_1^{cl}$ can appear. In fact, an extra $\tilde{\phi}_2^{cl}(x)\phi_1^q(x)$ term will cancel out these linear-in-$\phi_1^q(x)$ terms, due to the equation of motion (3.75). Therefore, it is possible to substitute these terms with $\tilde{\phi}_2^{cl}(x)$ term only and this considerably simplifies expression (3.76). Given that $\phi_1^{cl}$ is part of the specified initial data, $\phi_1 = \phi_1^q/2$ is defined to ensure that at site 1 only $\phi_1^q$ is included in the dynamical part of the

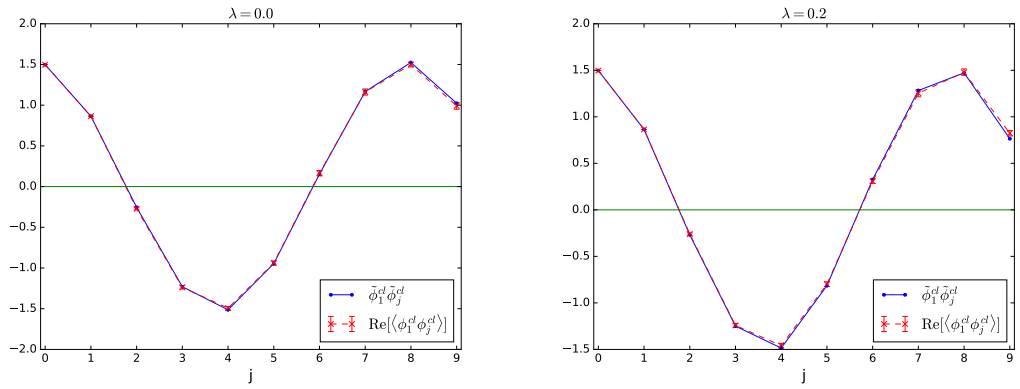


Figure 3.10: The classical correlator for a single initial condition, and the corresponding quantum averaged correlator. For $\lambda = 0.0$ (left) and 0.2 (right).

path integral. To arrive at (3.76),

$$\phi_{2m-1} = -\phi_1, \quad \Delta_0 = -\mathrm{d}t, \tag{3.78}$$

have been used. There are $N_{tot} = N_s(2m-2)$ variables in total, and for clarity a more compact notation will be adopted merging space and time labels into a single integer $a$.

For all the field variables $\phi_a$, the Monte-Carlo chains for the dynamical part of the path integral will be started from $\tilde{\phi}_a$, the classical critical-point configuration. In subsequent Monte-Carlo steps, these will be changed into new real values $\varphi$.

For the Lefschetz Thimble Method, then $J(\tau = 0)$ is determined by the eigenvectors of positive eigenvalues [44] of the Hessian evaluated on the critical point field configuration. For more on algorithms based on the Lefschetz Thimble Method, see [44, 45, 46]. And for more on algorithms based on the Generalized Thimble Method, see [47, 48, 104, 155, 156, 157, 109].

The algorithm used to generate these results deviates from that used in Chapter 2 in only one respect; the addition of the sampling of the initial conditions. In practice this represents $N$ simulations using different initial conditions drawn from (3.46). These are statistically independent by construction and are therefore generally parallelised where possible.

In Figure 3.10, the correlator for a single classical trajectory is shown, and com-

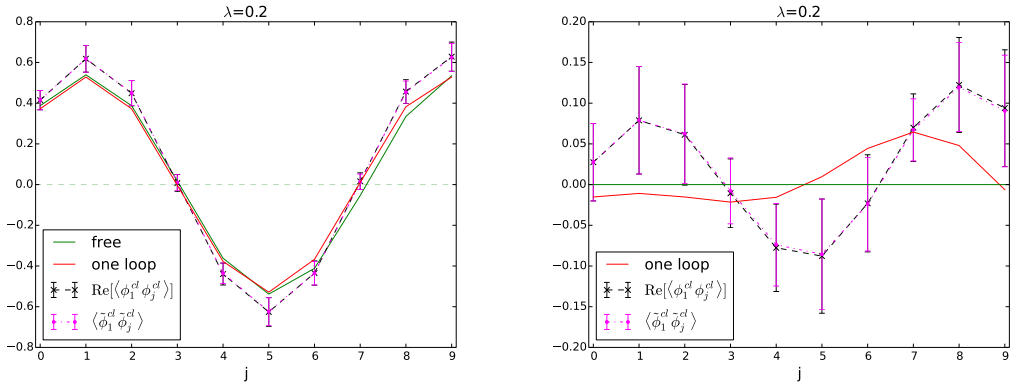


Figure 3.11: The full classical-statistical and quantum correlators (cl-cl) for a free and interacting theory at $\lambda = 0.2$. The figure on the right shows the result of subtracting the free propagator. The red line is the perturbative 1-loop result. In the right hand plot, the free values have been subtracted from the coupled values.

pared to the correlator when averaging over the simulation variables (but without averaging over initial conditions). In the left-hand plot for the free theory ($\lambda = 0$), in the right-hand plot including interactions ($\lambda = 0.2$). It can be seen that the averaging is has only a small effect for the free theory, whereas including a moderate interaction strength there is statistically significant effect, increasing over time.

### 3.5.3 All warmed up: Full evolution

The two part simulations can now be conducted, the inner (Monte-Carlo integration on the thimble) and outer (initial conditions) integration and combined to find the full quantum correlator, given an initial Gaussian state. The simulations presented here use $n_{initial} = 200$ initializations, with $5 \times 10^5$ Metropolis updates for single initialisation, in order to give small enough statistical errors.

Figure 3.11 (left) shows the two-point cl-cl correlator for the full classical-statistical simulation (pink) and the full quantum simulation (black). Overlaid also the 1-loop perturbative result (in red). Figure 3.11 (right) arises from subtracting the free propagator, to highlight the contribution from interactions. It can be seen that the classical-statistical approximation performs very well at these values of the coupling, and that it would seem that the differences arising from quantum

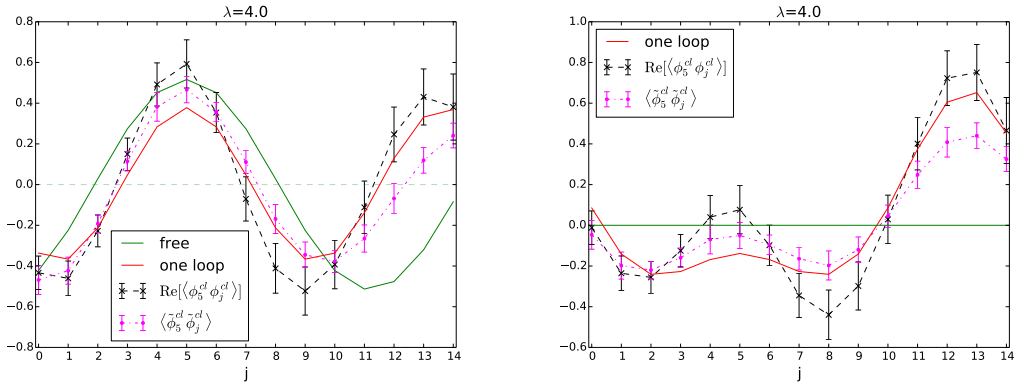


Figure 3.12: On the left, the full quantum correlators (cl-cl) for a free and interacting theory at $\lambda = 4$. On the right, when subtracting the free propagator.

averaging each initial condition (Figure 3.10) are in turn largely washed out when averaging over initial conditions. The 1-loop approximation shown in red is distinct from the other two curves, showing that the system is not in the extreme small-coupling limit, and so the agreement between classical-statistical and quantum approaches does apply to an interacting system.

Having established a match between this thimble technique and established peterbative results, the coupling $\lambda$ can be increased beyond the limits of the peterbative regime. In Figure 3.12 the $\lambda = 4$ case is shown, where by visual inspection it is possible to distinguish the classical-statistical (pink) from the fully quantum result (black). They are both different from the free theory (green) and the 1-loop approximation (red). Results using this new technique are compared to those generated using the forced equilibrium method in Chapter 2 in Figure, where similar to Figure 2.2, the Feynman propagator has been calculated, and compared with a semi-analytic solution. The initial conditions were sampled across 150 chains, but otherwise the system is identical to that presented in Chapter 2. As can be seen, the new technique's results match well, however the error is considerably larger, a consequence of the additional sampling that must be done to account for a density matrix which is inherently separated from the rest of the MCMC chain. It is worth noting that the error grows as the correlation function moves away from the initial two lattice sites, the fact they are held constant suppressing the error in the lattice sites around them. This effect would be expected to trail off as the lattice grows in the time dimension, but unfortunately cannot be verified

here due to computational limits.

A direct comparison can be made with the lattice based density matrix presented in Chapter 2, as shown in Figure 3.13. The new results are compared with the results shown in Figure 2.2, and show while the new technique matches previous results, the error is considerably increased by the larger parameter space represented by the density matrix. As before, the plots represent $\langle \phi_i \phi_j \rangle$ for a range of $i$ values. A single oscillation is used for computational efficiency, however in principle the simulations could be done with more time sites with no issue.

## 3.6 Conclusions

Real-time quantum dynamics is well-defined in terms of the Schwinger-Keldysh formalism, and although the classical-statistical approximation often does very well in some cases, simulations of truncated Kadanoff-Baym equations have shown that quantum corrections are important in other contexts.

This chapter has presented a new approach to calculating real time correlators, that does not require the system to be in equilibrium, directly from the path integral. This is possible through Monte-Carlo sampling as the sign problem inherent to the complex action can be softened by flowing the field variables into the complex plane.

In effect this represents a number of technical developments necessary to generalise the work of [1, 2] to initial-value problems. For a discrete space-time, this chapter has shown that the scalar field path integral can be separated into two parts: the initial density matrix and the following dynamical part. Under such a separation there exists one and only one critical point, which helps when either the Lefschetz Thimble Method or the Generalized Thimble Method are implemented on the dynamical part. A symmetric discretization of the theory has been used, in both a symmetric Feynman kernel and a symmetric time contour. With such a discretization all the critical points can be found.

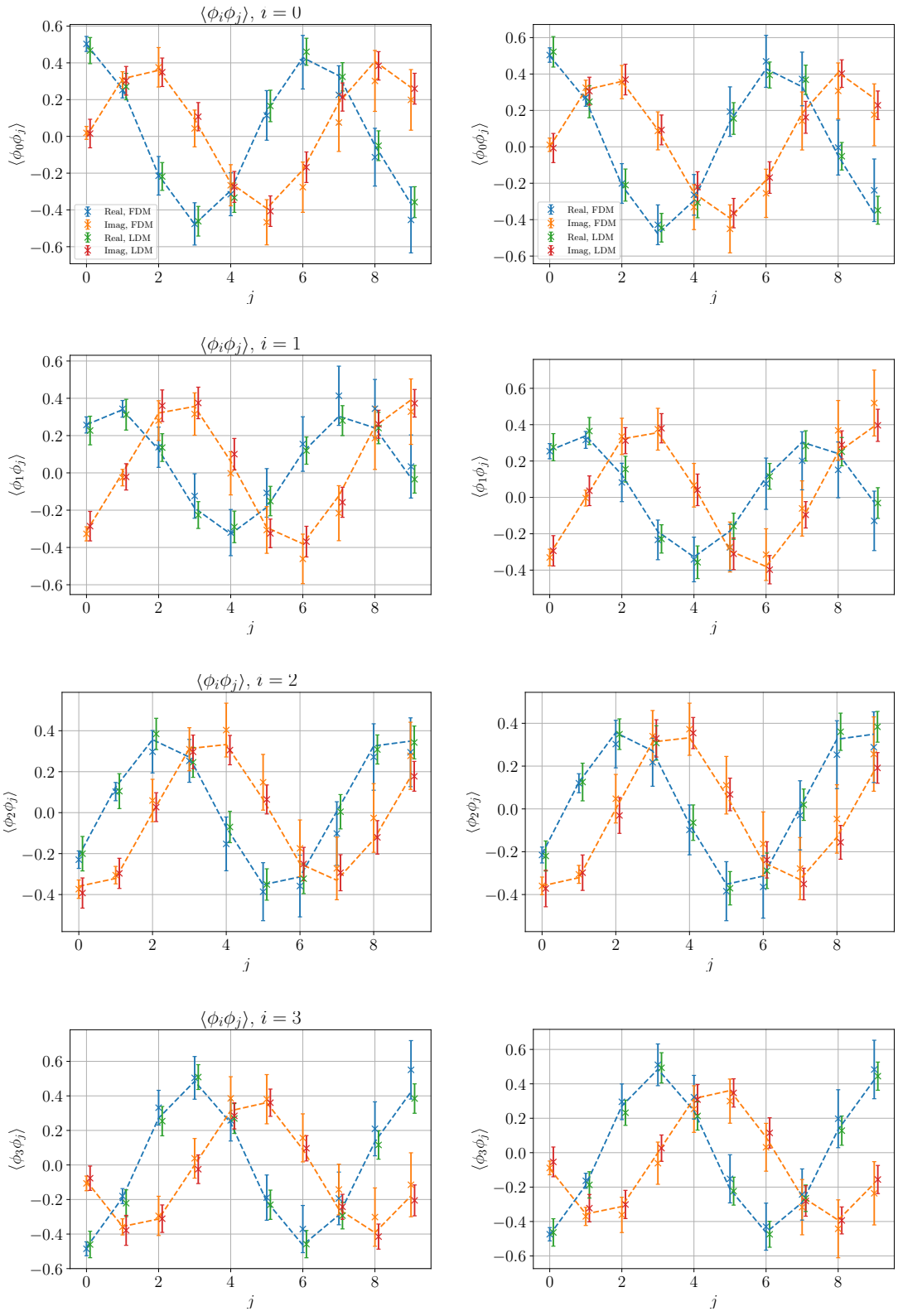


Figure 3.13: Comparing the results of calculating the Feynman correlators using this Free Density matrix (FDM in the legend) technique and those using a lattice based density matrix (LDM) as in Figure 2.2.

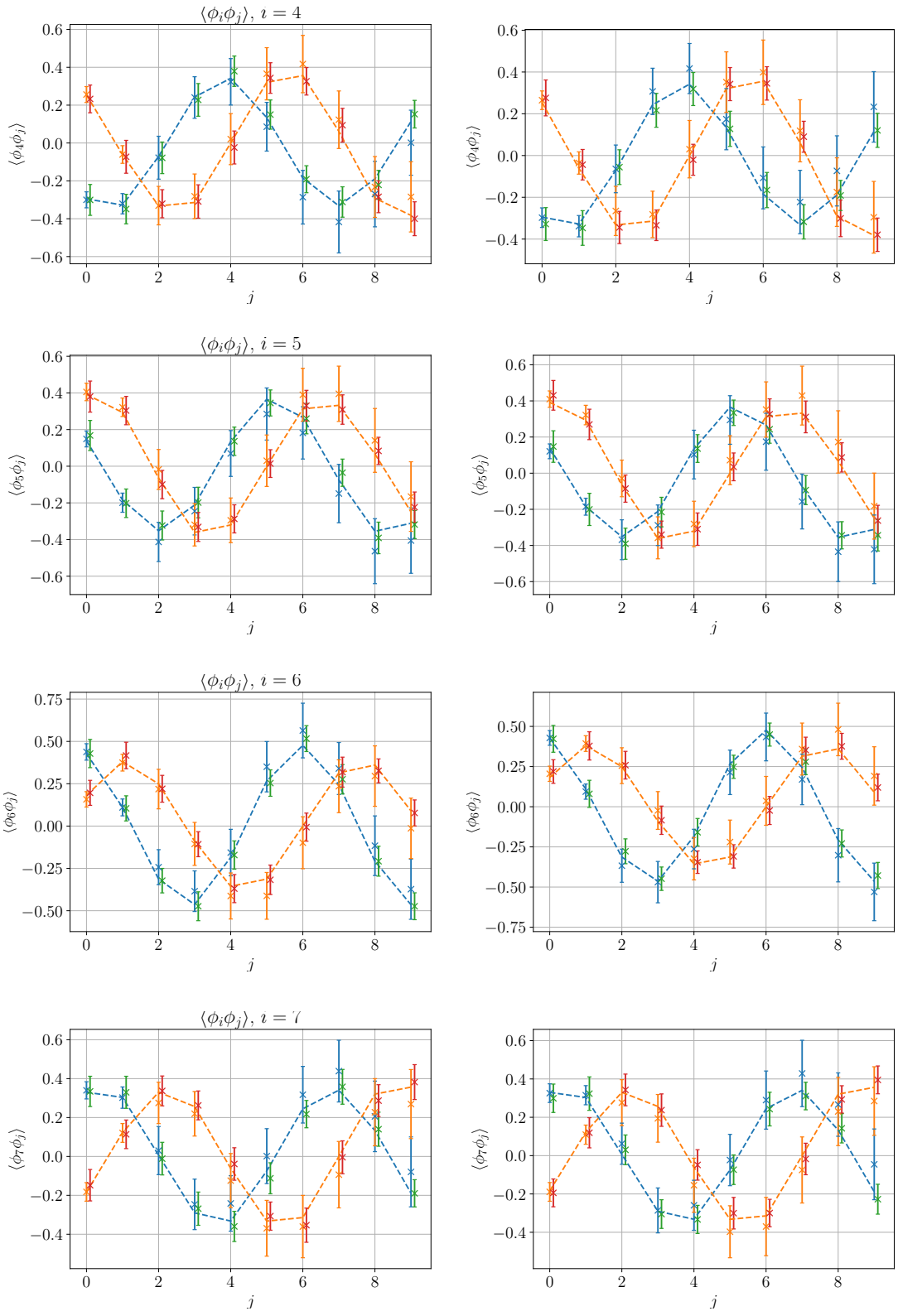


Figure 3.13: Comparing the results of calculating the Feynman correlators using this Free Density matrix (FDM in the legend) technique and those using a lattice based density matrix (LDM) as in Figure 2.2.

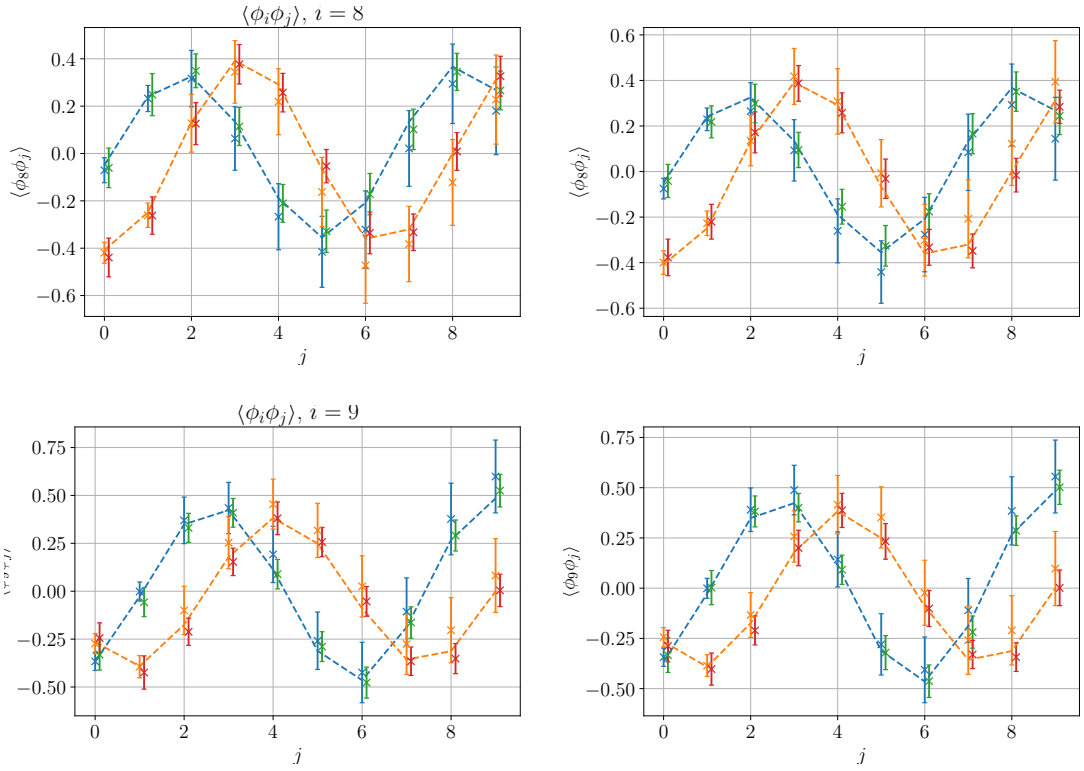


Figure 3.13: Comparing the results of calculating the Feynman correlators using this Free Density matrix (FDM in the legend) technique and those using a lattice based density matrix (LDM) as in Figure 2.2.

To demonstrate the implementation of this approach, the real-time propagator for a scalar field in 0+1 dimensions has been computed with a Gaussian (free-field) initial condition. Good statistical convergence was found, and agreement with the free analytic correlator (up to discretization errors). Once interactions were included and increased it was found that it was possible to distinguish coupled correlators from the free case, that the 1-loop perturbative result began to fail, and that for very large couplings the classical-statistical approximation became unreliable.

In this chapter the initial density matrix of the free theory was used as in this case $\phi_0^q$ can be integrated out explicitly, resulting in the familiar initial distribution of $\phi_0^{cl}$ and $\dot{\phi}_0^{cl}$. There is no difficulty in extending the calculation to the case of a more general density matrix, as long as the initialization for $\phi_0^{cl}$ and $\dot{\phi}_0^{cl}$ can be generated. Note however, that a density matrix containing $\phi_0^q$ and $\phi_1^{cl}$ might still be plagued with the "sign problem" owing to the appearance of a factor of $i\phi_1^{cl}\phi_0^q$ in (3.43). This only affects the density matrix part of the path integral, so the thimble approach may still be used for the remaining dynamical part. On the other hand, this chapter has also shown that real physical situations can be modeled by turning on the interaction after the initialization, either instantly or gradually, and the method developed in here can naturally deal with time dependent interaction coefficients, although none are presented due to computational limitations.

The computational cost of the thimble approach is $a\mathcal{O}(n^3)$, with $n$ the number of variables and $a$ the number of samples. By separating the simulation into two parts with $n_1$ and $n_2$ variables respectively, the cost becomes $a_1\mathcal{O}(n_1^3)+a_1a_2\mathcal{O}(n_2^3)$, corresponding to generating $a_1$ different initialisations and for each initialization $a_2$ Monte Carlo samples. If $a$ is not sensitive to $n$, the cost will be smaller than $a\mathcal{O}((n_1+n_2)^3)$, when $n_1$ and $n_2$ are big numbers. Given this it is possible to further separate the path integral into more pieces, with each piece depending only on its predecessor but not successor, as each piece becomes an initial condition for the part that follows it. This remains an open avenue of research.

# Chapter 4

# Computational Optimisations and the Second Field

This chapter is based on work published in [41].

## 4.1 Computational Optimisations

It has now been demonstrated that this technique can simulate systems that are, in principle, out of equilibrium. This has however come at a computational cost, implementing the 'two step' sampling in Chapter 3 has increased the run time by an order of magnitude. To mitigate this, significant effort was made to find the fastest (by wall clock) way to calculate physically significant results. To that end the results in this section will be produced using the action outlined in Chapter 3 with the self interaction term removed so that the (now free field) action reads

$$\mathcal{I} = \left(\frac{-i}{\hbar}\right)\left[\frac{2\phi_1\tilde{\phi}_2^{cl}}{\mathrm{d}t} - \frac{\phi_2\tilde{\phi}_1^{cl}}{\mathrm{d}t} + \frac{\phi_{2m-2}\tilde{\phi}_1^{cl}}{\mathrm{d}t} + \right. \tag{4.1}$$

$$\left. \sum_{i=1}^{2m-2} \frac{(\phi_{i+1}-\phi_i)^2}{2\Delta_i} - \left(\frac{\Delta_i + \Delta_{i+1}}{2}\right)\left(\frac{1}{2}m^2\phi_i^2\right)\right], \tag{4.2}$$

The free field has a number of simplifying properties. Firstly, the exact solution for the two-point function is known to be a nicely oscillating (and therefore well-

behaved) function, meaning that amplitudes and errors will be comparable for all $j, k$ pairs. Second, since the flow equation is linear in $\phi$, the right-hand side of (1.55) does not depend on $\phi$. As a result, the Jacobian in the flow evolution is constant, and does not need to be recomputed at every Monte Carlo and time step. This reduces the computational cost by about 95%, meaning that it is ideal for finding the optimal parameters for error reduction, under the assumption that these parameters do not vary enormously when an interaction is introduced.

These simulations are performed with $dt = 0.75$ temporal extent of the lattice is 10. The number of initial conditions $N_{init}$ "number of MC chains", the flow time $\tau_{max}$, the parameter $\delta$ and the length of the MC chains $N_{MC}$ are then varied.

For the purpose of optimisation, the 'number of merit' used here is the statistical error on the propagator, selecting the largest value over the 10 time points. This is chosen because the classical-classical propagator is in theory an entirely real valued function in the vacuum case. This reduces any potential confusion regarding the error of a complex number. In Figure 4.1 the correlation plots of this number of merit as the parameters of the algorithm are varied. It can be seen that the error improves with increasing MC chain length, increasing proposal size $\delta$ and increasing flow time $\tau$. The number of initial conditions is less important, provided it is large enough to convincingly sample the initial Gaussian distribution[1].

It can also be seen that the effects are uncorrelated, so that there is no favoured combination of parameters, that improves accuracy beyond the combined individual effects. The runtime depends linearly on $N_{init}$, $N_{MC}$ and $\tau_{max}$, since it is just how many times the algorithm is run. On the other hand, the runtime does not depend on $\delta$. This can however not be increased indefinitely, as shown in Figure 4.2, which shows the acceptance rate of MC steps, as $\delta$ is increases. This drops substantially at a maximal value $\delta_{max}$ (in this case 3.15, for $\tau_{max} = 1$).

In general, the flowed field manifold can have a very complicated geometry. Having knowledge of the curvature in different directions along the manifold would

[1]For a purely classical simulation, the statistical error decreases as $N_{init}^{-1/2}$.

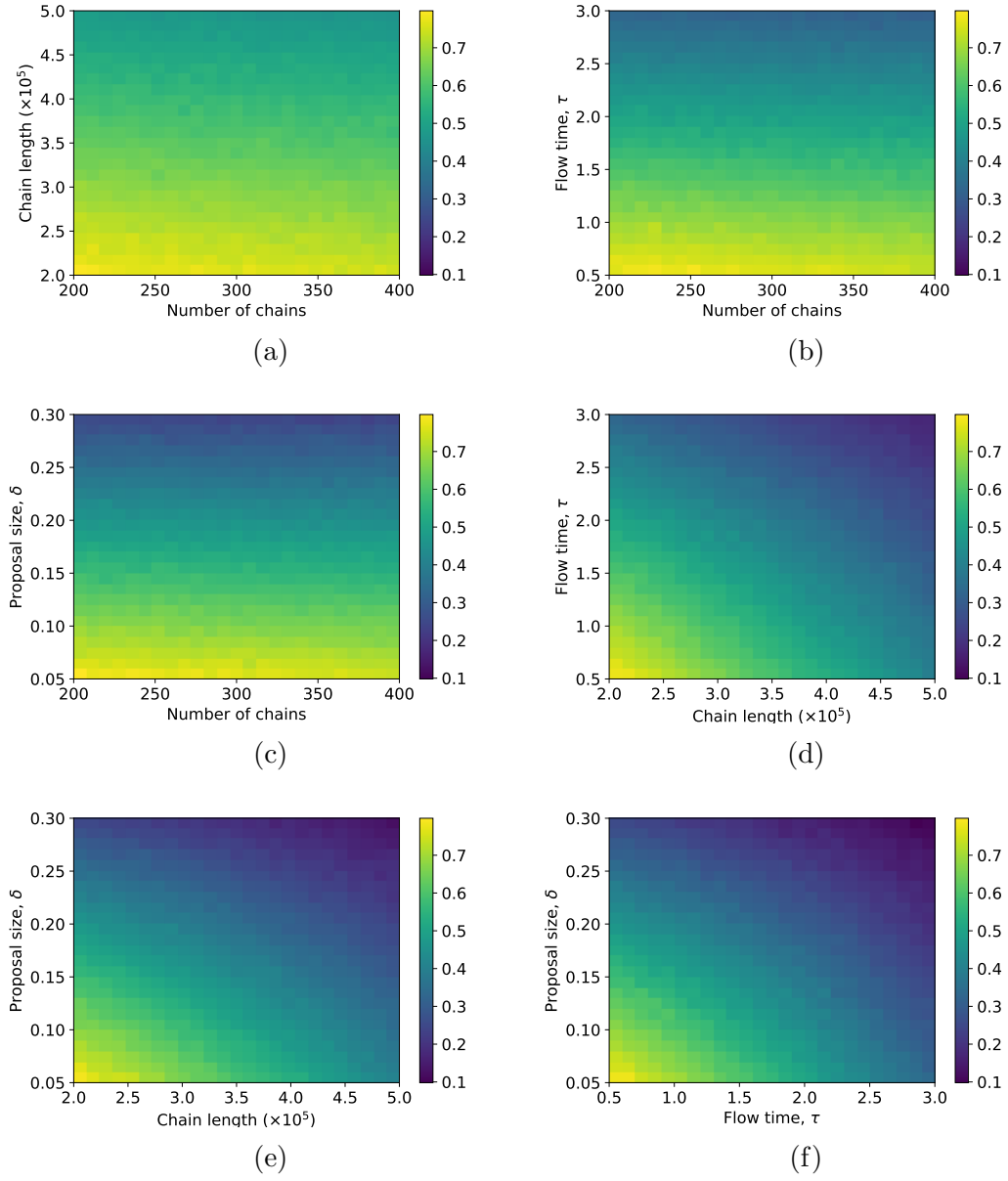


Figure 4.1: A comparison of the maximum error on a test correlator for various simulation parameters

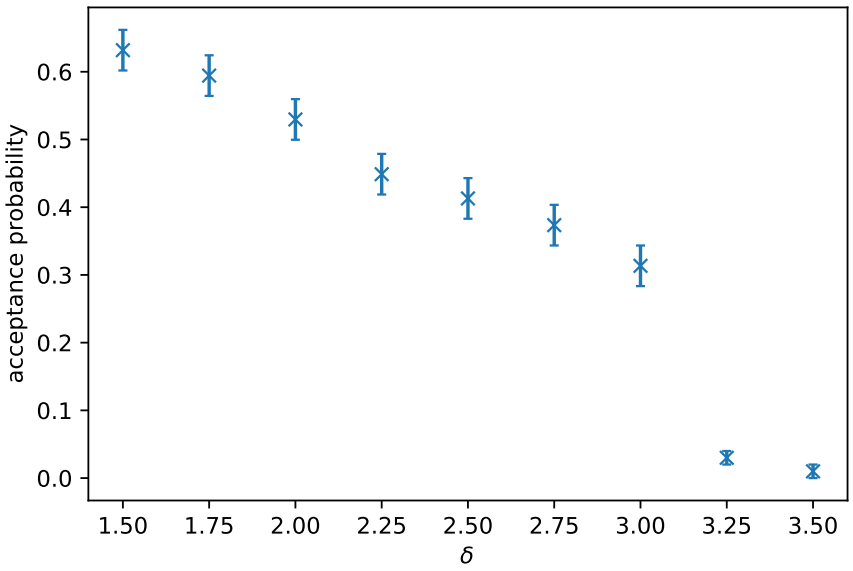


Figure 4.2: Probability of a proposal being accepted for $\tau = 1$. Note that while acceptance probability decreases with step size, the 'speed' around the manifold increases as the larger step size compensates.

allow us to generate random increments with different $\delta$ along each direction, for optimal speed through field configuration space. However, without such detailed knowledge of the geometry, this leaves selecting only one, global $\delta$. The hope is that for a given set of parameters, $\delta_{max}$ can be identified. Once the error can no longer be improved by increasing $\delta$, further improvements must come from increasing the flow time $\tau_{max}$ and the chain length $N_{MC}$.

The effect of the chain length on the error is expected to be $\propto N_{MC}^{1/2}$, although there are considerations to do with the autocorrelation time. The dependence on the flow time seems to be approximately linear $\propto 1/\tau_{max}$.

In summary the flow time should be increased until the reward is cancelled by the corresponding $\delta_{max}$ decreasing. Once this has been optimized, any further computing power should be used to increase the chain length and the number of chains/initial conditions. The chain length should in any case at least be large enough that ergodicity is achieved and much longer than the autocorrelation time. Similarly, the number of chains/initial conditions must be large enough that the initial condition distribution is well sampled. Each chain is independent providing an excellent opportunity for parallelisation.

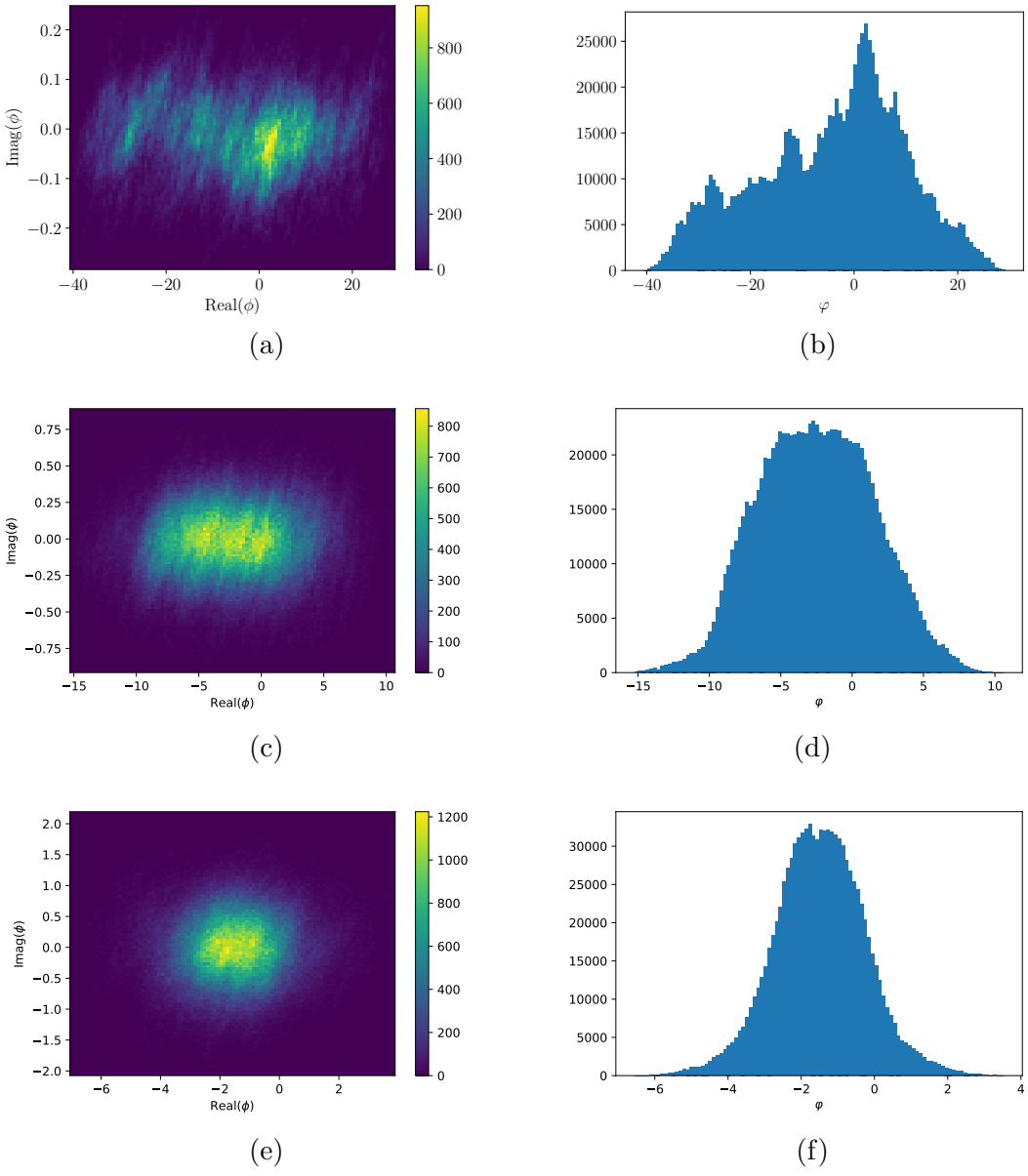


Figure 4.3: Complex domain of a single field variable during the MC sampling of a multivariable system (left) and the corresponding domain in terms of the un-flowed real variable (right). Top to bottom, $\tau_{max} = 0.01,\ 0.1,\ 1$.

For the simple one-variable example of Figure 1.7, the Thimble and the Generalized Thimble, to which the field manifold will flow were computed analytically. For multiple variables this is highly non-trivial, and in a MC sampling of coupled variables it is the entire multidimensional manifold including initial conditions, that is sampled. Still, it may be illustrative to show the domain in the complex plane, that one single variable samples during the course of the entire MC simulation. This will depend on the flow time $\tau_{max}$, where for $\tau_{max} = 0$, the domain is the real axis. In Figure 4.3, this domain is shown for three different flow times, $\tau_{max} = 0.01, 0.1, 1$. It can be seen that for larger flow times, a larger region of the complex plane is sampled (note the different scales on the axes). In the right-hand panels, the corresponding distribution of the real-valued variables $\varphi$ is shown. As the flow time becomes larger, they cluster around an ever smaller range near, but displaced from, the origin. This is qualitatively similar to the one-variable example.

## 4.2 Attempts to Make a 1+1D System

Initially the intention of these optimisations had been to accurately simulate a single field in an out of equilibrium state and in $1 + 1$D, such as a 'top hat' momentum distribution. This was proposed as the behaviour of such a system is well understood, and should decay towards a Bose-Einstein distribution. However even using the optimisations outlined in Section 4.1, the probing of $1 + 1$D non-equilibrium systems proves computationally challenging. A number of attempts were made varying the number of spacial layers used, the physical and temporal lattice spacing, and the height of the 'top hat' relative to the vacuum state. All of these, with the exception of the variation of the spacial layers, failed to effectively resolve the problem as they addressed the very real but ultimately subdominant problem of the computational cost of solving the flow equations by tinkering with parameters but cannot affect the primary source of additional computational complexity; the order of magnitude increase in the number of lattice points and corresponding increase in the size of the Jacobian, and the increased

complexity of the initial condition parameter space which would necessitate more chains being produced to ensure it was sufficiently explored. Altering the number of spatial layers addresses both of these concerns, but can only be reduced so far before edge effects would become dominant. Consequently a new approach was needed, and the $1 + 1$D simulations were shelved.

Despite the failure, interesting insight into the behaviour of the proposal mechanism was gained. In order for the MCMC routine to be successful it needed a reasonable acceptance probability. However, for all but the smallest $\delta$, the acceptance rate was close to zero, typically $< 10^{-4}$. As the number of degrees of freedom on the manifold increases, the step size must drop to maintain the acceptance probability. This appears to be because as the manifold increases in scale, the likelihood of the proposal being of net benefit decreases. This shows that the efficiency saving technique invoked by "sweeping" the lattice as discussed in Chapter 2 has its limits. There are two possible methods to resolve this, a single site updating technique more typical in lattice field theory and an updated version of one proposed in [1], which involves weighting the proposals in each direction by the relevant eigenvalue of the Jacobian. Unfortunately neither technique was tested extensively as it was already evident from the wall-clock time required to process each update that this would exceed the computational resources available.

The only significant complexity in implementing a single site update mechanism is to ask, what does that mean in this context? In traditional lattice field theory, without the thimble manifold, understanding the difference between updating all the sites at once compared to updating a single site per MC update is trivial. Here, due to the non trivial Jacobian, updating only a single site on either the real manifold or the manifold of integration will result in all lattice sites being updated on the other. This in practice meant only changing step 2. of the algorithm as outlined in Chapter 2 from drawing an entire vector from the distribution to drawing a single value and assigning it to a random element in a vector of the same size as previously, and transporting that vector back to the real manifold as before. This is equivalent to updating a single site on the manifold, however the

vector is completely distorted by the transformation back to $\mathbb{R}_n$ and as a result all elements of the real valued field are changed. This approach did significantly improve the acceptance probability, however at a practical cost. By doing this the effective speed that the Markov chain can move around the lattice is reduced by $\mathcal{O}(N^{1/2})$, as each step is effectively smaller. Consequently the Markov chain needs to be considerably longer to achieve the same results, and as the Jacobian still needed to be calculated at each update, the wall-clock time increased using this technique.

The second method involves calculating the eigenvalues and eigenvectors of the Jacobian, referred to as $\epsilon_n$ and $\rho^n$ respectively. Using these, the real-manifold site values can be written as

$$\varphi_i = \sum_\alpha c_\alpha \rho_i^\alpha, \tag{4.3}$$

where $c_\alpha$ are complex valued constants the imaginary parts of which are calibrated to ensure that $\varphi$ is real. Updates to the real values (and through flowing the updated real values, the thimble manifold values) can now be made in a manner that respects the topology of the thimble, by updating the real parts of $c_\alpha$ such that

$$c_\alpha^{\text{new}} = c_\alpha^{\text{old}} + \frac{\Delta}{|\epsilon_\alpha|^k}, \tag{4.4}$$

where $\Delta$ represents a random proposal from a Gaussian, comparable to the one drawn in the original algorithm. $k$ represents a parameter that controls how strongly the manifold's topology affects the proposal size. As smaller $\epsilon_\alpha$ implies a more flat region in the direction of $\rho_\alpha$, $k < 1$ suppresses steps in flat directions while increasing them in more curved directions compared to just diving by the eigenvalue. The imaginary part of $c_\alpha$ must then be updated to ensure that $\varphi$ remains real. Figure 4.4 compares the acceptance probability over $10^5$ MC updates with the value of $k$, with a maximum at $k \approx 0.5$. This matches the algorithm described in [1], although no justification is given in the paper for why this value is chosen.

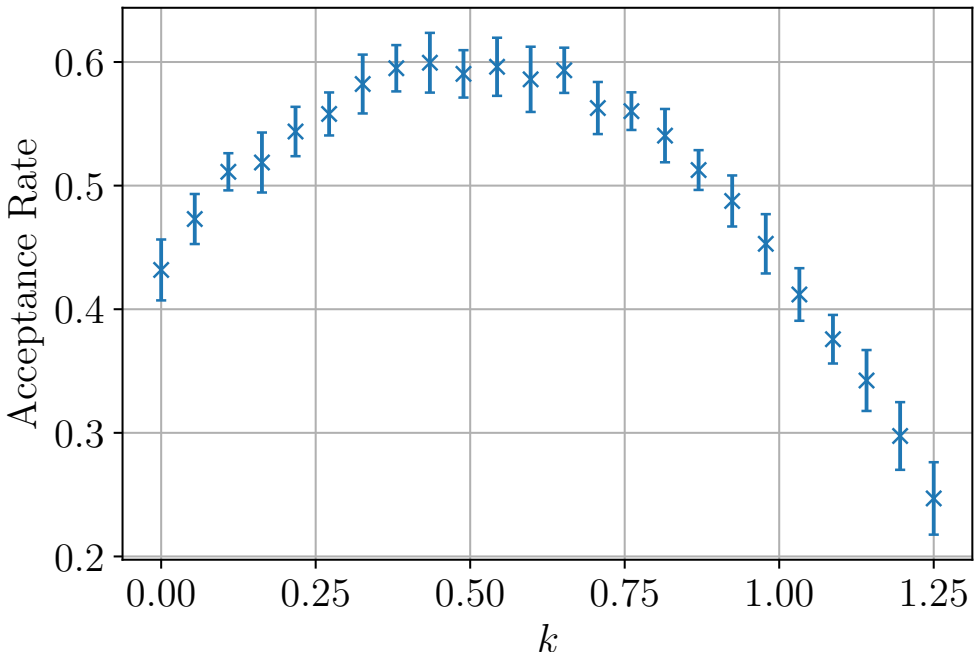


Figure 4.4: Showing the effect of the power of the eigenvalue on the acceptance rate, where not using the eigenvalue at all has an acceptance probability of $\approx 0.3$

This method of performing the updates has a number of advantages. Firstly, the proposals naturally scale with the curvature of the manifold meaning larger steps can be taken in each direction. The lack of need to transport vectors from the thimble manifold to the real manifold means that the inverse of the Jacobian does not need to be calculated, saving an $\mathcal{O}(N^3)$ operation, and once found the determinant of $J$ can be found quickly through the product of the eigenvalue. However, the computational cost of calculating the eigenvalue and eigenvectors of the Jacobian are not trivial. Using an implementation of the QR algorithm, an iterative $\mathcal{O}(n^2)$ solver that calculates the eigenpairs, the relationship between the number of iterations and the improvement in the convergence was investigated at $\tau = 1$, with 112 lattice sites. Unfortunately, as can be seen in Figure 4.5 while the technique improves the acceptance probability for a range of step sizes, $\delta$, the increase in wall clock time does not justify its use here. This 'saturation' is reached unfortunately early compared to not using the method at all. In previous chapters, values for $\delta$ as high as 0.25 were used, and this 20% increase does not justify the additional computational cost. Note that as shown in Figures 4.5e and 4.5f the wall clock time of each pass of the QR algorithm decreases, a

known quirk of algorithm, as the matrices involved internally become increasingly sparse, which has the counter-intuitive effect of an increase in marginal utility for a middle range of passes of the QR algorithm. The scaling of the QR algorithm being less than the inversion of the Jacobian means as the simulations have more lattice sites it will eventually supersede the techniques used here. It is also implied that the technique may be more viable at higher flow times, as shown by comparing Figures the left and right hand columns of Figure 4.5, where the latter is performed at $\tau = 1.5$, as the proposal technique is more sensitive to the topology. However, there is insufficient data here to make a concrete statement on this.

Even using the eigenvalue technique, a 'sweep' style update was used. However, there is no reason that an equivalent of a single site update technique could not be applied, by choosing a specific eigenvector's weights to be updated, rather than all at once. In principle this could incorporate the best aspects of both methods, as this the system is already decomposed in a logical manner for single parameter update, and could be an avenue of optimisations that was not considered here.

A further complication which occurs more frequently for $1+1D$ systems than the $0+1D$ systems that have mostly been considered elsewhere in this thesis is the problem of numerical overflow. As the flow time increases the numerical value of the field values at the lattice sites will typically increase, as will the values of the elements of the Jacobian. Particularly notable for this is the calculation of the action, which by construction will increase monotonically with the flow time. As the number of lattice sites to be considered increases, the likelihood of an overflow in the action or Jacobian determinant particularly, increases enormously. This functionally leads to either a practical limitation on the flow time, which as discussed in Section 4.1 will catastrophically impact on the ability of the thimble to minimise the error, or the use of high precision variables from a numerical library. An attempt was briefly made to use such high precision variables, provided by the Boost C++ library, but resulted in nearly a $50\times$ increase in wall clock time used per MC update, and was rejected. However, the reduction in flow time could still yield productive results. The necessity of using such a low flow time would mean

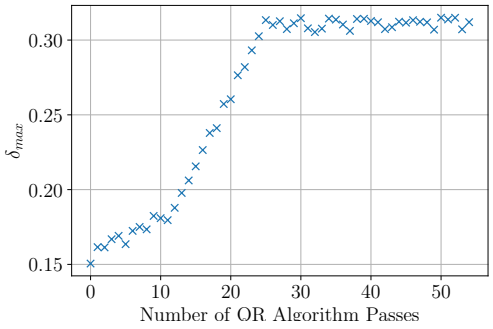


(a) How the maximum effective $\delta$ changes with the number of QR passes. $\tau = 1$.

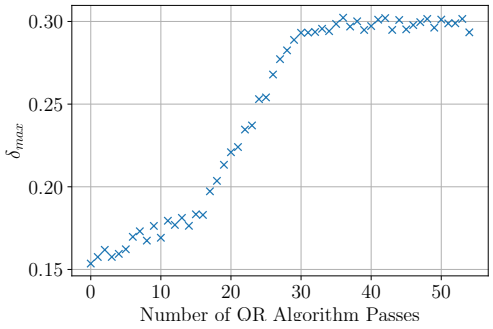


(b) How the maximum effective $\delta$ changes with the number of QR passes. $\tau = 1.5$.

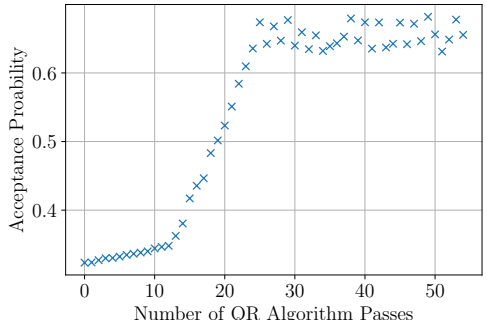


(c) How the acceptance probability for $\delta_{max}$ scales with the number of QR passes. $\tau = 1$.

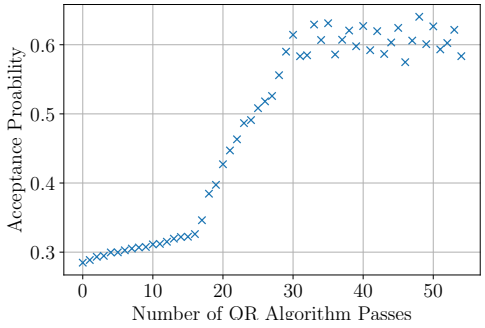


(d) How the acceptance probability for $\delta_{max}$ scales with the number of QR passes. $\tau = 1.5$.

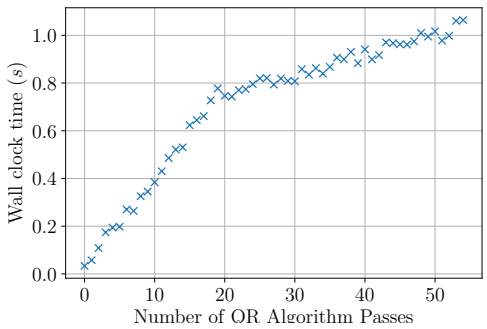


(e) Impact of QR number on the wall clock time required to perform an MC update for $\tau = 1$.

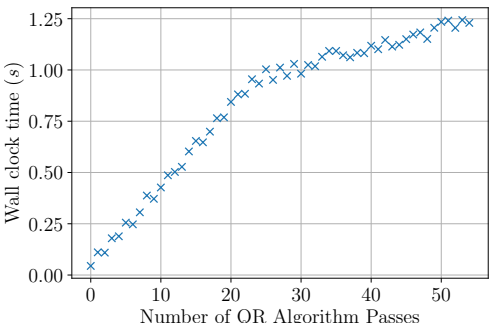


(f) Impact of QR number on the wall clock time required to perform an MC update for $\tau = 1.5$.

Figure 4.5: Impact of precision on the calculation of the Jacobian's eigenvalues, and how this impacts on step size and wall clock time. LHS corresponds to $\tau = 1$, RHS $\tau = 1.5$.

that using a $J_0$ or infrequently updated Jacobian might be more viable than it would be otherwise. Such techniques were discussed in Chapter 2.

## 4.3 An interacting two-field system

By introducing a second field to the simulations in 0+1D, the computational and initial condition complexity of the lattice could be increased without exceeding reasonable computational resources as this represents a factor of 2 increase in $N$, the number of equations to be solved for the flow and the dimension of the Jacobian, and still providing interesting new physical results. This second field exists on the same lattice as the original field, and for the example presented here is implemented through the action

$$\begin{aligned}\mathcal{I} = \left(\frac{-i}{\hbar}\right)\Bigg\{ & \frac{2\phi_1\tilde{\phi}_2^{cl}}{\mathrm{d}t} - \frac{\phi_2\tilde{\phi}_1^{cl}}{\mathrm{d}t} + \frac{\phi_{2m-2}\tilde{\phi}_1^{cl}}{\mathrm{d}t} + \frac{2\chi_1\tilde{\chi}_2^{cl}}{\mathrm{d}t} - \frac{\chi_2\tilde{\chi}_1^{cl}}{\mathrm{d}t} + \frac{\chi_{2m-2}\tilde{\chi}_1^{cl}}{\mathrm{d}t} \\ & + \sum_{i=1}^{2m-2}\Bigg[\frac{(\phi_{i+1}-\phi_i)^2}{2\Delta_i} + \frac{(\chi_{i+1}-\chi_i)^2}{2\Delta_i} \\ & - \left(\frac{\Delta_i+\Delta_{i+1}}{2}\right)\left(\frac{1}{2}m_\phi^2\phi_i^2 + \frac{1}{2}m_\chi^2\chi_i^2 + \frac{\lambda_1}{4}\phi_i\chi_i + \frac{\lambda_2}{4}\phi_i^2\chi_i^2\right)\Bigg]\Bigg\},\end{aligned} \tag{4.5}$$

where $\chi$ represents the second field. Note that this includes a bilinear mass mixing term parameterized by $\lambda_1$ and a quartic interaction parameterized by $\lambda_2$. As a result, setting $\lambda_1 = \lambda_2 = 0$ leads to recovering two decoupled free systems, two copies of the system studied previously. When $\lambda_1 \neq 0$, the system is still free, but $\phi$ and $\chi$ are no longer mass eigenstates, and oscillation between the two states is expected. When $\lambda_2 \neq 0$, actual interactions can be expected, decay and scattering between the two, depending on parameter values and the initial conditions.

The focus in this chapter will be on the case when $\chi$ is the heavier field, and initially occupied, and the $\phi$ is the lighter field and initially in vacuum. Concretely, $n_p = 0$ is taken for $\phi$ and $n_p = 1$ for $\chi$, $m_\phi = 1$ and $m_\chi = 2$. Considering first $\lambda_1 = \lambda_2 = 0$, and the free correlators in Figure 4.6. As the system is really two-

variable quantum mechanics, we can in fact solve the system semi-analytically using the method described in section 4.4, and use this for comparison. All thimble results below were generated with 400 chains of length $2 \times 10^6$, with $\tau = 1.5$, $\mathrm{d}t = 0.5$ and $\delta = 0.27$.

It is reasonable at this point to ask if a new problem has quietly appeared, that of multiple critical points, corresponding to multiple paths of steepest descent in the generalised manifold. In Chapter 3, it was shown that for each $(\phi_0, \phi_1)$ pair there was exactly one critical point. Is this still true, when multiple fields exist on the same lattice? In addition to (3.20) - (3.22), a second set of three equations now involved, of the same form as (3.20) - (3.22) with $\phi_i^{cl,q} \to \chi_i^{cl,q}$. $E_i$ is now a function of both fields. (3.22) with $\chi$ guarantees that $\chi_{m-1}^q = 0$ as for $\phi$. This ensures that $\partial E_i/\partial \phi_i^{cl} = \partial E_i/\partial \chi_i^{cl} = 0$, for the same reasons as previously. Given this, the same inductive process may be performed for both fields at the same time, showing that $(\phi_i^q, \chi_i^q) = 0$ for all $i$, and that all $(\phi_i^{cl}, \chi_i^{cl})$ are still uniquely defined by the initial conditions, although now those conditions are given by $(\phi_0, \phi_1, \chi_0, \chi_1)$, rather than by $\phi$ alone, and as a result there is only a single critical point. This technique can be applied in general for any number of scalar fields.

## 4.4 Semi-Analytic Quantum Mechanical Verification

It is possible to solve for the time evolution of the propagator directly in quantum mechanics, by defining the free Hamiltonians

$$H_\phi = \frac{p_\phi^2}{2} + \frac{\omega_\phi^2 \phi^2}{2}, \qquad H_\chi = \frac{p_\chi^2}{2} + \frac{\omega_\chi^2 \chi^2}{2}, \tag{4.6}$$

and setting up operators in the energy-eigenbasis of each of these harmonic oscillator systems, enumerated by $n$ and defined in terms of creation and annihilation

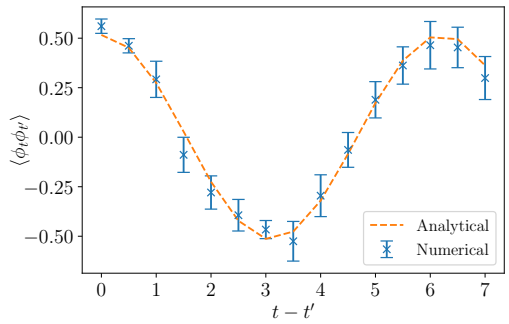


(a) Free field $\langle\phi\phi\rangle$ un-equal time correlator

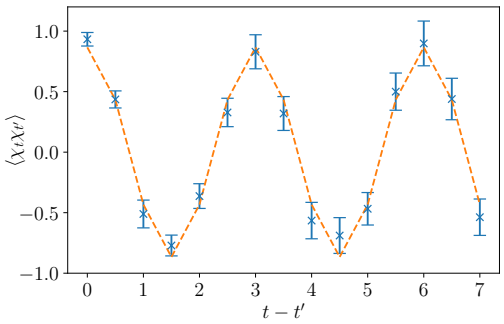


(b) Free field $\langle\chi\chi\rangle$ un-equal time correlator

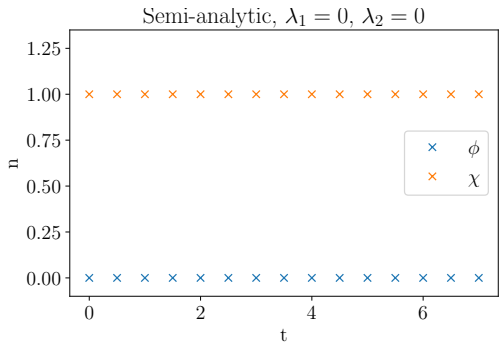


(c) Free field $\phi$ and $\chi$ occupation numbers, analytic computation.

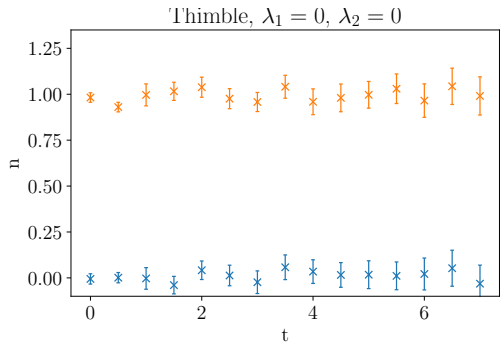


(d) Free field $\phi$ and $\chi$ occupation numbers, Thimble computation.

Figure 4.6: The un-equal time correlator (top) and occupation number (bottom) for two free fields, comparing semi-analytic results to Thimble results.

operators as

$$a^\dagger |n\rangle = \sqrt{n+1}\,|n+1\rangle\,, \quad a\,|n\rangle = \sqrt{n}\,|n-1\rangle \tag{4.7}$$

In this work it was found that a sufficiently good numerical result was obtained by restricting the system to the lowest $N = 30$ eigenstates (900 product eigenstates). In this basis, the Hamiltonian for each free system is then (one for $\phi$, one for $\chi$)

$$H = \hbar\omega \times \mathrm{diag}(n + 1/2), \tag{4.8}$$

while the "coordinate" operator (often denoted $q$ in QM, in the present context corresponding to $\phi$ and $\chi$), is

$$q = \sqrt{\frac{\hbar}{2\omega}}(a^\dagger + a) = \sqrt{\frac{\hbar}{2\omega}} \begin{pmatrix} 0 & \sqrt{1} & & & \\ \sqrt{1} & 0 & \sqrt{2} & & \\ & \sqrt{2} & 0 & \ddots & \\ & & \ddots & \ddots & \sqrt{N-1} \\ & & & \sqrt{N-1} & 0 \end{pmatrix}, \tag{4.9}$$

and similarly for the canonical momenta ($p_\phi$, $p_\chi$)

$$p = i\sqrt{\frac{\hbar\omega}{2}}(a^\dagger - a). \tag{4.10}$$

Including interactions, the combined Hamiltonian on the product space is

$$H = H_\phi \otimes \mathbb{I} + \mathbb{I} \otimes H_\chi + \frac{\lambda_1}{4}\phi \otimes \chi + \frac{\lambda_2}{4}\phi^2 \otimes \chi^2, \tag{4.11}$$

Given some operator $O(t)$ and some initial density matrix $\rho$, the observables may then be computed by direct insertion into the expression

$$\langle O(t)\rangle = \mathrm{Tr}\left[e^{iHt}\rho e^{-iHt}O\right]. \tag{4.12}$$

For $N = 30$, the Hamiltonian may be straightforwardly diagonalised numerically, giving the energy eigenvalues of the system as the diagonal matrix $\Lambda$. The change of basis matrices $U$, $H = U\Lambda U^\dagger$ are also set. This allows for exponentiation into

the evolution matrix $e^{iHt} = Ue^{i\Lambda t}U^\dagger$, which may then be inserted into (4.12), allowing us to carry out the trace.

The same observables are computed as in the Thimble calculation

$$O = \phi^2 \otimes \mathbb{I},\ p_\phi^2 \otimes \mathbb{I},\ \mathbb{I} \otimes \chi^2,\ \mathbb{I} \otimes p_\chi^2, \tag{4.13}$$

and extract the occupation number from this through the use of (4.18), for the same values of $t$ as the discretized Thimble lattice.

For consistency with the thimble computations in the main work, one field must be chosen ($\chi$, the heavier one) to initially be in an excited (thermal) state, and the other ($\phi$, the lighter one) to begin in the ground state. Beginning by writing

$$\rho = \rho_\phi \otimes \rho_\chi, \tag{4.14}$$

where $\rho_\phi$ and $\rho_\chi$ are the equilibrium density matrices for occupations numbers of 0 and $n = 1$ respectively, given by

$$\rho_\phi = \begin{pmatrix} 1 & 0 & \cdots & 0 \\ 0 & 0 & \cdots & 0 \\ \vdots & & & \vdots \\ 0 & 0 & \cdots & 0 \end{pmatrix}, \tag{4.15}$$

and

$$\rho_\chi = 2\sinh(\hbar\omega\beta/2) \begin{pmatrix} e^{-\hbar\omega\beta/2} & & & \\ & e^{-\hbar\omega\beta(1+1/2)} & & \\ & & \ddots & \\ & & & e^{-\hbar\omega\beta(N+1/2)} \end{pmatrix}, \tag{4.16}$$

where

$$\beta = \frac{1}{\hbar\omega} \ln\left(\frac{1}{n} + 1\right). \tag{4.17}$$

For quantum mechanics this method is of course vastly more efficient than applying the Generalised Thimble.

### 4.4.1 Mass mixing and field oscillations

It may be useful to introduce representation of the time-dependent occupation number operator, extracted from the equal-time correlators

$$\langle n_{\phi\, i} \rangle = \frac{1}{\hbar} \left( \sqrt{\langle \phi_i \phi_i \rangle \left\langle \dot{\phi}_i \dot{\phi}_i \right\rangle} - \frac{1}{2} \right), \tag{4.18}$$

This will now be computed for a number of different values of $\lambda_1$, still keeping $\lambda_2 = 0$. This is shown in Figure 4.7, and we see that the Thimble method provides a very good qualitative and quantitative match to the semi-analytic computation.

### 4.4.2 Interactions and particle exchange

The mass mixing was then turned off by setting $\lambda_1 = 0$, and instead quadratic interactions were enabled by setting $\lambda_2 \neq 0$. Similarly to the previous case the system is set up with a non zero occupation number in the $\chi$ field, and vacuum in the $\phi$ field. The $\chi$ is heavy and the $\phi$ is light, $m_\chi/m_\phi = 2$. Figure 4.8 shows again the evolution in time, but now including quartic interactions. It can be seen that instead of oscillations, the $\chi$ "particles" are slowly leaking into $\phi$ particles. This is a truly non-equilibrium, non-perturbative computation, captured within what is admittedly a quite small physical time interval. Clearly, for this quantum mechanical system, it is vastly more efficient to simply solve it using the semi-analytic method. But it can be seen that with moderate numerical effort, the Thimble approach provides accuracy good enough to distinguish a gradual exchange of particles between $\phi$ and $\chi$.

## 4.5 Conclusions

Using the technique developed in [49], it has been demonstrated that multiple fields can be simulated fully non-perturbatively in real-time, for time-scales where interesting real-time physics may begin to be explored. In the particular system

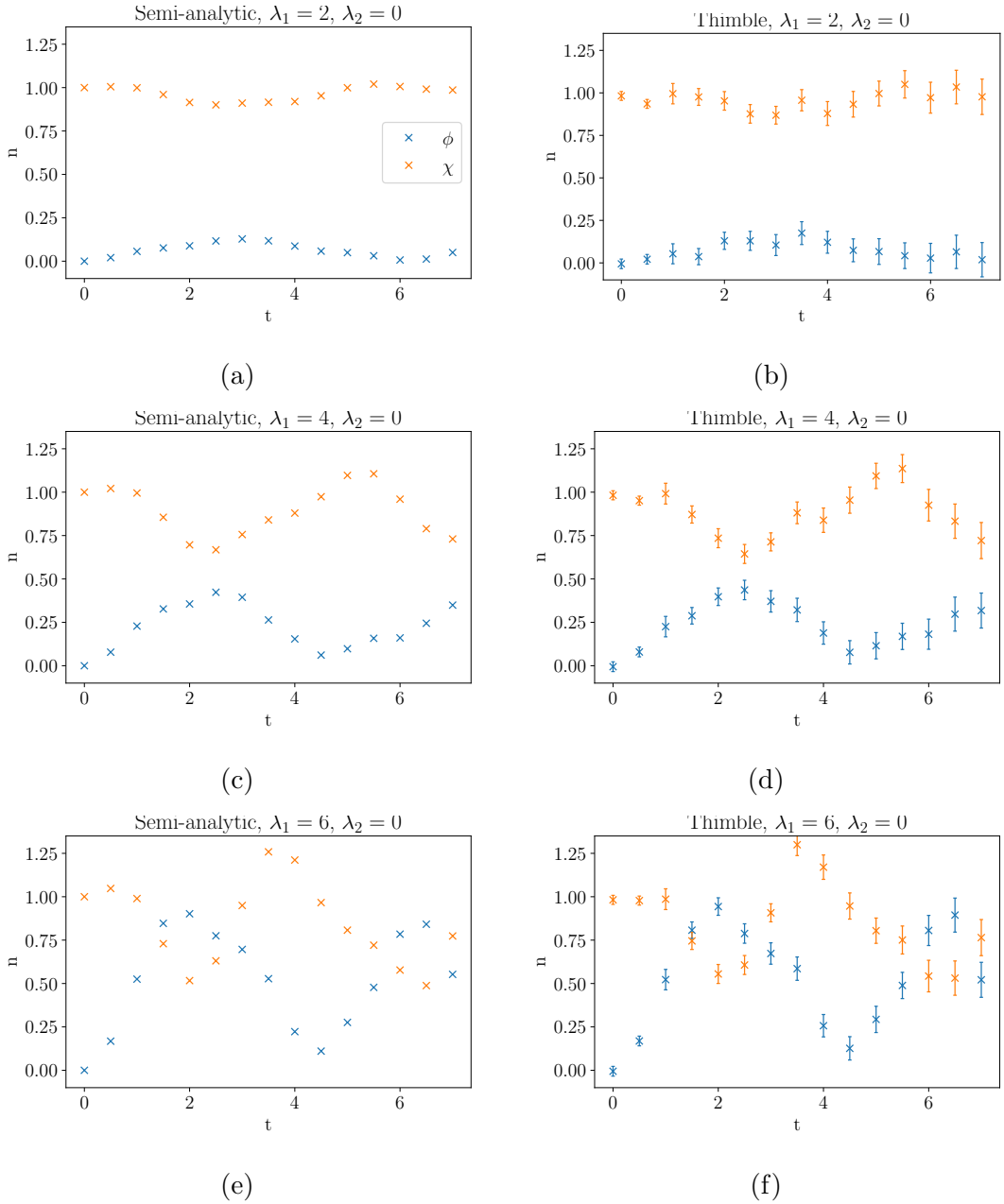


Figure 4.7: Semi-analytic (left) and Thimble (right) occupation numbers for two fields mixing with different values of the parameter $\lambda_1$, $\lambda_2 = 0$.

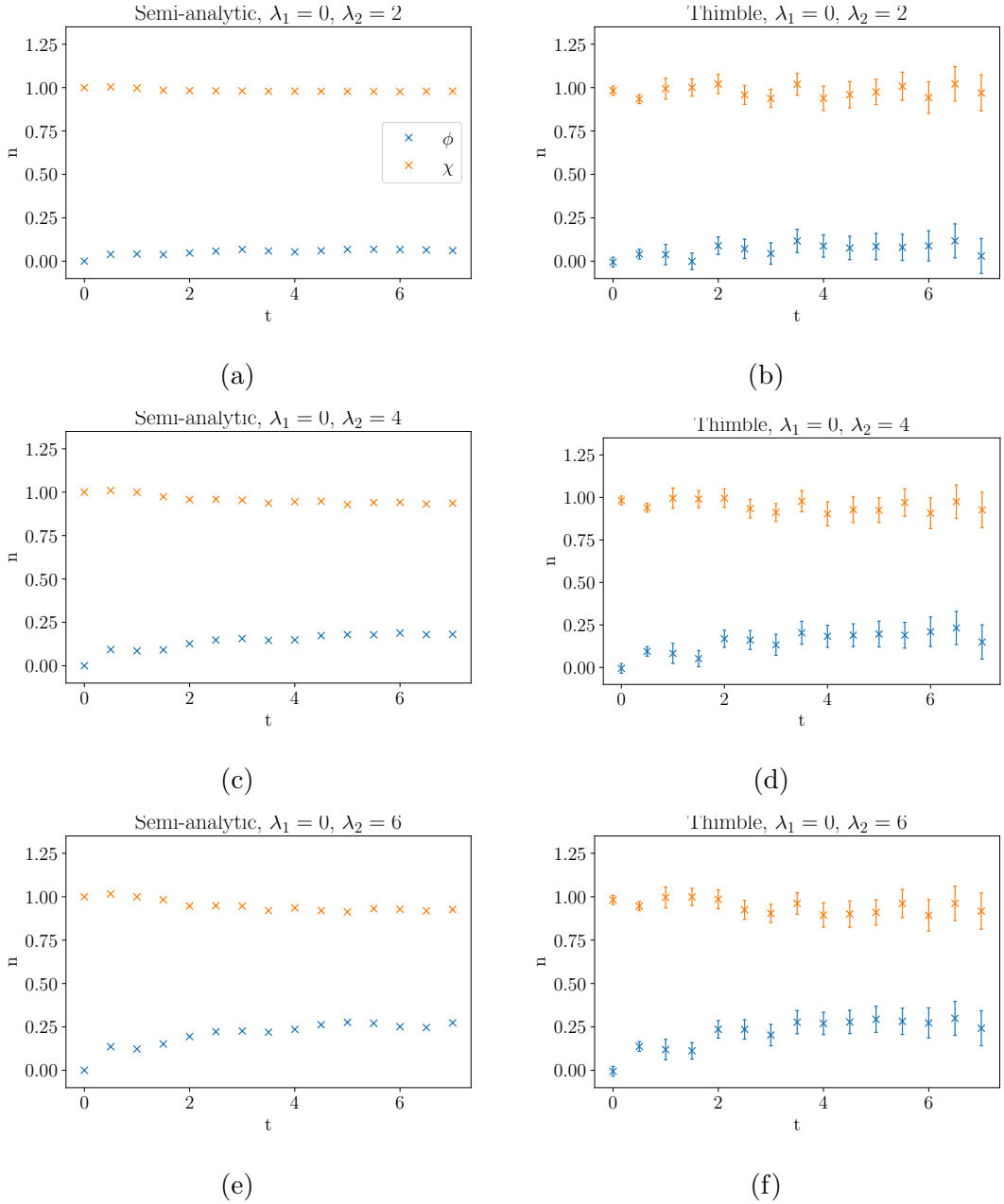


Figure 4.8: Semi-analytic (left) and Thimble (right) occupation numbers for two fields interacting with different values of the parameter $\lambda_2$, $\lambda_1 = 0$.

considered here, the fields were made to interact through mass mixing as well as through a 4-point interaction allowing for exchange of particles. By comparing to a standard semi-analytic computation in quantum mechanics, this is a further demonstration that real-time Generalised Thimble methods, as introduced in [49], give correct and accurate results. This strong statement can be backed by comparison with the semi-analytic quantum mechanical results.

It is however clear that in order to improve the computational viability of this new technique for full field theory at long physical times, the parameters controlling the numerical implementation must be optimised for minimal statistical error. These are critical as the system scales in complexity, but also due to the increasing number of independent chains required to probe the initial condition parameter space as the number of fields and the number of dimensions increases. By ensuring that the optimal simulation parameters are used the simulation time can be improved by a factor of 5 compared to previous attempts. Despite this, large scale multi-field $3+1$ dimensional simulations are probably out of reach for present computing power using this technique in its present form. As an example, consider a small classical-statistical real-time simulation in 3+1 D, which would typically involved $32^3$ spatial sites, $dt = 0.05$ with a mass of $am = 0.5$, running until a physical time of order $mt = 100$. That is an eye-watering $40 \times 100 \times 32^3 \times 2 = 262$ million variables, doubled for the two Keldysh branches. In the present simulations, up to 30 were considered. Even when straining the simulations in just 1+1D, using perhaps $dt = 0.1$, $am = 1$, $N_x = 16$ simulating to $mt = 25$, this is still $250 \times 16 \times 2 = 8000$ variables. Inversion of this size matrices is possible, but generating sufficiently long MC chains remains a challenge.

The MC chains/initial conditions may be trivially parallelised. The issue, as for standard MC simulations in four Euclidean dimensions, is the computation and inversion of large matrices, in this case the Jacobian $J$. Dealing with large (sparse) matrices is a well-known problem in that field, and optimised algorithms exist. Using GPU processors rather than CPU's would be a way to go. As mentioned above, even at the fairly small systems considered here, up to 95% of

the runtime is spent dealing with the Jacobian. Since that scales as the number of variables squared (or even cubed), it will be the vastly dominant bottleneck for large systems.

Hence, the proposal that was reached is for further work be done improving parallelisation within each chain, and the use of optimised algorithms for standard mathematical tasks. There are two good candidates for this effort, the implementations of (1.35) and (1.55) which generate $Nm + (Nm)^2$ coupled complex equations for $N$ fields and $m$ total dynamical lattice sites, and the solution of the matrix equation in step (3) of Section 2.1. This would make larger flow times or longer Markov chain lengths viable, improving accuracy in combination with increasing the number of chains/initial conditions. In turn, this could allow for effective simulations of multi-field models in higher dimensions, for longer physical times.

# Chapter 5

# Conclusions

The Generalised Thimble techniques presented here have shown that it is possible to have non-perturbative, non-equilibrium simulations of quantum fields on a lattice. In principle the energy of these interactions could be increased as high as are needed to simulate physics of interest. These techniques do not present an approximation of the solution, as prior attempts to tame the sign problem have, but a true representation of the underlying physics exactly as set in the Lagrangian thanks to the exact nature of using a generalised thimble as discussed in Chapters 1.1 and 3. Despite the exact nature of the mathematical technique, the simulations here are still produced using MCMC techniques, which introduces numerical error. However these results are always within reasonable error of literature or analytic verification results. Simultaneously Chapter 4 shows both a demonstration of multiple field simulations occurring with coupling strengths well beyond the perturbative regime, set to initial conditions that are out of equilibrium.

The work presented here has established that multiple fields can co-exist on the same lattice, and by using the new sampling method presented in Chapter 3, can be set in different initial configurations. Other authors have shown that the equilibrium techniques that have been expanded here work in $1+1D$ and even $2+1D$. There is no theoretical reason that these cannot be scaled further to $3+1D$, and

no aspect of their analysis is incompatible with the implementation of the density matrix as described here. Combining these opens the door to a wide variety of applications, where in principle any number of fields can be simulated in high fidelity, and their initial configurations tuned by changing the distribution in (3.46).

This is demonstrated tangibly by the simulations discussed in Chapter 4, where two fields in self equilibrium suddenly have an interaction turned on between them, allowing the heavier 'particle' species to decay into its lighter counterpart. This simulation was repeated with a range of coupling strengths which push it well beyond simple perturbative techniques and open new avenues of research. This combined with the optimisations presented in the same chapter show that multi-field simulations in $0 + 1D$ can be made to be viable even with limited hardware.

At the same time the difficulties in scaling such simulations up were discussed. This project was poised to take a different direction, into higher dimensional simulations rather than multiple fields, but the computational difficulties that this presented forced a change in course. However, the difficulties go beyond just increasing the number of lattice sites, practical solutions to the problem of the acceptance rate must be found if the number of lattice sites in these simulations continues to climb.

It is difficult to overstate the importance of the development of the decoupling of the initial conditions from the lattice as described in Chapter 3. Formerly, it would have been possible but pointless to perform simulations with two fields in the style presented in Chapter 4, as both fields would have to be at the same temperature as it is defined by the lattice, not by the field. The results in Chapter 4 further reinforce how useful this technique is. $0 + 1D$ simulations are ideal for testing techniques such as the Generalised Thimble in new situations, as it can easily be verified by well established quantum mechanical results. Here, the comparison between the traditional and new techniques show that they match remarkably well. This disconnection between the lattice and the initial conditions

is a wellspring for new simulations of fields that begin out of equilibrium which we have not yet begun to explore.

The technique is not however without its limits. The high energy interactions that are allowed by the technique being non-perturbative introduce problems of their own. As the energy of the interactions grows, the lattice link size must shrink to ensure that the details are captured. A necessary consequence of this is that it will require increasing numbers of lattice sites to cover the same spacial and temporal extent, as discussed in Chapter 2, the evaluation time of an MCMC step scales as $\mathcal{O}(N_{sites}^3)$, meaning that even a small decrease in the link size will have an enormous effect on the evaluation time. A further problem manifests in the flow process itself, as the link size decreases and coupling strengths increase the lattice action and its derivative $\partial\mathcal{I}/\partial\phi$ grow enormously. This causes issues for the numerical evaluation of (1.35) at large values of $\tau$, practically restricting how high $\tau_{max}$ can be set. As shown in Chapter 4, the flow time is the single easiest parameter to increase to make solution feasible, and by reducing it other parameters such as the chain length must be increased instead by roughly the factor by which the flow time has been decreased. This can therefore cause the program runtime to grow massively out of control.

The simulations in Chapters 3 and 4 benefit enormously from the fact there existed only one critical point, as proven for both cases in the relevant chapters. The existence of a single critical point guarantees that the full Picard-Lefshetz thimble cannot be composed of more than one path of steepest descent. Consequently, there cannot be any issue with increasing the flow time as was found in [104], where due to the fact the thimble was composed of multiple paths the generalised thimble with a finite flow time could never capture the asymptotic behaviour of the connection, resulting in a large potential barrier along the thimble. This lead to issues with the MCMC simulation, severely impacting on the chain length required to accurately probe the thimble. Furthermore, such potential barriers become harder (rather than easier, as one might intuitively expect) to probe as the flow increases, meaning that contrary to the results presented in

Chapter 4 increasing the flow time can worsen convergence time. This is something to bear in mind if the system to be simulated does not share the properties of the systems used here.

As discussed in this section increasing the lattice dimensions to $3+1D$ would require increasing the number of lattice sites by at least two orders of magnitude, and correspondingly increase the runtime by a factor of $10^6$. It is important to reiterate that the work referenced in relation to increasing the dimentionality is practically only currently possible due to the fact that these are equilibrium simulations, and therefore it is not required to explore the density matrix parameter space as it is integrated with the lattice as described in Chapter 1.1, a benefit that the non-equilibrium technique does not have.

These issues, the factor for $10^6$ for 'real dimensions' simulations in particular, could be seen as hard limits to the technique. However relief for this may yet be possible. As discussed in Chapter 2, techniques that minimise the computation of the Jacobian, such as assuming that the matrix evolves slowly compared to the fields, could enormously improve computational performance especially as this decreases the dependence on the calculating the Jacobian, its inverse, and its determinant. This correspondingly decreases the impact that the number of lattice sites has on the runtime from scaling with $N_{sites}^3$ to a linear dependence, for sufficiently infrequent Jacobian updates. The use of computationally efficient high precision variables could alleviate the issues with the max flow time, allowing simulations to be run with considerably higher efficiency, and decrease the impact of lowering the link size.

Other techniques beyond those of optimising the process that could improve the computational efficiency of this technique include the use of machine learning to provide the update proposals [158, 159, 160, 161, 162]. A number of papers have found that it is possible to train a neural network to accurately probe highly distorted probability distributions, of the type encountered when trying to draw isotropic proposals on the manifold. Optimisations of this type could significantly

shorten the chain length required to converge to a result. Radically, other approaches could even use machine learning to move away from MCMC techniques completely [163].

Recent advancements in programming on graphical processing units, GPUs (as opposed to conventional, computational processing units, CPUs) might also yield results in this regard. Compared to CPUs, GPUs typically have thousands of lower speed processing cores, allowing for efficient parallelisation. For a brief comparison, a current generation consumer GPU (NVIDIA 3080Ti) with the DiRAC DIaL3 supercomputer on which approximately half of the calculations in this thesis were run, generally using 256 cores, is included in Table 5.1. As this project is highly paralellisable, either at the scale of an MCMC chain, matrix operations, or at the scale of the ODE solver, the core speed statistic can be used to directly convert between core number and runtime. As a result, a single consumer grade GPU is approximately 20% as useful for these calculations as the entire DIaL3 supercomputer.

| | DIaL3 | NVIDIA 3080Ti |
|---|---|---|
| Core Number | 25,600 | 10,240 |
| Core Speed (GHz) | 3.4 | 1.67 |
| Memory (GB) | 512 | 12 |

Table 5.1: Showing a brief comparison of the computational capacity of a supercomputer and a GPU.

GPUs are particularly adept at performing small, linked tasks. Traditionally this has lead to a large number of linear algebra uses [164, 165, 166, 167, 168]. However, more recently attempts have been made to effectively solve systems of coupled ODEs on GPUs [169, 170]. Combining this work with these techniques could open the door to much larger lattices in higher dimentions.

There are caveats to this. Firstly programming on GPUs has more pitfalls than programming on CPUs as the technology to do this beyond graphical engines is considerably newer, and consequently code cannot be simply ported between the

two environments. The reduction in the ratio of memory to the number of cores presents significant programming obstacles too, but not ones that cannot be overcome. As discussed above, it is possible to parallelize within each chain, using the high number of processors to multi-thread matrix operations while keeping the total number of chains reasonable [171]. Some combination of these approaches are likely to yield productive developments in simulations using these techniques in the near future.

# Bibliography


[1] A. Alexandru, G. Başar, P.F. Bedaque, S. Vartak and N.C. Warrington, *Monte carlo study of real time dynamics on the lattice*, *Physical review letters* **117** (2016) 081602.

[2] A. Alexandru, G. Başar, P.F. Bedaque and G. Ridgway, *Schwinger-keldysh formalism on the lattice: A faster algorithm and its application to field theory*, *Physical Review D* **95** (2017) 114501.

[3] G. Aarts and J. Smit, *Classical approximation for time-dependent quantum field theory: Diagrammatic analysis for hot scalar fields*, *Nuclear Physics B* **511** (1998) 451.

[4] D. Scott and A. Moss, *Matter temperature during cosmological recombination*, *Monthly Notices of the Royal Astronomical Society* **397** (2009) 445.

[5] P. Peebles, *Recombination of the primeval plasma*, *The Astrophysical Journal* **153** (1968) 1.

[6] J. Chluba, *Could the cosmological recombination spectrum help us understand annihilating dark matter?*, *Monthly Notices of the Royal Astronomical Society* **402** (2010) 1195.

[7] S. Kempe and J. Kazmierczak, *Biogenesis and early life on earth and europa: favored by an alkaline ocean?*, *Astrobiology* **2** (2002) 123.

[8] S. Bruggisser, B. Von Harling, O. Matsedonskyi and G. Servant, *Baryon asymmetry from a composite higgs boson*, *Physical review letters* **121** (2018) 131801.

[9] M.M. Anber and E. Sabancilar, *Hypermagnetic fields and baryon asymmetry from pseudoscalar inflation*, *Physical Review D* **92** (2015) 101501.

[10] D. Gorbunov and A. Panin, *Scalaron the mighty: producing dark matter and baryon asymmetry at reheating*, *Physics Letters B* **700** (2011) 157.

[11] Y. Hamada and S. Iso, *Baryon asymmetry from primordial black holes*, *Progress of Theoretical and Experimental Physics* **2017** (2017) .

[12] M.S. Longair, *Galaxy formation*, Springer Science & Business Media (2007).

[13] T. Padmanabhan, *Structure formation in the universe*, Cambridge university press (1993).

[14] M. Tanabashi, K. Hagiwara, K. Hikasa, K. Nakamura, Y. Sumino, F. Takahashi et al., *Review of particle physics*, *Physical Review D* **98** (2018) 030001.

[15] D.E. Morrissey and M.J. Ramsey-Musolf, *Electroweak baryogenesis*, *New Journal of Physics* **14** (2012) 125003.

[16] T. Asaka and M. Shaposhnikov, *The $\nu$msm, dark matter and baryon asymmetry of the universe*, *Physics Letters B* **620** (2005) 17.

[17] T. Fujita and K. Kamada, *Large-scale magnetic fields can explain the baryon asymmetry of the universe*, *Physical Review D* **93** (2016) 083520.

[18] N. DePorzio, W.L. Xu, J.B. Muñoz and C. Dvorkin, *Finding ev-scale light relics with cosmological observables*, *Physical Review D* **103** (2021) 023504.

[19] K. Abazajian, G.M. Fuller and W.H. Tucker, *Direct detection of warm dark matter in the x-ray*, *The Astrophysical Journal* **562** (2001) 593.

[20] J.L. Feng, *Dark matter candidates from particle physics and methods of detection*, *Annual Review of Astronomy and Astrophysics* **48** (2010) 495.

[21] R. Haggar, F.R. Pearce, M.E. Gray, A. Knebe and G. Yepes, *The three hundred project: Substructure in hydrodynamical and dark matter simulations of galaxy groups around clusters*, *Monthly Notices of the Royal Astronomical Society* **502** (2021) 1191.

[22] A. Knebe, M. Gámez-Marín, F.R. Pearce, W. Cui, K. Hoffmann, M. De Petris et al., *The three hundred project: shapes and radial alignment of satellite, infalling, and backsplash galaxies*, *Monthly Notices of the Royal Astronomical Society* **495** (2020) 3002.

[23] D.H. Weinberg, J.S. Bullock, F. Governato, R. Kuzio de Naray and A.H. Peter, *Cold dark matter: controversies on small scales*, *Proceedings of the National Academy of Sciences* **112** (2015) 12249.

[24] E.S. Tyler, *Constraints on primordial black hole dark matter from wide binaries in the galactic halo*, Ph.D. thesis, University of Nottingham, 2022.

[25] E. Tyler, A.M. Green and S.P. Goodwin, *Uncertainties in wide binary constraints on primordial black holes*, *arXiv preprint arXiv:2207.08668* (2022) .

[26] M. Gorton and A.M. Green, *Effect of clustering on primordial black hole microlensing constraints*, *arXiv preprint arXiv:2203.04209* (2022) .

[27] P. Peebles and A. Vilenkin, *Noninteracting dark matter*, *Physical Review D* **60** (1999) 103506.

[28] E. Corbelli, *Dark matter and visible baryons in m33*, *Monthly Notices of the Royal Astronomical Society* **342** (2003) 199.

[29] G. Stefanucci and R. Van Leeuwen, *Nonequilibrium many-body theory of quantum systems: a modern introduction*, Cambridge University Press (2013).

[30] J. Berges, *Introduction to nonequilibrium quantum field theory*, in *AIP Conference Proceedings*, vol. 739, pp. 3–62, American Institute of Physics, 2004.

[31] W.A. de Jong, K. Lee, J. Mulligan, M. Płoskoń, F. Ringer and X. Yao, *Quantum simulation of nonequilibrium dynamics and thermalization in the schwinger model*, *Physical Review D* **106** (2022) 054508.

[32] F.M. Surace et al., *Lattice gauge theories and constrained systems: from quantum simulation to non-equilibrium dynamics*, .

[33] P.F. Bedaque, *A complex path around the sign problem*, in *EPJ Web of Conferences*, vol. 175, p. 01020, EDP Sciences, 2018.

[34] S. Catterall, R. Galvez, A. Joseph and D. Mehta, *On the sign problem in 2d lattice super yang-mills*, *Journal of High Energy Physics* **2012** (2012) 1.

[35] M. Troyer and U.-J. Wiese, *Computational complexity and fundamental limitations to fermionic quantum monte carlo simulations*, *Physical review letters* **94** (2005) 170201.

[36] C. Mak and D. Chandler, *Solving the sign problem in quantum monte carlo dynamics*, *Physical Review A* **41** (1990) 5709.

[37] G. Aarts, E. Seiler, D. Sexty and I.-O. Stamatescu, *On complex langevin dynamics and zeroes of the measure i: Formal proof and simple models*, *arXiv preprint arXiv:1611.02930* (2016) .

[38] G. Aarts, E. Seiler, D. Sexty and I.-O. Stamatescu, *Complex langevin dynamics and zeroes of the fermion determinant*, *Journal of High Energy Physics* **2017, 5** (2017) 1.

[39] H. Aoki, N. Tsuji, M. Eckstein, M. Kollar, T. Oka and P. Werner, *Nonequilibrium dynamical mean-field theory and its applications*, *Reviews of Modern Physics* **86** (2014) 779.

[40] F. Bursa and M. Kroyter, *A simple approach towards the sign problem using path optimisation*, *Journal of High Energy Physics* **2018** (2018) 1.

[41] S. Woodward, P.M. Saffin, Z.-G. Mou and A. Tranberg, *Optimisation of thimble simulations and quantum dynamics of multiple fields in real time*, *arXiv preprint arXiv:2204.10101* (2022) .

[42] Z.-G. Mou, P.M. Saffin and A. Tranberg, *Quantum tunnelling, real-time dynamics and picard-lefschetz thimbles*, *Journal of High Energy Physics* **2019** (2019) 1.

[43] J.M. Pawlowski, M. Scherzer, C. Schmidt, F.P. Ziegler and F. Ziesché, *Simulating gauge theories on lefschetz thimbles*, *arXiv preprint arXiv:2001.09767* (2020) .

[44] M. Cristoforetti, F. Di Renzo, L. Scorzato, A. Collaboration et al., *New approach to the sign problem in quantum field theories: High density qcd on a lefschetz thimble*, *Physical Review D* **86** (2012) 074506.

[45] M. Cristoforetti, F. Di Renzo, A. Mukherjee and L. Scorzato, *Monte carlo simulations on the lefschetz thimble: Taming the sign problem*, *Physical Review D* **88** (2013) 051501.

[46] A. Mukherjee, M. Cristoforetti and L. Scorzato, *Metropolis monte carlo integration on the lefschetz thimble: Application to a one-plaquette model*, *Physical Review D* **88** (2013) 051502.

[47] A. Alexandru, G. Başar and P. Bedaque, *Monte carlo algorithm for simulating fermions on lefschetz thimbles*, *Physical Review D* **93** (2016) 014504.

[48] A. Alexandru, G. Basar, P.F. Bedaque, G.W. Ridgway and N.C. Warrington, *Sign problem and monte carlo calculations beyond lefschetz thimbles*, *Journal of High Energy Physics* **2016** (2016) 1.

[49] Z.-G. Mou, P.M. Saffin, A. Tranberg and S. Woodward, *Real-time quantum dynamics, path integrals and the method of thimbles*, *Journal of High Energy Physics* **2019** (2019) 1.

[50] P.M. Bakshi and K.T. Mahanthappa, *Expectation value formalism in quantum field theory. i*, *Journal of Mathematical Physics* **4** (1963) 1.

[51] D. Bahns, S. Doplicher, K. Fredenhagen and G. Piacitelli, *Ultraviolet finite quantum field theory on quantum spacetime*, *Communications in mathematical physics* **237** (2003) 221.

[52] C. Fronsdal and R.W. Huff, *Two-body problem in quantum field theory*, *Physical Review D* **3** (1971) 933.

[53] J.W. Jerome and E. Polizzi, *Discretization of time-dependent quantum systems: real-time propagation of the evolution operator*, *Applicable Analysis* **93** (2014) 2574.

[54] E. Schrödinger, *An undulatory theory of the mechanics of atoms and molecules*, *Physical review* **28** (1926) 1049.

[55] H. Haug, A.-P. Jauho et al., *Quantum kinetics in transport and optics of semiconductors*, vol. 2, Springer (2008).

[56] R. van Leeuwen, N.E. Dahlen, G. Stefanucci, C.-O. Almbladh and U. von Barth, *Introduction to the keldysh formalism and applications to time-dependent density-functional theory*, *arXiv preprint cond-mat/0506130* (2005) .

[57] U. Fano, *Description of states in quantum mechanics by density matrix and operator techniques*, *Reviews of modern physics* **29** (1957) 74.

[58] A.S. Holevo, *Statistical structure of quantum theory*, vol. 67, Springer Science & Business Media (2003).

[59] A. Peres, *Quantum theory: concepts and methods*, Springer (1997).

[60] B.C. Hall, *Systems and subsystems, multiple particles*, in *Quantum Theory for Mathematicians*, pp. 419–440, Springer (2013).

[61] P. Busch and P. Lahti, *Lüders rule*, in *Compendium of quantum physics*, pp. 356–358, Springer (2009).

[62] H.-P. Breuer, F. Petruccione et al., *The theory of open quantum systems*, Oxford University Press on Demand (2002).

[63] L.P. Kadanoff and G.A. Baym, *Quantum Statistical Mechanics Green's Function Methods in Equilibrium Problems*, Benjamin (1962).

[64] A. Kamenev, *Field theory of non-equilibrium systems*, Cambridge University Press (2023).

[65] T. Kita, *Introduction to nonequilibrium statistical mechanics with quantum field theory*, *Progress of theoretical physics* **123** (2010) 581.

[66] P. Millington, *Thermal quantum field theory and perturbative non-equilibrium dynamics*, Springer Science & Business Media (2013).

[67] C. Gattringer and K. Langfeld, *Approaches to the sign problem in lattice field theory*, *International Journal of Modern Physics A* **31** (2016) 1643007.

[68] T.A. Degrand and C. DeTar, *Lattice methods for quantum chromodynamics*, World Scientific (2006).

[69] I. Montvay and G. Münster, *Quantum fields on a lattice*, Cambridge University Press (1994).

[70] Z.-X. Li and H. Yao, *Sign-problem-free fermionic quantum monte carlo: Developments and applications*, *Annual Review of Condensed Matter Physics* **10** (2019) 337.

[71] K. Nagata, *Finite-density lattice qcd and sign problem: current status and open problems*, *Progress in Particle and Nuclear Physics* (2022) 103991.

[72] M. Ulybyshev, V. Dorozhinskii and O. Pavlovskii, *The use of neural networks to solve the sign problem in physical models*, *Physics of Particles and Nuclei* **51** (2020) 363.

[73] G. Aarts, C. Allton, S. Hands, B. Jäger, S. Kim, M. Lombardo et al., *Lattice qcd at nonzero temperature and density*, in *Journal of Physics: Conference Series*, vol. 2207, p. 012055, IOP Publishing, 2022.

[74] Y. Tanizaki and T. Koike, *Real-time feynman path integral with picard–lefschetz theory and its applications to quantum tunneling*, *Annals of Physics* **351** (2014) 250.

[75] Y. Tanizaki, *Lefschetz-thimble techniques for path integral of zero-dimensional o (n) sigma models*, *Physical Review D* **91** (2015) 036002.

[76] E. Witten, *A new look at the path integral of quantum mechanics*, *arXiv preprint arXiv:1009.6032* (2010) .

[77] A. Alexandru, G. Başar, P.F. Bedaque and N.C. Warrington, *Complex paths around the sign problem*, *Reviews of Modern Physics* **94** (2022) 015006.

[78] G. Fujisawa, J. Nishimura, K. Sakai and A. Yosprakob, *Backpropagating hybrid monte carlo algorithm for fast lefschetz thimble calculations*, *Journal of High Energy Physics* **2022** (2022) 1.

[79] T. Kanazawa and Y. Tanizaki, *Structure of lefschetz thimbles in simple fermionic systems*, *Journal of High Energy Physics* **2015** (2015) 1.

[80] Y. Tanizaki, *Study on sign problem via lefschetz-thimble path integral*, *The University of Tokyo, PhD thesis* (2015) .

[81] H. Fujii, D. Honda, M. Kato, Y. Kikukawa, S. Komatsu and T. Sano, *Hybrid monte carlo on lefschetz thimbles—a study of the residual sign problem*, *Journal of High Energy Physics* **2013** (2013) 1.

[82] M. Ulybyshev and S. Valgushev, *Path integral representation for the hubbard model with reduced number of lefschetz thimbles*, *arXiv preprint arXiv:1712.02188* (2017) .

[83] G.V. Dunne and M. Unsal, *What is qft? resurgent trans-series, lefschetz thimbles, and new exact saddles*, *arXiv preprint arXiv:1511.05977* (2015) .

[84] L. Scorzato, *The lefschetz thimble and the sign problem*, *arXiv preprint arXiv:1512.08039* (2015) .

[85] A. Behtash, G.V. Dunne, T. Schäfer, T. Sulejmanpasic and M. Unsal, *Toward picard-lefschetz theory of path integrals, complex saddles and resurgence*, *arXiv preprint arXiv:1510.03435* (2015) .

[86] J. Brown, A. Cole, G. Shiu and W. Cottrell, *Gravitational decoupling and the picard-lefschetz approach*, *Physical Review D* **97** (2018) 025002.

[87] D. Dorigoni and P. Glass, *Picard-lefschetz decomposition and cheshire cat resurgence in 3d n $\mathcal{N} = 2$ field theories*, *Journal of High Energy Physics* **2019** (2019) 1.

[88] A. Behtash, T. Sulejmanpasic, T. Schäfer and M. Unsal, *Hidden topological angles and lefschetz thimbles*, *arXiv preprint arXiv:1502.06624* (2015) .

[89] H. Fujii, S. Kamata and Y. Kikukawa, *Monte carlo study of lefschetz thimble structure in one-dimensional thirring model at finite density*, *Journal of High Energy Physics* **2015** (2015) 1.

[90] Y. Tanizaki, *Study on sign problem via Lefschetz-thimble path integral*, Ph.D. thesis, University of Tokyo, 2016.

[91] V.S. Filinov, A.S. Larkin et al., *Lefschetz thimbles and wigner functions*, *Journal of Applied Mathematics and Physics* **8** (2020) 1278.

[92] S. Bluecher, J.M. Pawlowski, M. Scherzer, M. Schlosser, I.-O. Stamatescu, S. Syrkowski et al., *Reweighting lefschetz thimbles*, *SciPost Physics* **5** (2018) 044.

[93] M. Fukuma, N. Matsumoto and N. Umeda, *Implementation of the hmc algorithm on the tempered lefschetz thimble method*, *arXiv preprint arXiv:1912.13303* (2019) .

[94] M. Cristoforetti, F. Di Renzo, G. Eruzzi, A. Mukherjee, C. Schmidt, L. Scorzato et al., *An efficient method to compute the residual phase on a lefschetz thimble*, *Physical Review D* **89** (2014) 114505.

[95] P. Seidel, *Fukaya categories and Picard-Lefschetz theory*, vol. 10, European Mathematical Society (2008).

[96] V. Olivier et al., *Airy functions and applications to physics*, World Scientific (2010).

[97] C.P. Society, *Transactions of the Cambridge Philosophical Society*, vol. 10, University Press (1864).

[98] P. Groeneboom, S. Lalley and N. Temme, *Chernoff's distribution and differential equations of parabolic and airy type*, *Journal of Mathematical Analysis and Applications* **423** (2015) 1804.

[99] S. Lefschetz, *Applications of Algebraic Topology: Graphs and Networks. The Picard-Lefschetz Theory and Feynman Integrals*, vol. 16, Springer Science & Business Media (2012).

[100] É. Picard, *Théorie des fonctions algébriques de deux variables indépendantes*, vol. 1, Gauthier-Villars (1897).

[101] V. Vassiliev, *Applied Picard–Lefschetz theory, mathematical surveys and monographs*, American Mathematical Society (2002).

[102] G. Narain and H.-Q. Zhang, *Lorentzian quantum cosmology in novel gauss-bonnet gravity from picard-lefschetz methods*, *arXiv preprint arXiv:2006.02298* (2020) .

[103] K. Fukushima and T. Shimazaki, *Lefschetz-thimble inspired analysis of the dykhne–davis–pechukas method and an application for the schwinger mechanism*, *Annals of Physics* **415** (2020) 168111.

[104] A. Alexandru, G. Başar, P.F. Bedaque and N.C. Warrington, *Tempered transitions between thimbles*, *Physical Review D* **96** (2017) 034513.

[105] H. Fujii, S. Kamata and Y. Kikukawa, *Lefschetz thimble structure in one-dimensional lattice thirring model at finite density*, *Journal of High Energy Physics* **2015** (2015) 1.

[106] F. Di Renzo, S. Singh and K. Zambello, *Taylor expansions on lefschetz thimbles*, *Physical Review D* **103** (2021) 034513.

[107] C. Schmidt and F. Ziesché, *Simulating low dimensional qcd with lefschetz thimbles*, *arXiv preprint arXiv:1701.08959* (2017) .

[108] K. Zambello, F. Di Renzo and S. Singh, *Taylor expansions and pad\'e approximations for lefschetz thimbles and beyond*, *arXiv preprint arXiv:2111.14698* (2021) .

[109] Y. Tanizaki, H. Nishimura and J.J. Verbaarschot, *Gradient flows without blow-up for lefschetz thimbles*, *Journal of High Energy Physics* **2017** (2017) 1.

[110] G. Aarts, L. Bongiovanni, E. Seiler and D. Sexty, *Some remarks on lefschetz thimbles and complex langevin dynamics*, *Journal of High Energy Physics* **2014** (2014) 1.

[111] Z. Guralnik, *A new look at the helmholtz equation: Lefschetz thimbles and the einbein action*, *arXiv preprint arXiv:1810.02339* (2018) .

[112] P. Seidel, *Picard–lefschetz theory and dilating $\mathbb{C}^*$-actions*, *Journal of Topology* **8** (2015) 1167.

[113] A. Behtash, *Non-Perturbative Physics from the Picard-Lefschetz Theory of Path Integrals*, North Carolina State University (2019).

[114] A. Cherman, D. Dorigoni and M. Ünsal, *Decoding perturbation theory using resurgence: Stokes phenomena, new saddle points and lefschetz thimbles*, *Journal of High Energy Physics* **2015, 10** (2015) 1.

[115] R. Bharathkumar, *The sign problem and lefschetz thimbles*, .

[116] G. Aarts, *Introductory lectures on lattice qcd at nonzero baryon number*, in *Journal of Physics: Conference Series*, vol. 706, 2, p. 022004, IOP Publishing, 2016.

[117] F.F. Assaad and W. Hanke, *Numerical simulations of strongly correlated electron systems*, in *NIC Symposium 2006*, vol. 32, pp. 175–182, NIC Series, 2020.

[118] M. Fromm, J. Langelage, S. Lottini, M. Neuman and O. Philipsen, *Onset transition to cold nuclear matter from lattice qcd with heavy quarks*, *Physical review letters* **110** (2013) 122001.

[119] A. Mollgaard and K. Splittorff, *Complex langevin dynamics for chiral random matrix theory*, *Physical Review D* **88** (2013) 116007.

[120] G. Aarts, F. Attanasio, B. Jäger and D. Sexty, *Results on the heavy-dense qcd phase diagram using complex langevin*, *arXiv preprint arXiv:1610.04401* (2016) .

[121] U. Nowak, R.W. Chantrell and E. Kennedy, *Monte carlo simulation with time step quantification in terms of langevin dynamics*, *Physical review letters* **84** (2000) 163.

[122] D.L. Ermak and H. Buckholz, *Numerical integration of the langevin equation: Monte carlo simulation*, *Journal of Computational Physics* **35** (1980) 169.

[123] P.H. Damgaard and H. Hüffel, *Stochastic quantization*, *Physics Reports* **152** (1987) 227.

[124] D. Sexty, *Simulating full qcd at nonzero density using the complex langevin equation*, *Physics Letters B* **729** (2014) 108.

[125] X. Cheng, M. Jalil, H.K. Lee and Y. Okabe, *Mapping the monte carlo scheme to langevin dynamics: a fokker-planck approach*, *Physical review letters* **96** (2006) 067208.

[126] J. Ambjørn, M. Flensburg and C. Peterson, *The complex langevin equation and monte carlo simulations of actions with static charges*, *Nuclear Physics B* **275** (1986) 375.

[127] G. Parisi, *On complex probabilities*, *Physics Letters B* **131** (1983) 393.

[128] P. Meakin, H. Metiu, R. Petschek and D. Scalapino, *The simulation of spinodal decomposition in two dimensions: a comparison of monte carlo and langevin dynamics*, *The Journal of chemical physics* **79** (1983) 1948.

[129] G.G. Batrouni and R.T. Scalettar, *Quantum monte carlo with the langevin equation: Coupled bose-fermi systems*, in *Journal of Physics: Conference Series*, vol. 1290, p. 012004, IOP Publishing, 2019.

[130] R. Ettelaie and M. Moore, *Comparison of langevin and monte carlo dynamics*, *Journal of Physics A: Mathematical and General* **17** (1984) 3505.

[131] W. Coffey and Y.P. Kalmykov, *The Langevin equation: with applications to stochastic problems in physics, chemistry and electrical engineering*, vol. 27, World Scientific (2012).

[132] F. James, *Complex Langevin dynamics as a cure for the sign problem*, Ph.D. thesis, Swansea U., 2012.

[133] G. Aarts, E. Seiler, D. Sexty and I.-O. Stamatescu, *On complex langevin dynamics and zeroes of the measure ii: Fermionic determinant*, *arXiv preprint arXiv:1611.02931* (2016) .

[134] A. Wawrzkiewicz-Jałowiecka, P. Borys and Z.J. Grzywna, *On application of langevin dynamics in logarithmic potential to model ion channel gate activity*, *Cellular and Molecular Biology Letters* **20** (2015) 663.

[135] A. Rudin and P. Choi, *Diffusion in polymers*, *The Elements of Polymer Science & Engineering, 3rd Edition, Academic Press, San Diego* (2013) 275.

[136] R. Pastor, *Techniques and applications of langevin dynamics simulations*, in *The Molecular Dynamics of Liquid Crystals*, pp. 85–138, Springer (1994).

[137] C. Berger, L. Rammelmüller, A. Loheac, F. Ehmann, J. Braun and J. Drut, *Complex langevin and other approaches to the sign problem in quantum many-body physics*, *Physics Reports* **892** (2021) 1.

[138] M. Scherzer, E. Seiler, D. Sexty and I.-O. Stamatescu, *Complex langevin and boundary terms*, *Physical Review D* **99** (2019) 014512.

[139] I. Sato and H. Nakagawa, *Approximation analysis of stochastic gradient langevin dynamics by using fokker-planck equation and ito process*, in *International Conference on Machine Learning*, pp. 982–990, PMLR, 2014.

[140] J.L. García-Palacios and F.J. Lázaro, *Langevin-dynamics study of the dynamical properties of small magnetic particles*, *Physical Review B* **58** (1998) 14937.

[141] H. Makino, H. Suzuki and D. Takeda, *Complex langevin method applied to the 2d s u (2) yang-mills theory*, *Physical Review D* **92** (2015) 085020.

[142] A. Durmus and E. Moulines, *Nonasymptotic convergence analysis for the unadjusted langevin algorithm*, *The Annals of Applied Probability* **27** (2017) 1551.

[143] K. Nagata, J. Nishimura and S. Shimasaki, *Argument for justification of the complex langevin method and the condition for correct convergence*, *Physical Review D* **94** (2016) 114515.

[144] J. Berges and I.-O. Stamatescu, *Simulating nonequilibrium quantum fields with stochastic quantization techniques*, *Physical review letters* **95** (2005) 202003.

[145] J. Berges, S. Borsanyi, D. Sexty and I.-O. Stamatescu, *Lattice simulations of real-time quantum fields*, *Physical Review D* **75** (2007) 045007.

[146] H.J. Rothe, *Lattice gauge theories: an introduction*, World Scientific Publishing Company (2012).

[147] S. Weinberg, *The quantum theory of fields*, vol. 2, Cambridge university press (1995).

[148] R. Jackiw, *Analysis on infinite-dimensional manifolds-schrödinger representation for quantized fields*, .

[149] J. Schwinger, *Brownian motion of a quantum oscillator*, *Journal of Mathematical Physics* **2** (1961) 407.

[150] L.V. Keldysh et al., *Diagram technique for nonequilibrium processes*, *Sov. Phys. JETP* **20** (1965) 1018.

[151] C. Greiner and B. Müller, *Classical fields near thermal equilibrium*, *Physical Review D* **55** (1997) 1026.

[152] A. Kamenev and A. Levchenko, *Keldysh technique and non-linear $\sigma$-model: basic principles and applications*, *Advances in Physics* (2010) .

[153] C.M. Bender and T.T. Wu, *Anharmonic oscillator*, *Physical Review* **184** (1969) 1231.

[154] A. Cherman and M. Unsal, *Real-time feynman path integral realization of instantons*, *arXiv preprint arXiv:1408.0012* (2014) .

[155] A. Alexandru, P.F. Bedaque, H. Lamm and S. Lawrence, *Finite-density monte carlo calculations on sign-optimized manifolds*, *Physical Review D* **97** (2018) 094510.

[156] A. Alexandru, G. Başar, P.F. Bedaque, H. Lamm and S. Lawrence, *Finite density qed 1+ 1 near lefschetz thimbles*, *Physical Review D* **98** (2018) 034506.

[157] M. Fukuma and N. Umeda, *Parallel tempering algorithm for integration over lefschetz thimbles*, *Progress of Theoretical and Experimental Physics* **2017** (2017) 073B01.

[158] G. Aarts, D. Bachtis and B. Lucini, *Interpreting machine learning functions as physical observables*, *arXiv preprint arXiv:2109.08497* (2021) .

[159] Y. Jia, S. Yu and J. Ma, *Intelligent interpolation by monte carlo machine learning*, *Geophysics* **83** (2018) V83.

[160] M.N. Jones, J. Frutiger, N.G. Ince and G. Sin, *The monte carlo driven and machine learning enhanced process simulator*, *Computers & Chemical Engineering* **125** (2019) 324.

[161] T.H. Oakes, A. Moss and J.P. Garrahan, *A deep learning functional estimator of optimal dynamics for sampling large deviations*, *Machine Learning: Science and Technology* **1** (2020) 035004.

[162] A. Moss, *Accelerated bayesian inference using deep learning*, *Monthly Notices of the Royal Astronomical Society* **496** (2020) 328.

[163] D. Bachtis, G. Aarts and B. Lucini, *Quantum field theories, markov random fields and machine learning*, in *Journal of Physics: Conference Series*, vol. 2207, p. 012056, IOP Publishing, 2022.

[164] J. Krüger and R. Westermann, *Linear algebra operators for gpu implementation of numerical algorithms*, in *ACM SIGGRAPH 2005 Courses*, pp. 234–es (2005).

[165] S.S. Leang, A.P. Rendell and M.S. Gordon, *Quantum chemical calculations using accelerators: Migrating matrix operations to the nvidia kepler gpu and the intel xeon phi*, *Journal of chemical theory and computation* **10** (2014) 908.

[166] A.A. Shabalin, *Matrix eqtl: ultra fast eqtl analysis via large matrix operations*, *Bioinformatics* **28** (2012) 1353.

[167] R. Nishino and S.H.C. Loomis, *Cupy: A numpy-compatible library for nvidia gpu calculations*, *31st confernce on neural information processing systems* **151** (2017) .

[168] K. Fatahalian, J. Sugerman and P. Hanrahan, *Understanding the efficiency of gpu algorithms for matrix-matrix multiplication*, in *Proceedings of the ACM SIGGRAPH/EUROGRAPHICS conference on Graphics hardware*, pp. 133–137, 2004.

[169] V.M. Garcia, A. Liberos, A.M. Climent, A. Vidal, J. Millet and A. Gonzalez, *An adaptive step size gpu ode solver for simulating the*

*electric cardiac activity*, in *2011 Computing in Cardiology*, pp. 233–236, IEEE, 2011.

[170] Y. Shi, W.H. Green, H.-W. Wong and O.O. Oluwole, *Accelerating multi-dimensional combustion simulations using gpu and hybrid explicit/implicit ode integration*, *Combustion and Flame* **159** (2012) 2388.

[171] D. Boyda, S. Calì, S. Foreman, L. Funcke, D.C. Hackett, Y. Lin et al., *Applications of machine learning to lattice quantum field theory*, *arXiv preprint arXiv:2202.05838* (2022) .

# Appendices

# Appendix A

# Airy Solution Proof

Here, the fact that (1.38) is a solution to (1.39) is demonstrated. Differentiating (1.38) twice using Leibniz's Integral Rule, it can be seen that

$$y'' = -\frac{1}{2\pi}\int_{-\infty}^{\infty} \mathrm{d}\varphi\ \varphi^2 \exp\left[i\left(\frac{\varphi^3}{3} + z\varphi\right)\right] \quad , \tag{A.1}$$

where $y''$ denotes the second derivative with respect to $z$. This can then be inserted into (1.39) with the substitution for $y$ given from (1.38) to give

$$y'' - zy = \frac{i}{2\pi}\int_{-\infty}^{\infty} \mathrm{d}\varphi\ i(\varphi^2 + z) \exp\left[i\left(\frac{\varphi^3}{3} + z\varphi\right)\right] = 0, \tag{A.2}$$

where the factor of $i$ has been introduced by splitting the minus sign. It can now be noted that the factor before the exponential is the derivative of the exponential's argument, allowing for simple integration giving

$$y'' - zy = \frac{i}{2\pi} \exp\left[i\left(\frac{\varphi^3}{3} + z\varphi\right)\right]\Bigg|_{-\infty}^{\infty} = 0, \tag{A.3}$$

which can be evaluated using the Cauchy Principle Value [96] to give 0, as required.

# Appendix B

# Analytic Continuation Evaluation Comparison

A Gaussian integral with an imaginary exponent,

$$\int_{-\infty}^{\infty} \mathrm{d}\varphi \; e^{i\varphi^2/2}, \tag{B.1}$$

cannot be solved by the usual polar co-ordinate transform typically used to solve this problem. However, it can be solved by analytically extending the integrand and using Cauchy's integral formula, as shown. For a complex valued $\phi$ it can be stated that

$$\oint_c \mathrm{d}\phi \; e^{i\phi^2/2} = 0, \tag{B.2}$$

along a closed contour $c$, due to the absence of poles in $e^{i\phi^2/2}$. By writing $\phi$ in angular representation, the integrand of (B.2) can be separated into its real and imaginary parts and written

$$\exp\big(i\phi^2/2\big) = \exp\left[ir^2\cos(2\theta)/2\right]\exp\left[-r^2\sin(2\theta)/2\right]. \tag{B.3}$$

This means in regions where $\sin(2\theta)$ is positive, the integrand is suppressed for large $r$, which corresponds to the real positive, imaginary positive quadrant and real negative, imaginary negative quadrant in the Argand plane. Combining these two pieces of information, we can write the contour $c = c_1 + c_2 + c_3 + c_4$

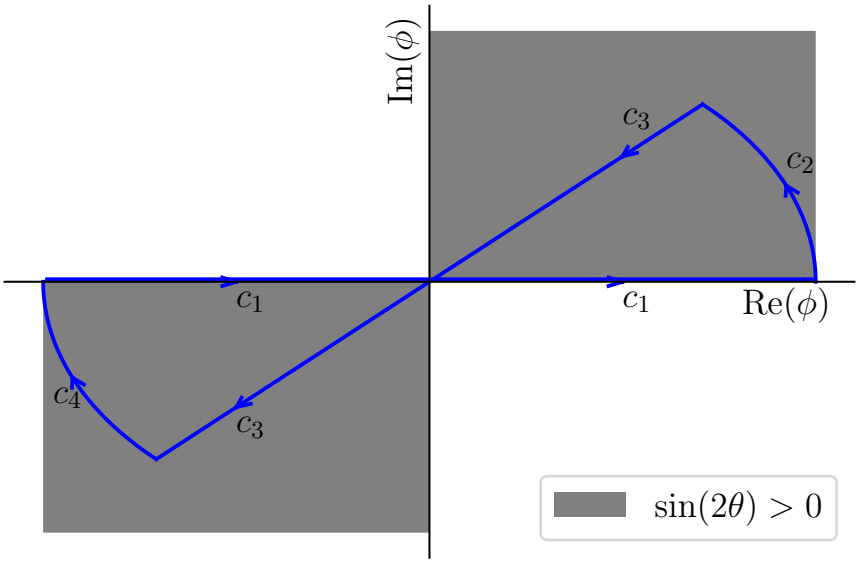


Figure B.1: Path of the contour $c$ through the complex plane to allow for evaluation of an imaginary valued Gaussian.

as shown in Figure B.1. In the limit where $c_1$ extends along the entire real axis, $c_1$ represents the integral shown in (B.1), and conveniently ensures the large $r$ behaviour discussed above. That suppression ensures that the contribution of the integral over $c_2, c_4 \to 0$. Consequently (B.2) reduces to

$$\int_{-\infty}^{\infty} \mathrm{d}\phi \; e^{i\phi^2/2} + \int_{c_3} \mathrm{d}\phi \; e^{i\phi^2/2} = 0. \tag{B.4}$$

There are many valid paths that could make up $c_3$, and equally many to parameterise them. However one of the easiest is $\phi_{c_3}(t) = t(1+i)$ and performing this substitution gives

$$\int_{-\infty}^{\infty} \mathrm{d}\phi \; e^{i\phi^2/2} + \int_{\infty}^{-\infty} \mathrm{d}t \; (1+i) e^{-it^2/2} = 0, \tag{B.5}$$

where the orientation of the $c_3$ contour is implemented through the signs on the limits. This gives

$$\int_{-\infty}^{\infty} \mathrm{d}\phi \; e^{i\phi^2/2} = (1+i) \int_{-\infty}^{\infty} \mathrm{d}t \; e^{-it^2/2} \tag{B.6}$$

$$= (1+i)\sqrt{\pi}, \tag{B.7}$$

as required to match the result given by the thimble method in (1.52). Note the change of the limits in (B.6) to account for the factor of $-1$.

# Appendix C

# Additional Jacobian Sampling Data

The sample of data included in Table 2.1 shows that it is possible to decrease the frequency with which the Jacobian is calculated to improve computational efficiency. However, there are practical limits to this. As the manifold is updated, the topology changes rendering the Jacobian out of date and useless. Continuing with the data presented in Chapter 2, Table C.1 includes more information, showing that while for a low value of $M$, the parameter dictating how often the Jacobian should be recalculated, and $\tau$, it is possible to get accurate results, even as high as $M = 10$. Unfortunately, this means limiting the simulations to $\tau = 0.1$, which as shown in Chapter 4, is devastating to the error, before considering the additional error effects of this approximate Jacobian.

| M | Mean time per update (ms) | Error | $\tau$ | Accurate |
|---|---|---|---|---|
| 1 | 0.30 | 0.05 | 0 | Yes |
| 1 | 0.7 | 0.1 | 0.1 | Yes |
| 1 | 1.1 | 0.1 | 0.2 | Yes |
| 1 | 2.6 | 0.3 | 0.5 | Yes |
| 1 | 5.0 | 0.5 | 1 | Yes |
| 2 | 0.28 | 0.05 | 0 | Yes |
| 2 | 0.37 | 0.06 | 0.1 | Yes |
| 2 | 0.61 | 0.09 | 0.2 | Yes |
| 2 | 1.4 | 0.1 | 0.5 | Yes |
| 2 | 2.6 | 0.3 | 1 | Yes |
| 3 | 0.28 | 0.05 | 0 | Yes |
| 3 | 0.25 | 0.05 | 0.1 | Yes |
| 3 | 0.38 | 0.05 | 0.2 | Yes |
| 3 | 0.95 | 0.08 | 0.5 | No |
| 3 | 1.7 | 0.2 | 1 | No |
| 5 | 0.27 | 0.05 | 0 | Yes |
| 5 | 0.15 | 0.03 | 0.1 | Yes |
| 5 | 0.23 | 0.05 | 0.2 | Yes |
| 5 | 0.55 | 0.05 | 0.5 | No |
| 5 | 1.1 | 0.1 | 1 | No |
| 10 | 0.25 | 0.05 | 0 | Yes |
| 10 | 0.02 | 0.01 | 0.1 | Yes |
| 10 | 0.04 | 0.02 | 0.2 | No |
| 10 | 0.19 | 0.04 | 0.5 | No |
| 10 | 0.4 | 0.1 | 1 | No |
| 20 | 0.23 | 0.05 | 0 | Yes |
| 20 | 0.04 | 0.01 | 0.1 | No |
| 20 | 0.07 | 0.01 | 0.2 | No |
| 20 | 0.14 | 0.02 | 0.5 | No |
| 20 | 0.26 | 0.05 | 1 | No |

Table C.1: Further effects of skipping Jacobian updates on runtime.